



저작자표시-비영리-변경금지 2.0 대한민국

이용자는 아래의 조건을 따르는 경우에 한하여 자유롭게

- 이 저작물을 복제, 배포, 전송, 전시, 공연 및 방송할 수 있습니다.

다음과 같은 조건을 따라야 합니다:



저작자표시. 귀하는 원저작자를 표시하여야 합니다.



비영리. 귀하는 이 저작물을 영리 목적으로 이용할 수 없습니다.



변경금지. 귀하는 이 저작물을 개작, 변형 또는 가공할 수 없습니다.

- 귀하는, 이 저작물의 재이용이나 배포의 경우, 이 저작물에 적용된 이용허락조건을 명확하게 나타내어야 합니다.
- 저작권자로부터 별도의 허가를 받으면 이러한 조건들은 적용되지 않습니다.

저작권법에 따른 이용자의 권리는 위의 내용에 의하여 영향을 받지 않습니다.

이것은 [이용허락규약\(Legal Code\)](#)을 이해하기 쉽게 요약한 것입니다.

[Disclaimer](#)

공학박사학위논문

**A study on the effect of stress on the growth,  
and electrical, mechanical behaviors of one-  
dimensional nanomaterials**

1 차원 나노물질의 성장 및 전기적, 기계적 거동에  
미치는 응력의 영향에 관한 연구

2015 년 8 월

서울대학교 대학원  
재료공학부  
김 도 현

## **Abstract**

# **A study on the effect of stress on the growth, and electrical, mechanical behaviors of one-dimensional nanomaterials**

Do Hyun Kim

Department of Materials Science and Engineering

The Graduate School

Seoul National University

Stress or strain is a universal phenomenon pertinent to the synthesis, fabrication, and application of all types of materials. In the plastic regime, materials generally undergo irreversible changes, such as failure or property degradation. Elastic deformation, on the other hand, can induce reversible changes to materials properties from electronic and chemical to optical. The strength of a material depends very strongly on its dimensions. Typically, smaller structure can tolerate larger deformations before yielding. Therefore, it is anticipated that stress or strain engineering can be profitably explored in materials with reduced

dimensions, such as one-dimensional nanowires.

Rapid progress in device miniaturization has led to the rise of flexible, nanoscale devices for which one-dimensional nanowires and atomic sheets are particularly promising candidate materials. These nanomaterials possess unusual properties arising from giant surface effect and quantum confinement, and super mechanical properties. Therefore, nanowires are one of ideal platforms to explore novel stress effect and device concepts at the nanoscale, such as energy harvesting piezoelectric nano-generator, stress induced phase transition, and wrinkle based stretchable electronics.

In this dissertation, we focused the effect of stress on the growth and piezoresistive properties of one-dimensional nanowires.

In a view of growth, we utilized the stress driven single crystalline indium nanowire growth on InGa<sub>N</sub> substrate by ion beam irradiation. With comprehensive microstructural and chemical analysis, we confirmed that source of indium nanowire growth was originated from Ga<sup>+</sup> ion beam induced phase decomposition of InGa<sub>N</sub> substrate, and compressive stress build up by ion irradiation and atomic migration are responsible for the growth of indium nanowires as a process of stress relaxation. Since focused ion beam can be precisely controlled by

changing the accelerating voltage, current density, and location of irradiation, the diameter and length of the nanowires as well as their growth rate could be effectively controlled. Indium nanowires with diameter of 40-200 nm and length up to 120  $\mu\text{m}$  were fabricated at growth rate as high as 500 nm/s, which is remarkable fast compared with other nanowire growth methods.

Second, the effect of stress on the phase change nanowire ( $\text{Ge}_2\text{Sb}_2\text{Te}_5$ ) was explored to tune the electromechanical properties for the application to advanced electronic and memory devices.

A single crystalline GST nanowires were grown by the vapor-liquid-solid mechanism. And GST nanowires possess a large piezoresistive effect and strain dependent electrical switching behavior of PCM devices. For example, the longitudinal piezoresistance coefficient along  $\langle 10\bar{1}0 \rangle$  direction for GST nanowires reach as high as  $440 \times 10^{-11} \text{ Pa}^{-1}$ , which is comparable to the values of Si. Resistance change by strain was reversible, thus it restored its original resistance when uniaxial stress was released. Since GST is known as p-type semiconductor with negligible band gap of  $\sim 0.3 \text{ eV}$ , this great piezoresistivity of GST was originated from the hole mobility change, which induced the tunable switching

behaviors of phase change memory with threshold voltage changes. The large piezoresistance and strain dependent behavior of PCM enable the potential application not only for flexible memory device, but also for another candidate of piezoresistive materials for strain sensors.

Keywords: Nanotechnology, one-dimensional nanowire, focused ion beam, indium, stress driven nanowire growth, phase change memory,  $\text{Ge}_2\text{Sb}_2\text{Te}_5$ , threshold switching, uniaxial stress, piezoresistive effect

***Student Number:*** 2006-20819

# **Table of Contents**

<b>Abstract</b> .....	I
<b>Table of Contents</b> .....	V
<b>List of Tables</b> .....	XI
<b>List of Figures</b> .....	XII

## **Chapter 1. Introduction**

1.1 Introduction to nanomaterials.....	1
1.2 Thesis motivation.....	6
1.3 Reference.....	9

## **Chapter 2. Stress/strain engineering of 1-D nanomaterials**

2.1 Introduction.....	10
2.2 Stress/strain effect in 1D nanomaterials.....	11
2.2.1 Size effect of mechanical properties.....	12

2.2.2 Piezoresistance.....	12
2.2.3 Manipulation of MIT temperature.....	13
2.2.4 Nano-generator.....	14
2.3 References.....	19

### **Chapter 3. Ion beam induced stress and indium nanowire growth**

3.1 Introduction.....	20
3.2 Conventional methods for nanowire synthesis.....	21
3.2.1 Vapor-liquid-solid growth.....	21
3.2.2 Vapor-solid growth.....	26
3.2.3 Oxide assisted growth.....	26
3.2.4 Template based synthesis.....	30
3.3 Stress driven nanowire growth.....	34
3.3.1 Stress induced migration: atomic diffusion.....	35
3.4 Ion implantation induced stress.....	41
3.4.1 Origin of stress evolution in ion irradiated surface.....	41
3.5 Experimental procedure.....	45
3.5.1 Preparation of InGaN substrate.....	45

3.5.2 FIB/SEM dual beam system: nanowire growth.....	48
3.5.3 Methods for the structural and chemical characterization...	48
3.6 Results and discussion.....	53
3.6.1 Growth of nanowire.....	53
3.6.2 Identification of nanowire.....	57
3.6.3 Controlled nanowire growth: dimension and growth rate...	57
3.6.4 Growth mechanism.....	63
3.6.5 Site selective growth and patterning.....	69
3.7 Conclusion.....	74
3.8 References.....	75

## **Chapter 4. Stress induced piezoresistive effect in $\text{Ge}_2\text{Sb}_2\text{Te}_5$ (GST) phase change nanowire**

4.1 Piezoresistive effect in semiconductor.....	78
4.1.1 Historical overview.....	78
4.1.2 Piezoresistivity fundamentals.....	82
4.2 Phase change materials.....	91
4.2.1 General introduction.....	91
4.2.2 $\text{Ge}_2\text{Sb}_2\text{Te}_5$ compound.....	95

4.2.3 Electronic state of amorphous $\text{Ge}_2\text{Sb}_2\text{Te}_5$ .....	96
4.2.4 Band structure of $\text{Ge}_2\text{Sb}_2\text{Te}_5$ .....	97
4.2.5 Mechanisms of threshold switching.....	103
4.3 Experimental procedure.....	105
4.3.1 Synthesis of GST nanowire.....	105
4.3.2 Device fabrication.....	107
4.3.3 Mechanical stressing and electrical measurements.....	111
4.4 Results and discussion.....	112
4.4.1 Analysis of GST nanowire.....	112
4.4.2 Young's modulus of GST nanowire.....	115
4.4.3 Piezoresistivity in GST nanowire.....	118
4.4.4 Origin of piezoresistivity in GST.....	121
4.4.5 Effect of stress on phase change behavior.....	123
4.5 Conclusion.....	127
4.6 References.....	128
<b>Chapter 5. Conclusion.....</b>	<b>131</b>

## **Appendix I. UV-responsive nanoparticle and its application to oil recovery**

6.1 Oil absorption/desorption materials and wettability.....	133
6.2 Experimental procedure.....	135
6.2.1 Synthesis of hydrocarbon and TiO <sub>2</sub> nanoparticles.....	135
6.2.2 Fabrication of nanoparticle sponge.....	136
6.2.3 Fabrication of the NS/p-PDMS.....	136
6.2.4 Characterization methods.....	137
6.3 Results and discussion.....	142
6.3.1 Tunable surface wettability underwater.....	142
6.3.2 Spontaneous bubble growth.....	148
6.3.3 Oil absorption/desorption using the nano-sponge.....	150
6.3.4 Vertical force balance at the oil-solid interface.....	154
6.3.5 Oil absorption/desorption with NS/p-PDMS.....	159
6.3.6 Recyclable oil absorption/desorption.....	163
6.4 Conclusion.....	169
6.5 References.....	170

## **Appendix II. Microtexture development during equi-biaxial tensile deformation in monolithic and dual phase steels**

7.1 Microstructure and deformation behavior in DP steel.....	173
7.2 Experimental procedure.....	176
7.2.1 Equi-biaxial deformation and microstructure.....	176
7.2.2 Materials and determination of martensite fraction.....	178
7.3 Results and discussion.....	182
7.3.1 Microtexture development in IF and DP steels.....	182
7.3.2 VPSC model: texture prediction.....	185
7.3.3 Orientation rotation/spread of individual ferrite grains.....	190
7.3.4 Strain partitioning and GND.....	191
7.4 Conclusion.....	198
7.5 References.....	200
요약 (국문초록).....	203

## LIST OF TABLES

- Table 4.1 Numerical values of the parameters describing the band structure for crystalline and amorphous GST
- Table 6.1 Weight and volume mixing ratio of each nano-sponge and its atomic composition determined using energy-dispersive X-ray spectroscopy.

## LIST OF FIGURES

- Figure 1.1 Fluorescence of CdSe-Cds core-shell nanoparticles with a diameter of 1.7 nm up to 6 nm
- Figure 1.2 The effect of the increased surface area provided by nanostructured materials
- Figure 2.1 Variation of the Young's modulus as a function of the diameters silver nanowires
- Figure 2.2 Giant piezoresistance of p-type silicon nanowire
- Figure 2.3 Stress (or Strain) manipulation of metal-insulator transition at room temperature in VO<sub>2</sub> nanowires
- Figure 2.4 ZnO nanowires: nano-generator based on piezoelectric properties
- Figure 3.1 (a) Schematic illustration of vapor-liquid-solid growth mechanism including three stages. (b) The binary phase diagram between Au and Ge including three stages of (I) alloying, (II) nucleation, and (III) growth
- Figure 3.2 In-situ TEM images recorded during the process of

nanowire growth. (a) Au nanoclusters in solid state at 500 °C; (b) alloying initiated at 800 °C, at this stage Au exists mostly in solid state; (c) liquid Au/Ge alloy; (d) the nucleation of Ge nanocrystal on the alloy surface; (e) Ge nanocrystal elongates with further Ge condensation and eventually forms a wire (f).

Figure 3.3 TEM images of (a) Si nanowire nuclei formed on the Mo grid and (b), (c) initial growth stages of the nanowires.

Figure 3.4 Schematic diagram of the nucleation and growth mechanism of Si nanowires. The parallel lines indicate the [112] orientation. (a) Si oxide vapor is deposited first and forms the matrix within which the Si nanoparticles are precipitated. (b) Nanoparticles in a preferred orientation grow fast and form nanowires. Nanoparticles with non-preferred orientations may form chains of nanoparticles.

Figure 3.5 AFM image of an anodic alumina membrane (AAM).

Figure 3.6 Schematic diagram showing the formation of nanowires by templating against mesostructures which are self-

assembled from surfactant molecules. (a) Formation of cylindrical micelle; (b) formation of the desired material in the aqueous phase encapsulated by the cylindrical micelle; (c) removal of the surfactant molecule with an appropriate solvent to obtain an individual nanowire.

Figure 3.7 Growth process of the Al nanowire: illustration of the growth mechanism (the extrusion of atoms from the bases of nanowires)

Figure 3.8 Growth mechanism and structural characteristic of the single crystalline Bi nanowires (a) a schematic representation of the growth of Bi nanowires by on-film formation of nanowires, (b) SEM image of a Bi nanowire grown on Bi thin film, and (c) a low magnification TEM image of Bi nanowire

Figure 3.9 Illustration for the phenomenon of stress migration in a material with a distribution of compressive stress

Figure 3.10 A schematic representation of the three microstructural regimes that arise from ion-implantation into crystalline materials. In Region I (low dose), a damaged but still

crystalline solid solution is formed. In Region II (intermediate doses), amorphous material is initially formed at the peak of the displacement damage profile, In Region III (sufficiently high doses), a true surface amorphous layer is formed

Figure 3.11 Plane view SEM image of In-rich InGaN film grown by MOCVD. The inset shows the cross-section view of specimen

Figure 3.12 XRD measurement of In-rich InGaN

Figure 3.13 FIB/SEM dual beam system for nanowire growth

Figure 3.14 Procedure of nanowire TEM sampling: (a) the bottom of nanowire on InGaN film (b) Detachment of nanowire from substrate by Omni-probe, (c) The nanowire pick-up and transfer, (d) approaching to the Cu grid, (e) Pt deposition for nanowire to grid (f) completion of TEM sampling

Figure 3.15 Schematic illustration of indium nanowire growth induced by FIB irradiation

Figure 3.16 Time evolution of formation of straight nanowires after exposure to FIB with accelerating voltage of 10 kV and ion current density of 200 nA/cm<sup>2</sup>, Scale bar = 20 μm (left ) and 10 μm (right)

Figure 3.17 TEM analysis of the nanowire (a) Bright field image with growth direction. Inset shows the diffraction pattern of the indium nanowire along the [110] zone axis, (b) EDS spectrum of nanowire

Figure 3.18 Dependence of the nanowires dimensions and growth rate on the ion beam parameters. (a) Length distribution of the nanowires synthesized at current density of 15 nA cm<sup>-2</sup> and different ion beam accelerating voltages. The lines denoted by 50%, 70% and 90% indicate the 50<sup>th</sup>, 70<sup>th</sup> and 90<sup>th</sup> percentile of the collected data for nanowires length at each accelerating voltage. (b) Dependence of nanowires average length and diameter on the ion beam parameters. (c) Dependence of the average growth rate of nanowires on the ion beam current density measured for three distinct voltages of 5, 10, 20 kV

- Figure 3.19 EELS composition map using HVEM (a) before and (b) after Ga<sup>+</sup> ion irradiation on InGaN. Indium (red), Gallium (red), Nitrogen (green)
- Figure 3.20 In-situ monitoring of cross-section view of InGaN during Ga<sup>+</sup> ion irradiation on the surface
- Figure 3.21 TEM analysis of InGaN and GaN substrate to calculate the misfit strain by measuring the d-spacing (a,b) Low magnification of sample, (c) diffraction patterns of InGaN and GaN
- Figure 3.22 Measured d-spacings of (a) InGaN (b) GaN and (c) calculated misfit strain dependent on the orientation
- Figure 3.23 Functional networks of nanowires. (a) SEM image of a network of single indium nanowires created on selected locations using a maskless patterning. (b) Nanowire forests of 25 x 25 μm<sup>2</sup> size. In both experiments, the current density and accelerating voltage of the ion beam were 1.2 μA cm<sup>-2</sup> and 10 kV for (a) and 350 nA cm<sup>-2</sup> and 5 kV for (b). Scale bar = 5 μm, unless denoted otherwise

- Figure 4.1 The alteration of specific resistance produced in different metals
- Figure 4.2 Isotropic stress applied on silicon crystal. BEP refers to the minimum energy for electron to exist in conduction band
- Figure 4.3 Schematic of hole energy of silicon subjected to uniaxial stress
- Figure 4.4 Operation principles of PRAM: (L) application of current pulse and resultant phases of phase change material, (R) typical current-voltage curves of PRAM
- Figure 4.5 Band diagram for amorphous chalcogenide. On the left is Mott's model and on the right is the mapping in a standard semiconductor band diagram
- Figure 4.6 Band diagrams for both crystal and amorphous phases implemented in numerical model
- Figure 4.7 CVD system and furnace schematic diagram for nanowire growth.

- Figure 4.8 Aligned GST nanowires on PI substrate by contact printing method: (a) high density and (b) low density transfer by controlling the contact pressure
- Figure 4.9 Process for device fabrication and optical image of fabricated memory device.
- Figure 4.10 Sequence of experiment to exert the external stress/strain to GST nanowire including nanowire transfer, alignment, and straining
- Figure 4.11 Morphology and chemical composition of GST nanowires by SEM and EDS analysis: (a) low magnification, and (b) high magnification SEM images of GST nanowires, and EDS spectrum with chemical composition.
- Figure 4.12 (a) Bright field TEM image of a single crystalline GST nanowire, (b) high-resolution TEM image of the nanowire: the white arrow indicates the growth direction of the nanowire, (c) diffraction pattern of hexagonal GST structure (ZA [0001])

Figure 4.13 In-situ uniaxial tensile test of GST nanowire for Young's modulus measurement inside SEM chamber. (a-b) Optical images of the MEMS tensile testing device. (c) GST nanowire is attached to load cell using electron beam induced Pt-C deposition. (d) Engineering stress-strain curves with varying nanowire diameter. (e) Measured Young's modulus values of GST nanowire.

Figure 4.14 Current (I)-Voltage (V) measurement of GST NW under different strain condition: (a) I-V sweep curves of GST nanowire with uniaxial strain from -0.4% (compression) to 0.4% (tension), Inset shows resistance changes with external strain. Electrical measurements show that GST nanowire exhibits reversible responses to external strain, and original resistance was recovered after releasing strain. (b) Plot of relative resistivity changes of representative GST nanowires vs. external strain and stress representing piezoresistance effect.

- Figure 4.15 Resistance of amorphous and crystalline GST nanowire under the compressive (blue), tensile (green) stress and unstrained (red) state
- Figure 4.16 (a) Threshold switching behavior of GST and (b) relation between threshold voltage and resistance
- Figure 6.1 Preparation of nano-sponge, composed of Mixture of hydrophobic hydrocarbon and hydrophilic  $\text{TiO}_2$  nanoparticles and the surface morphology and chemical composition of the nano-sponge using scanning electron microscopy (SEM) and energy-dispersive X-ray spectroscopy (EDS). Photograph of hydrocarbon/ $\text{TiO}_2$  NPs (a) before and (b) after mixing in an IPA solution. SEM images of the nano-sponges (hydrocarbon/ $\text{TiO}_2$  NPs) with volume ratios of (c) 10/0, (d) 6/4, (e) 4/6 and (f) 0/10. (g) Atomic composition of the nano-sponges with different mixing volume ratios measured with EDS
- Figure. 6.2 Water CA in air and oil (n-hexane); CA underwater on the nano-sponges for each volume ratio (hydrocarbon/ $\text{TiO}_2$ :

10/0, 8/2, 6/4, 4/6, 2/8, 0/10) before/after UV irradiation for 2 hrs.

Figure 6.3 Surface wettability of water and oil (n-hexane) on a nano-sponge before and after UV irradiation. (a) Water and oil contact angle (CA) in air, (b) underwater oil CA and work of adhesion. Insets are snapshots of the oil droplets immediately prior to detachment from the injection needle before (lower inset) and after (upper inset) UV irradiation. (c) X-ray photoelectron spectroscopy analysis before (upper graph) and after (lower graph) UV irradiation

Figure 6.4 Spontaneous growth of bubbles within an oil droplet on the surface of nano-sponge underwater with UV irradiation. (a) Bubble growth within a light oil (n-hexane, density: 0.6548 g/ml) droplet in contact with 6/4 nano-sponge underwater with increasing UV irradiation times of 0, 1, 2, 4, 8, and 16 hr and (b) underwater oil CA measured from (a)

Figure 6.5 Spontaneous growth of bubbles within an oil droplet and oil/bubble release behavior on the surface of the nano-

sponge underwater with UV irradiation: A heavy oil (3 M Fluorinert FC-770, density: 1.793 g/ml) release behaviors from the nano-sponges with hydrocarbon/TiO<sub>2</sub> volume ratios of (a) 6/4, (b) 10/0 with UV irradiation for 0, 17, 30, 32, and 33 hr, as well as after 33 hr. (c) Underwater oil CA and (d) ratio of the oil contact radius ( $R_C$ ) to the original oil contact radius ( $R_{C, \text{initial}}$ ) for the 6/4 and 10/0 nano-sponges with UV irradiation.

Figure 6.6 Vertical force components of the surface tension ( $F_S$ ), pressure force ( $F_P$ ), and buoyancy ( $F_B$ ) of the oil/bubble at the oil-solid interface underwater during UV irradiation: (a) schematic illustration of each force component. The buoyancy, pressure force, surface tension force, and net force ( $F_{\text{NET}}$ ) were non-dimensionalized and plotted as bubble radius ( $R_B$ )/contact radius ( $R_C$ ) for (b) 6/4 and (c) 10/0 nano-sponges

Figure 6.7 Spontaneous oil (n-hexane, dyed in blue) absorption/desorption of a 6/4 NS/p-PDMS during UV irradiation, and the origin of bubble growth with the oil

desorption mechanism. Oil desorption with UV irradiation time (a) 0 hr and (b) 8 hr, respectively. (c) Snapshot of oil/bubble release (~ 24 hr). (d) Top view of the collected oil/bubbles. The inset shows the side view of the collected oil/bubble. (e) Mass spectroscopy analysis of collected gas bubbles

Figure 6.8 Mechanism of bubble growth and oil desorption with UV-responsive TiO<sub>2</sub>

Figure 6.9 (a) Underwater crude oil absorption of the 6/4 NS/p-PDMS, fully absorbed state, and oil desorption with air bubble flow/UV irradiation. (b) A schematic procedure of oil absorption and desorption with UV-responsive wettability and air bubble flow

Figure 6.10 (a) Oil absorption/desorption capacities and recyclabilities of the NS/p-PDMS (desorption by UV/bubbling) vs. a p-PDMS (desorption by squeezing or bubbling). (b) Oil desorption efficiency: bubbling and UV irradiation on the NS/p-PDMS sponge vs. squeezing the p-PDMS for oil desorption

Figure 6.11 (a) Underwater oleophilic nature of the p-PDMS after squeezing. (b) Underwater oleophobic nature of the 6/4 NS/p-PDMS after UV/bubbling

Figure 7.1 Schematic diagram and digital images of equi-biaxial tensile deformation device for EBSD measurement: (a) Sample shape for equi-biaxial tensile deformation. (b) Schematic diagram of equi-biaxial tensile deformation device controlled by rotation of screw. Digital images of equi-biaxial tensile deformation device (c) before and (d) after deformation

Figure 7.2 (a) Band contrast image and (b) histogram for martensite selection in DP steel. Blue color in (a) indicates martensite phase

Figure 7.3 EBSD orientation maps of IF and DP steels with martensite area fractions of (a) 0%, (b) 7%, (c) 18% and (d) 27% during equi-biaxial tensile deformation

Figure 7.4 Inverse pole figures of steel (a) with random orientation before equi-biaxial strain and (b) after equi-biaxial strain of 40%. Black arrows indicate rotation direction of

orientation. Red and blue dots indicate two different regions with  $\langle 001 \rangle // ND$  and  $\langle 111 \rangle // ND$  for equi-biaxial tensile deformation, respectively

Figure 7.5 ODF sections with  $\varphi_2 = 45^\circ$  obtained at the same area of (a) IF and (b) DP steels with 0% and 27% martensite area fraction before (left-hand column) and after (right-hand column) equi-biaxial tensile deformation

Figure 7.6 Inverse pole figures of measured initial and final orientation of several grains in (a) IF and (b-e) DP steels with 0% and 18% martensite area fraction

Figure 7.7 (a) EBSD BC image, (b) AFM topography and (c) AFM line profiles matching with line 1 and 2 in (b), respectively, measured in DP steel with 18% martensite area fraction after 5% equi-biaxial tensile deformation. F and M indicate ferrite and martensite, respectively

Figure 7.8 (a) EBSD orientation map of DP steel with martensite area fraction 18% after 5% biaxial deformation. Specimen surface was re-polished to eliminate the surface roughness.

(b) Calculated distribution of GND density in ferrite grain indicated as dashed box area in (a). (c) HAADF image of the dashed box area depicted in (b).

# **Chapter 1. Introduction**

## **1.1 Introduction to nanomaterials**

Nanotechnology aims to create and use structures and devices in the size range of about 0.1 – 100 nm where it covers atomic and molecular length scales, as well as integrate the resulting nanostructures into a large system for practical uses. Because of this focus on the nanometer scale, nanotechnology may meet the emerging needs of industries that have thrived on continued miniaturization<sup>1</sup>.

Nanomaterials are generally classified regarding to their dimensionalities as zero-dimensional (dots or spherical nanoparticles), one-dimensional (nanowires, nanotubes, and nanobelts), and two-dimensional (thin films). These classifications refer to the number of dimensions in which the material is outside the nano-regime. Nanomaterials have received steadily growing interests as a result of their peculiar and fascinating properties, and applications superior to their bulk counterparts<sup>2</sup>. Important changes in behavior are caused not only by continuous modification of characteristics with diminishing size, but also by the emergence of totally new phenomena such as quantum confinement<sup>3</sup>. A typical example of which is that the color of light emitting from semiconductor nanoparticles depends on their sizes as shown in Figure 1.1<sup>4</sup>. When sizes of solid in the visible scale are compared to what can be seen

in a regular optical microscope, there is little difference in the properties of the particles. But when materials are created with dimensions of about 1–100 nanometers, the properties change significantly from those in bulk. This is the size scale where so-called quantum effects rule the behavior and properties of materials. Properties of materials are also size-dependent in this nanometer scale. Thus, when size is made to be nanoscale, properties such as melting point, fluorescence, electrical conductivity, magnetic permeability, and chemical reactivity change as a function of the size of the particle<sup>4</sup>.

Nanomaterials have larger surface areas than similar masses of bulk materials. As surface area per mass of a material increases, a greater amount of the material can come into contact with surrounding materials, thus affecting reactivity<sup>4</sup>. A simple thought experiment shows why nanomaterials have phenomenally high surface areas. A solid cube of a material 1 cm on a side has 6 cm<sup>2</sup> of surface area. But if that volume of 1 cm<sup>3</sup> were filled with cubes 1 mm on a side, that would be for a total surface area of 60 cm<sup>2</sup>. When the 1 cm<sup>3</sup> is filled with micrometer-sized cubes, the total surface area amounts to 6 m<sup>2</sup>. And when that single cubic centimeter of volume is filled with 1-nanometer-sized cubes—their total surface area comes to 6,000 m<sup>2</sup> (Figure 1.2<sup>5</sup>). One benefit of greater surface area, and improved reactivity in nanostructured materials is creating better catalysts. Nano-engineered batteries, fuel cells, and catalysts can potentially use enhanced reactivity at the nanoscale to produce cleaner, safer, and more affordable modes of producing and storing energy.

But even if nano-systems and nano-devices with suitable performance characteristics are available, nanotechnology solutions will find practical advantages only if they are practically viable. We will need to develop methods for the controlled fabrication of functional nanostructures with tunable properties and their integration into usable macroscopic systems and devices.

In both technological and scientific standpoint, one dimensional nanowires are of great interest as building blocks for high-efficiency nanometer-scale devices. Because of their unique density of electronic states, nanowires are expected to exhibit significantly different optical, electrical and magnetic properties from their bulk counterparts. The increase surface area, very high density of electronic states, enhanced exciton binding energy, diameter-dependent band gap, and increased surface scattering for electrons and phonons<sup>4,6</sup> are some of the aspects in which nanowires differ from their corresponding bulk materials. Nanowires can provide a promising framework for the design of nanostructures and for potential nanotechnology applications. Therefore the development of methods for preparation of nanowire and further tunable properties is of significant broad interest at the present time.



Figure 1.1 Fluorescence of CdSe-Cds core-shell nanoparticles with a diameter of 1.7 nm up to 6 nm<sup>4</sup>

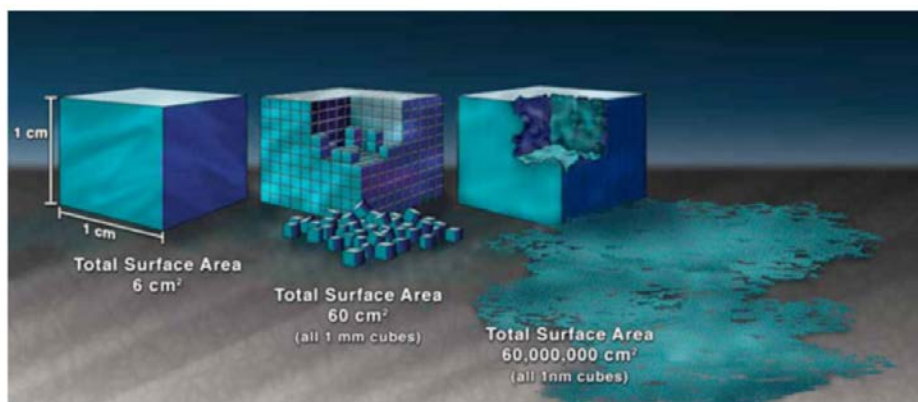


Figure 1.2 The effect of the increased surface area provided by nanostructured materials<sup>5</sup>

## 1.2 Thesis motivation

Deformation is one of the most fundamental aspects of materials. While mechanical failure is an outcome of deformation to be avoided, elastic deformation can have a pronounced and positive impact on materials properties. The effect of elastic deformation becomes even more evident at low dimensions, because at the nanomaterials can sustain exceptionally high elastic strain before failure. Rapid progress in device miniaturization has led to the quick rise of flexible, nanoscale devices for which one-dimensional (1-D) nanowires are particularly promising candidate materials. These nanowires possess unusual electronic properties due to large surface effects and quantum confinement.

Therefore, 1-D nanowires are one of the ideal platforms to explore novel stress effects and device concepts at the nanoscale, such as energy harvesting piezoelectric nano-generator<sup>7</sup>, stress induced phase transition<sup>8</sup>, and wrinkle based stretchable electronics<sup>9</sup>.

Until now, there are the great demand to manipulate the external stress or strain to expand the functionalities of nanowires including the synthesis process, fabrication. Therefore, we focused the effect of stress on one-dimensional nanowires from the growth and piezoresistive properties. The goal is to investigate the effect of stress on the nanowire growth and piezoresistivity of phase change materials to reveal the underlying mechanisms.

In a view of growth, we utilized the stress driven single crystalline indium

nanowire growth on InGaN substrate by ion beam irradiation. With comprehensive microstructural and chemical analysis, we confirmed that source of indium nanowire growth was originated from Ga<sup>+</sup> ion beam induced phase decomposition of InGaN substrate, and compressive stress build up by ion irradiation and atomic migration are responsible for the growth of indium nanowires as a process of stress relaxation. Since focused ion beam can be precisely controlled by changing the accelerating voltage, current density, and location of irradiation, the diameter and length of the nanowires as well as their growth rate could be effectively controlled. Indium nanowires with diameter of 40-200 nm and length up to 120 μm were fabricated at growth rate as high as 500 nm/s, which is remarkable fast compared with other nanowire growth methods.

Second, the effect of stress on the phase change nanowire (Ge<sub>2</sub>Sb<sub>2</sub>Te<sub>5</sub>) was explored to tune the electromechanical properties for the application to advanced electronic and memory devices. This is the first report that GST nanowires possess a large piezoresistive effect and strain dependent electrical switching behavior of PCM devices. For example, the longitudinal piezoresistance coefficient along  $\langle 10\bar{1}0 \rangle$  direction for GST nanowires reach as high as  $440 \times 10^{-11} \text{ Pa}^{-1}$ , which is comparable to the values of Si. The large piezoresistance and strain dependent behavior of PCM enable the potential application not only for flexible memory device, but also for another candidate

of piezoresistive materials for strain sensors.

This work can provide an important information to understand the stress related phenomenon as well as manipulating the external stress in 1D nanomaterials.

### 1.3 References

1. J.V. Barth, G. Costantini, K. Kern, *Nature* **437**, 671 (2005).
2. H.S. Nalwa, *Handbook of Nanostructured Materials and Nanotechnology*, Academic Press, New York (2000).
3. T. Takagahara, K. Takeda, *Phys. Rev. B* **46**, 578 (1992).
4. E. Roduner, *Chem. Soc. Rev.* **35**, 483 (2006).
5. Nanotechnology 101, National Nanotechnology Initiative
6. B. Bhushan, *Springer handbook of nanotechnology*, Springer Science & Business Media (2010).
7. Z.L. Wang, J. Song, *Science* **312**, 242 (2006).
8. J. Cao, E. Ertekin, V. Srinivasan, W. Fan, S. Huang, H. Zheng, J.W.L. Yim, D.R. Khanal, D.F. Ogletree, J.C. Grossman, J. Wu, *Nat. Nanotechnol.* **4**, 732 (2009).
9. Y. Sun, W.M. Choi, H. Jiang, Y.Y. Huang, J.A. Rogers, *Nat. Nanotechnol.* **1**, 201 (2006).

## **Chapter 2. Stress & strain engineering of one-dimensional (1-D) nanomaterials**

### **2.1 Introduction**

Deformation is one of the most fundamental aspects of materials. While mechanical failure is a result of deformation to be avoided, elastic deformation can have a pronounced and positive impact on materials properties and its applications. The effect of elastic deformation becomes even more evident at low dimensions, because at the micro/nanoscale, materials and structures can usually sustain ultra-high elastic strain (order of 8%) before yielding<sup>1,2</sup>. And this behavior is in contrast to conventional bulk materials, which can only deform on the order of 0.2% elastic strain.

Stress and Strain are a universal phenomenon pertinent to the synthesis, fabrication, and applications of all types of materials. Strain can have two distinct regimes: In the plastic regime, materials generally undergo irreversible changes, such as failure or property degradation. Elastic deformation, on the other hand, can induce reversible changes to materials properties. Especially, nanostructured materials, such as nanowires, nanotubes, have revealed a host of ultra-strength phenomena, defined by stress in a material component generally rising up to a significant fraction (1/10) of its ideal strength. Ultra-strength phenomena of nanomaterials not only have to do with the shape

stability and deformation kinetics of a component, but also the tuning of its physical and chemical properties by stress. Reaching ultra-strength enables “elastic strain engineering”, where by controlling the elastic strain field<sup>1</sup>.

A particularly successful application of strain engineering is pushing the limit of miniaturization of silicon-based field-effect transistors<sup>3</sup>. By alternating deposition of Si and Ge layers, the interlayer lattice mismatch creates controllable strain in the silicon crystal. The precisely controlled strain breaks the crystal field symmetry and reduces the scattering of carriers by phonons, resulting in substantially increased carrier mobility, which allows for further reduction in the channel size.

## **2.2 Stress/Strain effect in 1-D nanomaterials (nanowires)**

The strength of a material depends on its dimensions. Typically, smaller structures can tolerate larger deformations before yielding<sup>4</sup>. Therefore, it is anticipated that the effect of stress can be profitably explored in materials with reduced dimensions, such as one dimensional nanomaterials (nanowires).

Rapid progress in device miniaturization has led to the quick rise of flexible, nanoscale devices for which one-dimensional nanowires are particularly promising candidate materials. These nanomaterials possess unusual electronic properties due to large surface effects and quantum confinement. Owing to their reduced dimensions, these materials also exhibit superb mechanical properties

up to theoretical values. Therefore, 1-D nanowires are one of the ideal platforms to explore novel elastic strain effects and device concepts at the nanoscale.

### 2.2.1 Size effect of mechanical properties

Lieber's group<sup>5</sup> reported the size effects of mechanical properties of nanotubes and SiC nano-rods. They found that the strengths of SiC nanorods were substantially greater than those found previously for SiC bulk structures, and they approach theoretical values. The size effect of nanowires is also reflected in the variation of the Young's modulus upon bending with the nanowire diameter. Yu's group<sup>6</sup> systematically investigated the Young's modulus of metallic silver nanowires with different diameters by performing nanoscale three-point bending test on suspended nanowires. From measurement of the force applied with each push and the corresponding displacement, the apparent Young's modulus could be obtained as shown in Figure 2.1. It is observe that the apparent Young's modulus of the silver nanowires is found to decrease with the increase of the diameter (76 GPa for bulk, and ~160 GPa for nanowire with diameter of ~ 20 nm).

### 2.2.2 Piezoresistance

Large elastic strains can be used to tune the functional properties of nanowire. Application of strain to a crystal results in a change in electrical conductivity due to the piezoresistance effect. Yang's group<sup>7</sup> investigated the

piezoresistance of a single p-type silicon nanowire under uniaxial tensile/compressive strain and observed a so-called giant piezoresistance phenomenon (Figure 2.2). Longitudinal piezoresistance coefficient along the  $\langle 111 \rangle$  direction increases with decreasing diameter. And the strain induced carrier mobility change have been shown to have influence on piezoresistance coefficient. Liu *et al.* theoretically constructed an elastically strained silicon nanoribbon, consisting an alternating regions of unstrained and a strained Si, which creates a single element electronic heterojunction superlattice<sup>8</sup>. In such a strained configuration, it is predicted that, due to the strain effect and quantum confinement, it is possible to manipulate the motion of carriers by elastic strain.

### 2.2.3 Manipulation of metal insulator transition (MIT) temperature

By simple tip manipulation of the bending deformation of a single-crystal vanadium dioxide ( $\text{VO}_2$ ) nanowire<sup>9</sup>, they could nucleate and manipulate ordered arrays of metallic and insulating domains along single-crystal beams of  $\text{VO}_2$  by continuously tuning the strain over a wide range of values. This active control of external stress/strain allowed to reduce the metal–insulator transition temperature to room temperature, which normally happens at an elevated temperature in its bulk counterpart as shown in Figure 2.3.

### 2.2.4 Nano-generator

Wang *et al.* has used the elastic bending deformation of ZnO nanowires to create the nano-generators<sup>10</sup> as shown in Figure 2.4. They converted nanoscale mechanical energy into electrical energy by means of piezoelectric ZnO nanowire arrays. The aligned nanowires are deflected with a conductive AFM tip in contact mode. The coupling of piezoelectric and semiconducting properties in ZnO creates a strain field and charge separation across the nanowire as a result of its bending. The rectifying characteristic of the schottky barrier formed between the metal tip and the nanowire leads to electrical current generation. The efficiency of the nanowire-based piezoelectric power generator is estimated to be 17 to 30%. This approach has the potential of converting mechanical, vibrational, and/or hydraulic energy into electricity for powering nano-devices. Specifically, no output current is collected when the tungsten tip first touches the nanowire and pushes the nanowire, and power output occurs only when the tip touches the compressive side of the bent nanowire.

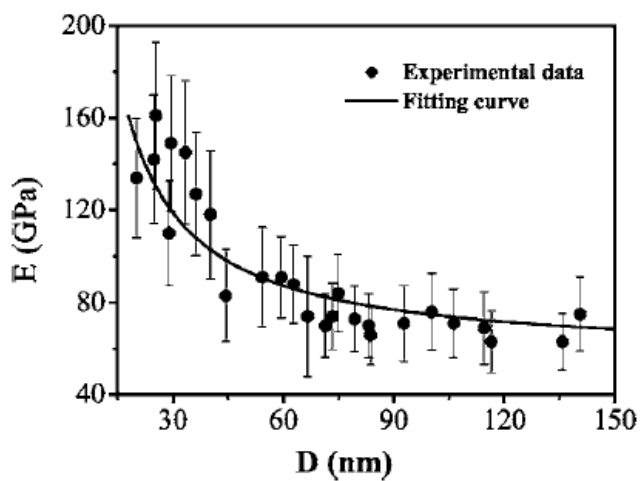
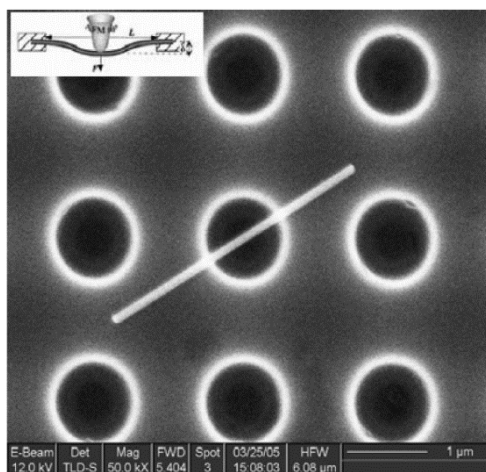


Figure 2.1 Variation of the Young's modulus as a function of the diameters silver nanowires<sup>6</sup>

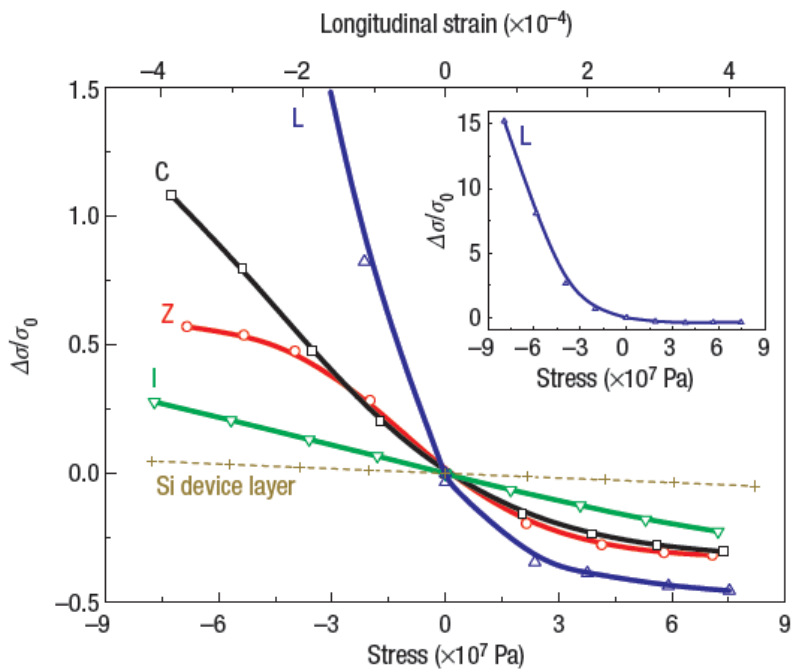


Figure 2.2 Giant piezoresistance of p-type silicon nanowire<sup>7</sup>

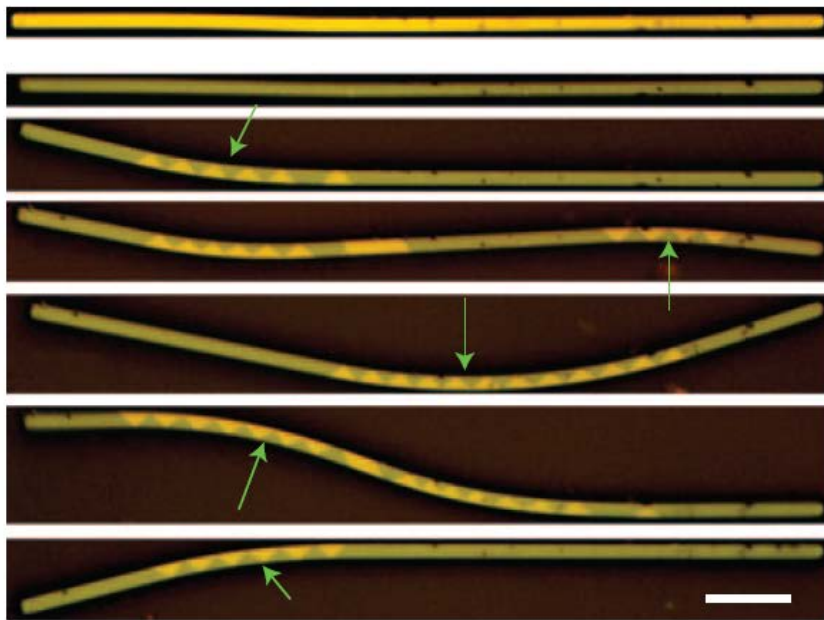


Figure 2.3 Stress (or Strain) manipulation of metal-insulator transition at room temperature in VO<sub>2</sub> nanowires<sup>9</sup>

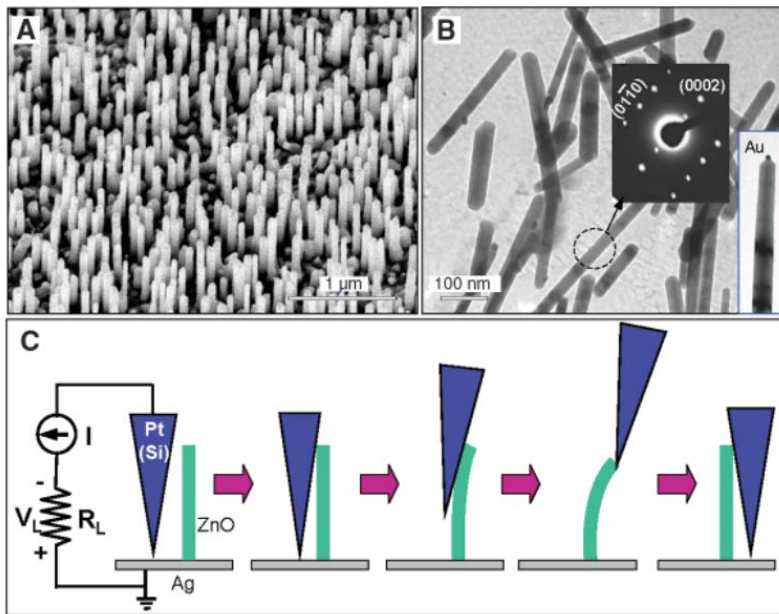


Figure 2.4 ZnO nanowires: nano-generator based on piezoelectric properties<sup>10</sup>

## 2.3 References

1. T. Zhu, J. Li, *Prog. Mater. Sci.* **55**, 710 (201).
2. D. Yu, J. Feng, J. Hone, *MRS Bulletin* **39**, 157 (2014).
3. M. Jeong, B. Doris, J. Kedzierski, K. Rim, M. Yang, *Science* **306**, 2057 (2004).
4. P. Hiralal, H.E. Unalan, G.A.J. Amaratunga, *Nanotechnology* **23**, 194002 (2012).
5. E.W. Wong, P.E. Sheehan, C.M. Lieber, *Science* **277**, 1971 (1997).
6. G.Y. Jing, H.L. Duan, X.M. Sun, Z.S. Zhang, J. Xu, Y.D. Li, J.X. Wang, D.P. Yu, *Phys. Rev. B* **73**, 235409 (2006).
7. R. He, P. Yang, *Nat. Nanotechnol.* **1**, 42 (2006).
8. Z. Liu, J. Wu, W. Duan, M.G. Lagally, F. Liu, *Phys. Rev. Lett.* **105**, 016802 (2010).
9. J. Cao, E. Ertekin, V. Srinivasan, W. Fan, S. Huang, H. Zheng, J.W.L. Yim, D.R. Khanal, D.F. Ogletree, J.C. Grossman, J. Wu, *Nat. Nanotechnol.* **4**, 732 (2009).
10. Z.L. Wang, J. Song, *Science* **312**, 242 (2006).

## **Chapter 3. Ion beam induced stress and indium nanowire growth**

### **3.1. Introduction**

Until now, several techniques to grow various types of nanowires have been reported for semiconductor nanowires as optoelectronic and electronic devices and metal nanowires as superconducting devices<sup>1</sup>, grown with various methods such as chemical vapor deposition (CVD)<sup>2</sup>, laser ablation<sup>3</sup>, electrochemical deposition<sup>4</sup>, etc. Fabrication methods for most of nanowires are based on the vapor-liquid-solid (VLS) mechanism in which various metals catalytically enhanced the growth of nanowires (details in chapter 3.2).

However, the difficulties to generate nanowires have been associated with the synthesis and fabrication of these nanostructures with well controlled dimension, morphology, phase purity, and chemical composition. Each method for 1-D nanostructure growth as introduced briefly above, has its specific merits and inevitable weaknesses. In terms of feasibility, methods based on the VLS process are the most versatile in growing various nanowires with controllable sizes and composition. However, they are not suitable for metal nanowires, as well as the catalyst may cause contamination for the nanowire product. On the other hand, methods using several templates also have the serious problem that removal of the templates through a post synthesis process may damage a

resultant nanowires while they provide a good control over the uniformity and dimension of nanowires. Still a key challenge in development of these devices, which are envisioned to impact human's life in the near future, is the development of economical techniques for controlled creation of their building blocks.

## **3.2 Conventional methods for nanowire synthesis**

### **3.2.1 Vapor-liquid-solid growth**

The growth of nanowires through a gas phase reaction including the vapor-liquid-solid (VLS) process has been the most widely studied. Wagner proposed in 1960s, a mechanism for the growth via gas phase reaction involving the so-called vapor-liquid-solid process<sup>5</sup>. He worked for the growth of mm-sized Si whiskers in the presence of Au particles. The mechanism described in this report is suggested that the anisotropic crystal growth is activated by the presence of the liquid alloy/solid interface, and this mechanism has been widely accepted and applied for understanding of various nanowires. The growth of Ge nanowires with Au clusters is understood based on the Ge-Au phase diagram in Figure 3.1<sup>6</sup>. Ge and Au form a liquid alloy when the temperature is higher than the eutectic point as shown in Figure 3.1 (I- alloying). The liquid surface has a large accommodation coefficient and is therefore a preferred site for the incoming Ge vapor. After the liquid alloy involving Ge and Au becomes

supersaturated state, precipitation of the Ge nanowire starts at the solid-liquid interface (Figure 3.1-II, III: nucleation & growth).

The only clue that nanowires grew by VLS mechanism is considered by the existence of alloy droplets at the top of the nanowire. Wu *et al.*<sup>6</sup> have reported real-time observation of Ge nanowire grown by in-situ heating TEM, which demonstrate the validity of the VLS growth mechanism. Wu's report shows that there are three growth steps: metal alloying, crystal nucleation, and axial growth (Figure 3.2).

Figure. 3.2 displays a sequential images of Ge nanowire growth grown by in-situ heating TEM. Three steps (I-III) are clearly demonstrated.

(I) Alloying process (Figure 3.2 (a)-(c)): The maximum temperature that could be gained in the system was 900 °C, which the Au clusters remain in the solid state in the absence of Ge vapor. As increasing amount of Ge vapor condensation and dissolution, Ge and Au form a liquid alloy. The volume of the alloy droplet increases, while the alloy composition moves, from left to right, to a biphasic regime (solid Au and Au/Ge liquid alloy) and a single-phase region (liquid). An isothermal line in the Au-Ge phase diagram in Figure 3.1 (b) shows the alloying process.

(II) Nucleation (Figure 3.2 (d)-(e)): the nucleation of the Ge nanowire begins when the concentration of Ge in Au/Ge alloy droplet becomes supersaturated. From the volume change of the Au/Ge liquid alloy, it is estimated that the

nucleation generally occurs at a Ge weight percentage with 50-60%.

(III) Axial growth (Figure 3.2 (d)-(f)): Once precipitation of Ge nanowire begins at the liquid/solid interface, further Ge vapor into the Au/Ge droplet alloy increases the amount of Ge precipitation from the alloy. The incoming Ge vapors diffuse and condense at the solid/liquid interface, which lead to secondary nucleation events. This report confirms the validity of the VLS growth mechanism at nanoscale.

Because the diameter of catalyst governs the diameter of nanowires, VLS manner is not only to provide an efficient ways to obtain uniform nanowires, but also to gain insight to extend the knowledge of the phase diagram of the reacting species. Physical methods, such as laser ablation, thermal evaporation, as well as chemical vapor deposition can be used to generate the reactant species in vapor form, required for the nanowire growth. From this perspective, various nanowires, such as elements, oxides, carbides, etc., have been successfully synthesized with VLS manner<sup>7-9</sup>.

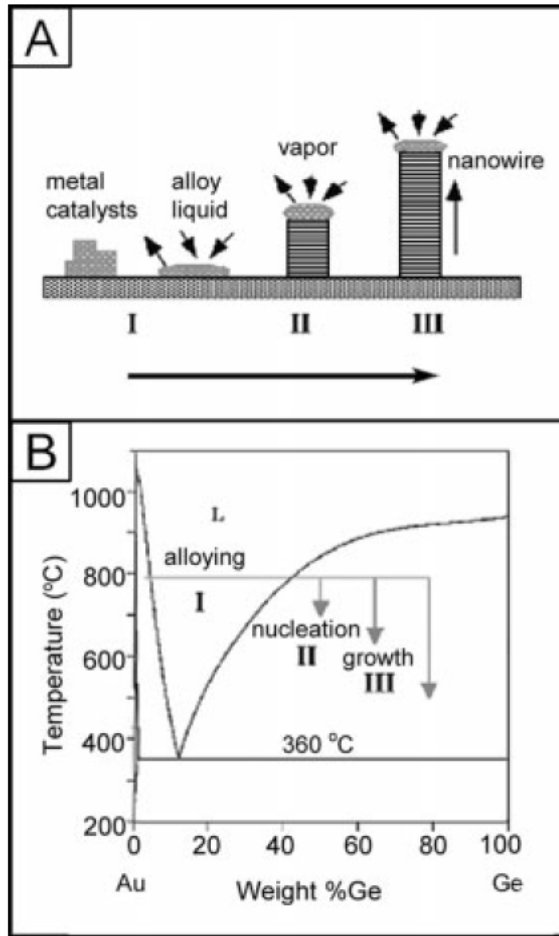


Figure 3.1 (a) Schematic illustration of vapor-liquid-solid growth mechanism including three stages. (b) The binary phase diagram between Au and Ge including three stages of (I) alloying, (II) nucleation, and (III) growth<sup>6</sup>

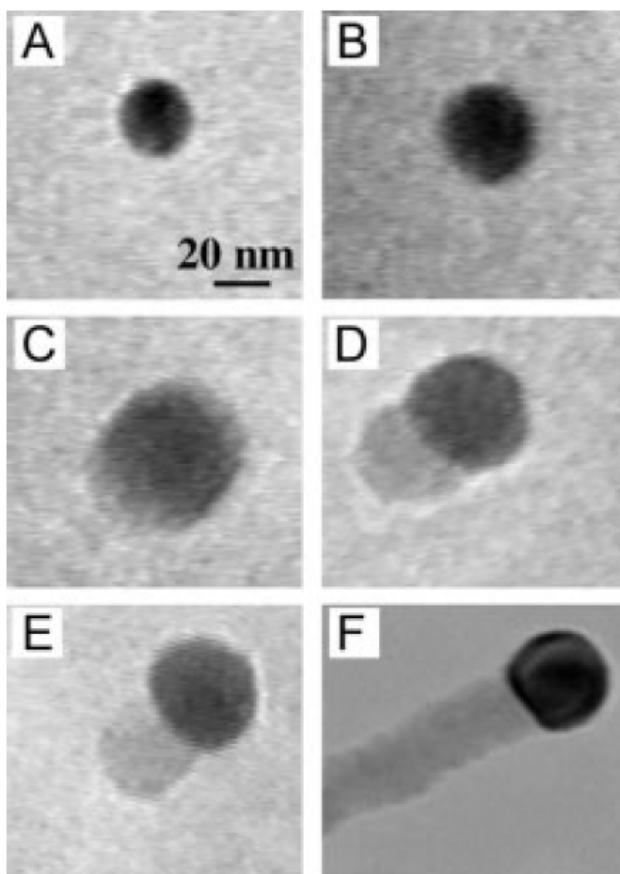


Figure 3.2 In-situ TEM images recorded during the process of nanowire growth. (a) Au nanoclusters in solid state at 500°C; (b) alloying initiated at 800°C, at this stage Au exists mostly in solid state; (c) liquid Au/Ge alloy; (d) the nucleation of Ge nanocrystal on the alloy surface; (e) Ge nanocrystal elongates with further Ge condensation and eventually forms a wire (f)<sup>6</sup>.

### 3.2.2 Vapor-solid growth

The nanowires can also be synthesized without catalysts by thermally evaporating a proper source materials near their melting point and depositing at cooler temperatures<sup>10</sup>. This method, the synthesis without liquid droplets corresponding to alloying, is referred to as a vapor-solid (VS) method. The VS method has been adopted to prepare whiskers of oxide, as well as metals with micrometer diameters. Even though no tight manner to control the spatial arrangement has been reported so far, it is worth mentioning that various nanowires can be obtained via VS manner if one can control the nucleation and the subsequent growth process<sup>11</sup>.

### 3.2.3 Oxide-assisted growth

In contrast to the well-established VLS growth, Lee and co-researchers have suggested a nanowire grown by the oxide-assisted mechanism<sup>12</sup>. At this report, these researchers find that the growth of Si nanowire is highly enhanced when Si powder target containing SiO<sub>2</sub> were utilized. Lee *et al.* proposed that the growth of the Si nanowire was assisted by the Si oxide, where the Si<sub>x</sub>O (x>1) vapor generated by thermal treatment plays the key role. Nucleation of the nanoparticles was assumed to occur on the substrate as shown in equation (3.1) and (3.2).





The precipitation of Si nanoparticles is attributed in these decompositions, which serve as the nuclei of the silicon nanowires sheathed by shells of silicon oxide. The precipitation suggesting that temperature gradient gives the external driving force for the formation and growth of the nanowires.

Figure 3.3 (a)-(c) reveal the TEM images of the formation of nanowire nuclei at the initial stages. Figure 3.3 (a) displays isolated Si nanoparticles covered by an amorphous silicon oxide layer, which have the growth normal direction to the substrate. The tip of the Si crystalline core possesses a high concentration of defects, as indicated by arrows in Figure 3.3 (c). Figure 3.4 shows a schematic diagram of the oxide-assisted mechanism. The Si nanowires growth is governed by four factors: (1) catalytic effect of the  $\text{Si}_x\text{O}$  ( $x>1$ ) layer on the nanowire tips (2) retardation of the lateral growth of nanowires by the  $\text{SiO}_2$  component in the shells (3) stacking faults of growth direction of  $\langle 112 \rangle$ , which contain  $1/6[112]$  and non-moving  $1/3[111]$  partial dislocations, and microtwins reveals at the tip areas coming fast growth of Si nanowires (4) the  $\{111\}$  plane with the lowest surface energy plays an important role during nucleation and growth, since the energy of the system is decelerated significantly when the  $\{111\}$  surfaces are parallel to the axis of the nanowires. The aforementioned last two factors are only working at lying in  $\langle 112 \rangle$  direction parallel to the growth direction.

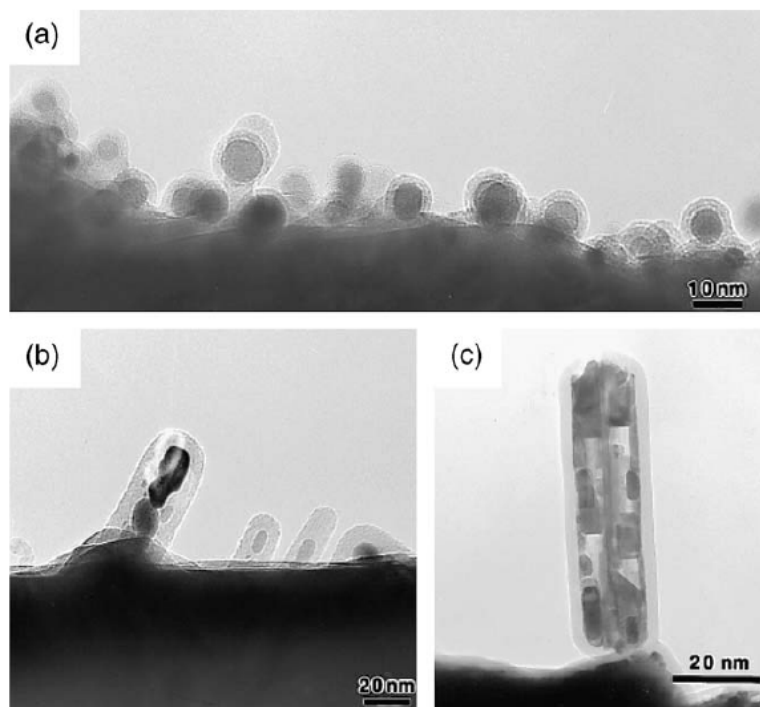


Figure 3.3 TEM images of (a) Si nanowire nuclei formed on the Mo grid and (b), (c) initial growth stages of the nanowires<sup>12</sup>

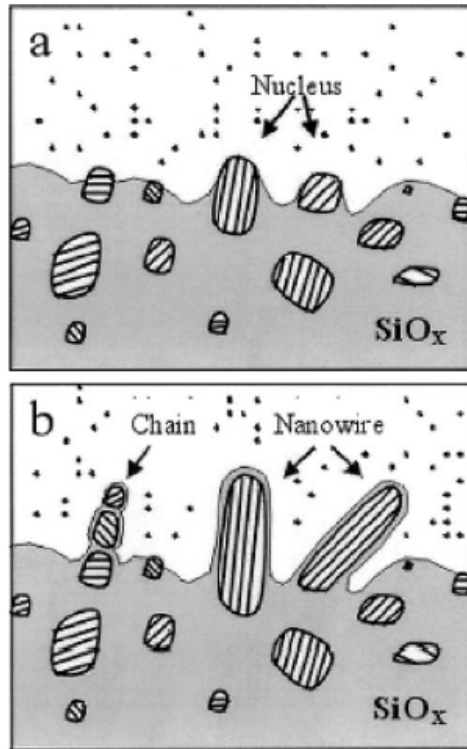


Figure 3.4 Schematic diagram of the nucleation and growth mechanism of Si nanowires. The parallel lines indicate the [112] orientation. (a) Si oxide vapor is deposited first and forms the matrix within which the Si nanoparticles are precipitated. (b) Nanoparticles in a preferred orientation grow fast and form nanowires. Nanoparticles with non-preferred orientations may form chains of nanoparticles<sup>12</sup>

### 3.2.4 Template-based synthesis

The growth of template-directed nanowires is the most widely studied strategy in solution based synthesis. In this manner, the template provides as a scaffold against which other materials with similar morphologies are synthesized. The in-situ generated material is formed into a nanostructure with morphology complementary to that of the template. The templates can be nanoscale channels within mesoporous materials such as porous alumina and polycarbonate membranes. For the formation of nanowires, the nanoscale channels are filled in terms of the solution, the sol-gel or the electrochemical manner. The desired nanowires can be synthesized after removal of the host matrix<sup>13</sup>. Unlike the polymer membranes made by etching, anodic alumina membrane (AAM) involving a hexagonally packed 2D array of cylindrical pores with a uniform size are fabricated using anodization of aluminum foils in an acidic medium (Figure 3.5).

The various materials such as elements, oxides, chalcogenides are synthesized by electronically conducting polymers such as polypyrrole, poly(3-methylthiophene) and polyaniline. The only drawback of template-based growth is difficulty of achieving materials with single-crystalline.

Additionally, alumina and polymer membranes with large surface areas and uniform pore sizes, mesoporous silica has been utilized as a template for the synthesis of nanowires. Mesophase structures self-assembled from surfactants

provide specific class of useful and versatile templates for producing 1-D nanostructures in relatively large quantities (Figure 3.6). It is well known that specific micell concentration surfactant molecules spontaneously organize into rod-shaped micelles<sup>14</sup>. These anisotropic structures can be employed as soft templates to promote the formation of nanowires when combined with suitable chemical or electrochemical reaction. The surfactant is required with selective removal to collect the nanowires. Through the template-based growth, various nanowires such as CdS, ZnS, and ZnSe have been synthesized by using surfactants such as Na-AOT and Triton X of known concentrations<sup>15</sup>.

Nanowires themselves can be exploited as templates to generate the nanowires of other materials. The template can be coated to the nanowire fabricating coaxial nanowires, or it can react with the nanowires forming a novel material<sup>16</sup>. From solution or sol-gel coating, nanowires can be directly sheathed with conformal coating layers made of a different material to form coaxial nanowires. Subsequent dissolution of the original nanowires results in nanotubes of the coated materials. The sol-gel coating provides a general way to synthesize coaxial nanowires that contain electrically conductive metal cores and insulating sheaths.

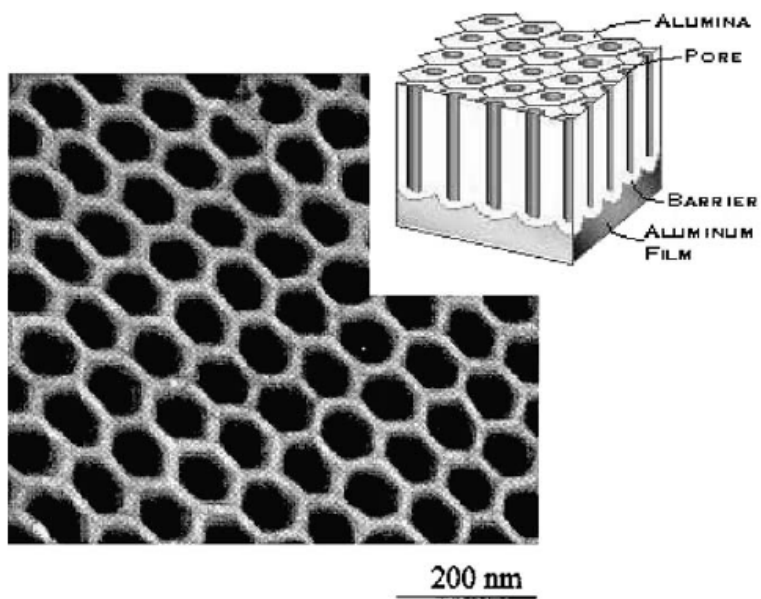


Figure 3.5 AFM image of an anodic alumina membrane (AAM)<sup>13</sup>

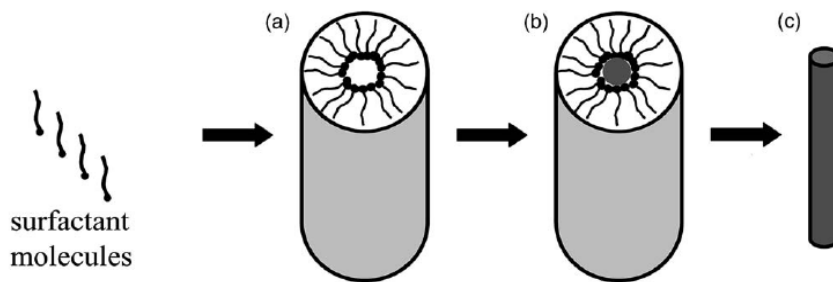


Figure 3.6 Schematic diagram showing the formation of nanowires by templating against mesostructures which are self-assembled from surfactant molecules. (a) Formation of cylindrical micelle; (b) formation of the desired material in the aqueous phase encapsulated by the cylindrical micelle; (c) removal of the surfactant molecule with an appropriate solvent to obtain an individual nanowire<sup>1</sup>

### 3.3. Stress driven nanowire growth

The formation of microscale metal whiskers on the surface of electrical components is a significant technological concern that can result in short circuits or electrical discontinuities<sup>17,18</sup>. The multilevel metal electrodes in large-scale integration may experience a significant amount of mechanical fatigue owing to the difference in the thermal expansion coefficients of the metals. With repeated device operation, thermally induced mechanical stress can develop to a level that causes substantial atomic diffusion to the extent where it leads to whisker formation. Whiskers are considered as a potential threat for device reliability. These whiskers are unintended and of uncontrollable size, and limited with respect to the type and number of materials that can be grown within microscopic field of view. The whiskers are, therefore, still at present the subject of remedial studies. From the point of view of materials scientists and engineers, whiskers are ideal for studying material properties, owing to their near perfect single crystal structure afforded by spontaneous thermodynamic growth. For example, stress-induced Sn<sup>18-20</sup>, and Al<sup>21</sup> whiskers are single crystals without lattice defects. This was shown by investigation of their elastic and plastic properties<sup>19</sup>. If whiskers with a nanoscale diameter are grown on a macroscopic length scale, it provides one with a platform to fully explore novel fundamental properties which can benefit from the high crystal quality offered by spontaneous growth.

### 3.3.1 Stress induced migration: atomic diffusion

With the newly reported works on various nanowires fabricated by utilizing stress migration<sup>21-23</sup> (Figure 3.7), the field of stress migration research has entered a new phase, not only in terms of its suppression, but also in terms of its applications. This is because one dimensional nano-structures have attracted considerable attention due to their unique mechanical, electrical, and magnetic properties, and their fundamental importance to MEMS/NEMS in recent years.

It has been demonstrated that whisker growth is driven by compressive stress gradients. The origin of the compressive stress can be mechanical, thermal, and chemical<sup>24</sup>. Based on the Tu's work<sup>25</sup>, in order for Sn whiskers to grow, there must be a chemical reaction between the bonded elements to guarantee the necessary stress generation. Moreover, because Sn whisker growth is a spontaneous process, the stress that is generated is internal and so the geometrical properties of whiskers are uncontrollable. All of the characteristics described above have certain limitations that must be taken into account in consideration of nanowire formation by utilizing stress migration, such as the choice of source material, the growth rate, the generation of the driving force and controllability.

In contrast to 'traditional' Sn whisker growth, alternative approaches have been developed in which an external applied stress is used to induce atomic diffusion. Almost all of these fabrication techniques aimed at utilizing the

thermal stresses that result from a mismatch in thermal expansion coefficients in bilayer/multilayer structures. Let us refer to the work by Shim *et al.*<sup>26</sup> to give a schematic representation of the nanowire growth mechanism. As illustrated in Figure 3.8, a tri-layer structure with an oxidized Si substrate followed by a Bi layer is used. It should be mentioned that there is a large difference between the thermal expansion coefficients of Bi ( $13.4 \mu\text{m m}^{-1} \text{K}^{-1}$ ) and  $\text{SiO}_2/\text{Si}$  ( $0.5 \mu\text{m m}^{-1} \text{K}^{-1} / 2.4 \mu\text{m m}^{-1} \text{K}^{-1}$ ). The Bi film expands while it is annealed in the temperature range 260-270°C, while the substrate restricts expansion, putting the Bi film under compressive stress. By making use of stress relief and atomic diffusion, Bi nanowires can be fabricated. The mass of Bi nanowires that are formed have high aspect ratios (length/diameter), as shown in Figure 3.8 (b). Figure 3.8 (c) shows TEM analysis of a formed Bi nanowire. The nanowire was found to be uniform in diameter and to have formed a 10 nm thick Bi oxide layer on its outer surface.

It is noteworthy that the growth of stress migration-induced nanowires is governed by temperature, film thickness, grain size and the time that the film is subjected to stress during the process. Therefore, by adjusting these parameters, the growth of nanowires can be controlled.

Since the atomic diffusion induced by stress migration is a stress relief phenomenon, it must relate to the stress gradient. To be precise, it occurs due to a gradient of compressive hydrostatic stress. Denoting the hydrostatic stress

by  $\sigma$  and considering a material with a distribution of compressive stress as shown in Figure 3.9<sup>27</sup>, the atoms diffuse from position A with more-negative stress (higher compressive stress) towards position B with less-negative stress (lower compressive stress). As a result, a local atomic accumulation is caused at position B. The hydrostatic stress is expressed as  $\sigma = (\sigma_x + \sigma_y + \sigma_z)/3$ , where  $\sigma_x$ ,  $\sigma_y$  and  $\sigma_z$  are the corresponding normal stresses in the Cartesian coordinates system (x, y, z). In most of these cases, the surface of a material subjected to stress migration is covered by an oxide layer or by a passivation layer. In those cases, the normal stresses  $\sigma_x$ ,  $\sigma_y$  and  $\sigma_z$  caused by the accumulation of atoms are the same as each other,  $\sigma_x = \sigma_y = \sigma_z$ , and hence  $\sigma$  is equal to  $\sigma_x$ , where x is usually taken in the longitudinal direction of the tested material and z is in the normal direction to the surface of the material. The stress migration induced atomic flux,  $J_s$  is given by<sup>23,27</sup>

$$J_s = \frac{N\Omega D_0}{k_B T} \exp\left(-\frac{Q-\Omega\sigma}{k_B T}\right) \text{grad } \sigma \quad (3.3)$$

Where  $N$  is the atomic concentration,  $\Omega$  is the atomic volume,  $k_B$  is Boltzmann's constant,  $T$  is the absolute temperature,  $D_0$  is the self-diffusion coefficient,  $Q$  is the activation energy and  $\sigma$  is the hydrostatic stress. Here, the gradient of  $\sigma$  is the driving force for atomic diffusion, and this differs with the electron flow, which is used to describe that of electro-migration.

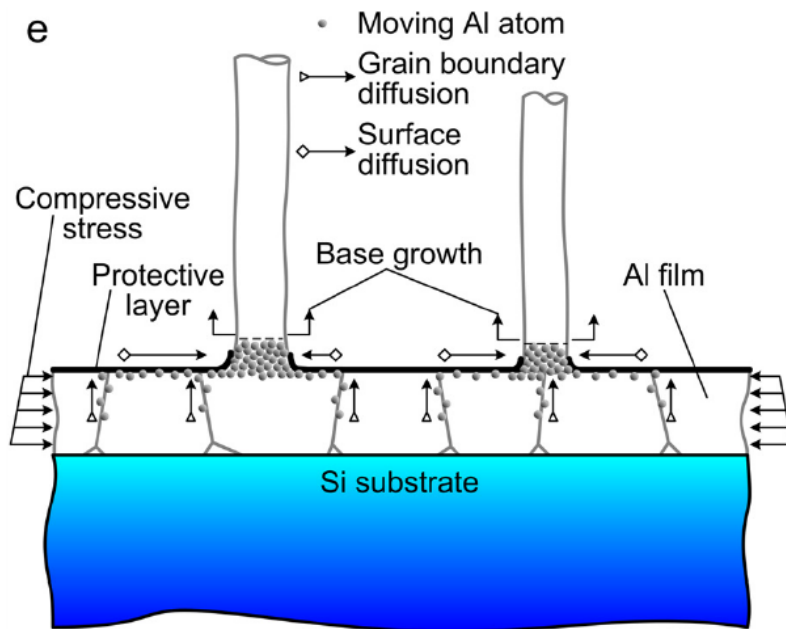


Figure 3.7 Growth process of the Al nanowire: illustration of the growth mechanism (the extrusion of atoms from the bases of nanowires)<sup>21</sup>

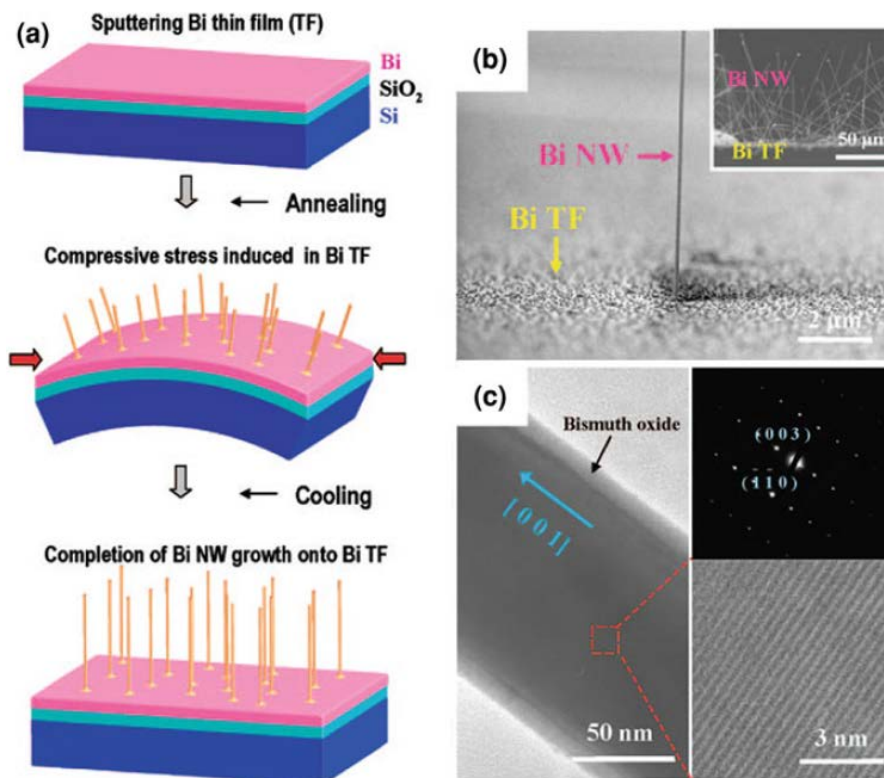


Figure 3.8 Growth mechanism and structural characteristic of the single crystalline Bi nanowires (a) a schematic representation of the growth of Bi nanowires by on-film formation of nanowires, (b) SEM image of a Bi nanowire grown on Bi thin film, and (c) a low magnification TEM image of Bi nanowire<sup>26</sup>

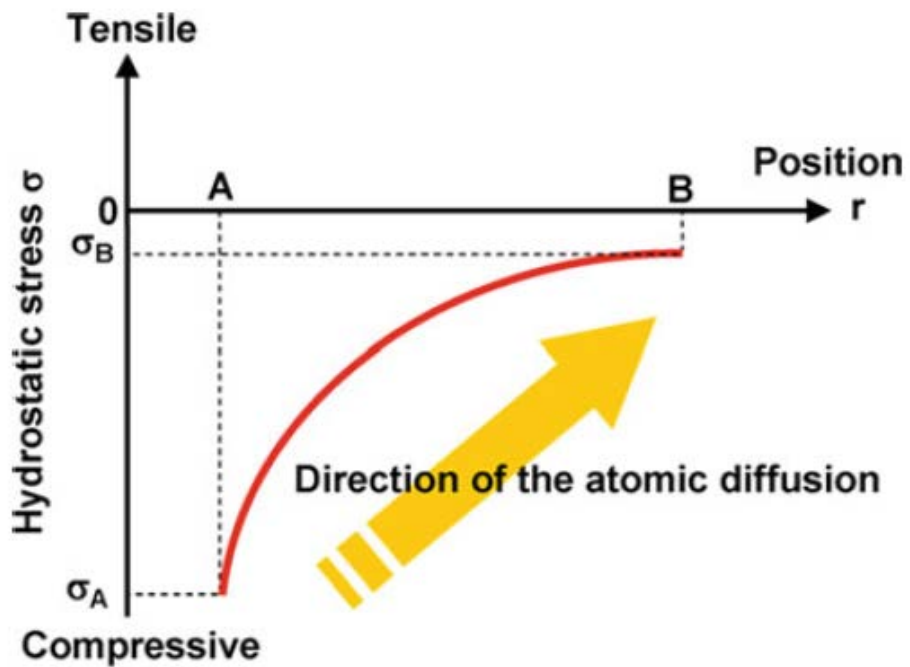


Figure 3.9 Illustration for the phenomenon of stress migration in a material with a distribution of compressive stress<sup>23,27</sup>

## 3.4 Ion implantation induced stress

### 3.4.1. Origin of stress evolution in ion irradiated surface

Changes in the state of stress in materials under irradiation derive from a number of mechanisms; accumulation of defects, the redistribution of material near surfaces, and phase transformation (amorphization)<sup>28</sup>.

It is known that ion implantation can induce high levels of stress in the surface. This stress has been shown to be compressive for most ion-target combination<sup>29</sup>. Compressive stresses are usually attributed to extensive defect production, together with the ion stuffing effect of the implanted species. The depth of material modified by highly energetic implantation process is thin (typically  $\sim 0.5 \mu\text{m}$ ), and the biaxial compressive stresses produced in this layer can be of the order of 1 to 10 GPa.

Ion implantation is a low temperature vacuum surface treatment process involving ion energies typically in the range 50 to 500 keV. Energetic ions penetrate the surface of the target material and come to rest in an approximately Gaussian distribution<sup>30</sup>.

The implanted ions lose energy by two mechanisms prior to coming to rest. Firstly, inelastic collision result in the displacement of host atoms from their structure-sites. These displaced atoms may then proceed to displace other host atoms until, finally, the energies of both the incident ions and the recoiling host

atoms are insufficient to produce further displacements. Secondly, fast-moving ions may lose energy by electronic excitation of the host material. This can result in the weakening of the host atom bonding by ionization and the formation of charged defects such as colour centres. Such processes are more efficient at higher ion energies with displacements prevalent at lower energies, the competition between the processes (combined with the statistical nature of the collision processes) producing the typically Gaussian damage and concentration profiles usually assumed.

As implantation proceeds, the accumulation of displacement damage may lead to the host material (if crystalline) eventually becoming amorphous<sup>30</sup>. This has been observed by a number of workers for a wide range of both covalently-bonded and ionically-bonded materials (e.g. silicon<sup>31</sup>, Al<sub>2</sub>O<sub>3</sub><sup>31</sup>, and SiC<sup>32</sup>). Amorphization is expected to occur first at the peak of the displacement damage profile beneath the host surface, i.e. initially a sub-surface amorphous zone occurs once the damage peak exceeds some critical, material-dependent, value. The thickness of this zone increases with subsequent increases in dose, until, when the damage level at the surface exceeds the critical value, a surface amorphous layer will be formed. Consequently it can be seen that, as the implantation dose is increased, three distinct microstructural regimes occur; these are summarized in Figure 3.10<sup>28</sup>. Finally, the generation of the point defects by displacement processes results in a volume change within the implanted layer. Volume expansions of up to 30% have been reported<sup>32</sup>.

However, if this change is constrained by either underlying or surrounding material, as is usual, large stresses may be generated in this relatively thin implanted layer<sup>29</sup>.

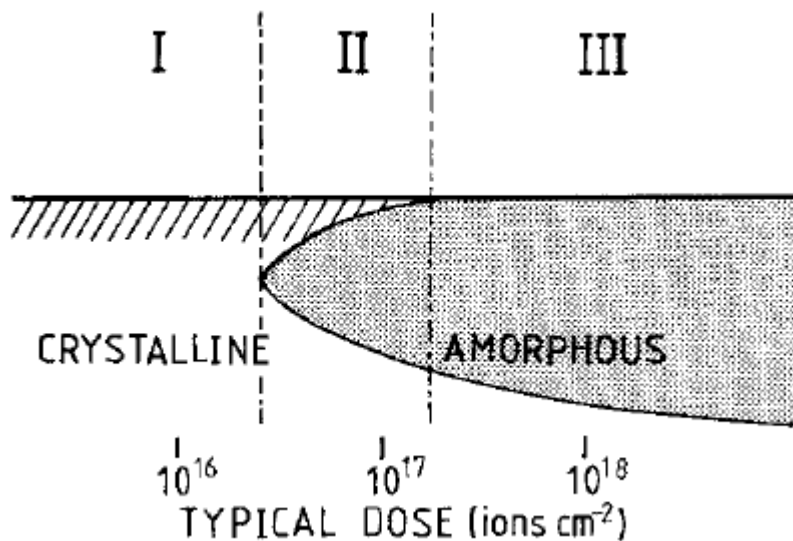


Figure 3.10 A schematic representation of the three microstructural regimes that arise from ion-implantation into crystalline materials. In Region I (low dose), a damaged but still crystalline solid solution is formed. In Region II (intermediate doses), amorphous material is initially formed at the peak of the displacement damage profile, In Region III (sufficiently high doses), a true surface amorphous layer is formed<sup>28</sup>

## 3.5 Experimental procedure

### 3.5.1. Preparation of InGaN substrate

300 nm thick In-rich InGaN layers (Figure 3.11), as a target template for FIB irradiation, were grown by low-pressure metal organic chemical vapor deposition (MOCVD)<sup>33</sup>. Trimethylgallium (TMGa), trimethylindium (TMIn) and ammonia were used as Ga, In, and N sources, respectively. In-rich InGaN growth was performed on 2  $\mu\text{m}$  thick GaN layers were grown on (0001) sapphire substrate at 1080 $^{\circ}\text{C}$  before the growth of In-rich InGaN layers. Growth temperature of In-rich InGaN was 640 $^{\circ}\text{C}$  and input TMIn flow rate was in the range of 1 $\mu\text{mol}/\text{min}$ ~10 $\mu\text{mol}/\text{min}$ . Input TMGa flow rate and reactor pressure were kept constant at 3  $\mu\text{mol}/\text{min}$  and 300 Torr, respectively. InGaN layers were grown for 20 min. Thickness was 300 nm by controlling the growth temperature and TMIn flow rate. During the InGaN layer growth,  $\text{N}_2$  was used as a carrier gas. Synthesized InGaN layers are saturated with ~80% indium confirmed by X-ray diffraction technique (Figure 3.12), and its roughness in RMS scale was measured as 30nm using Atomic Force Microscopy (AutoProbe CP research system, ThermoMicroscopes).

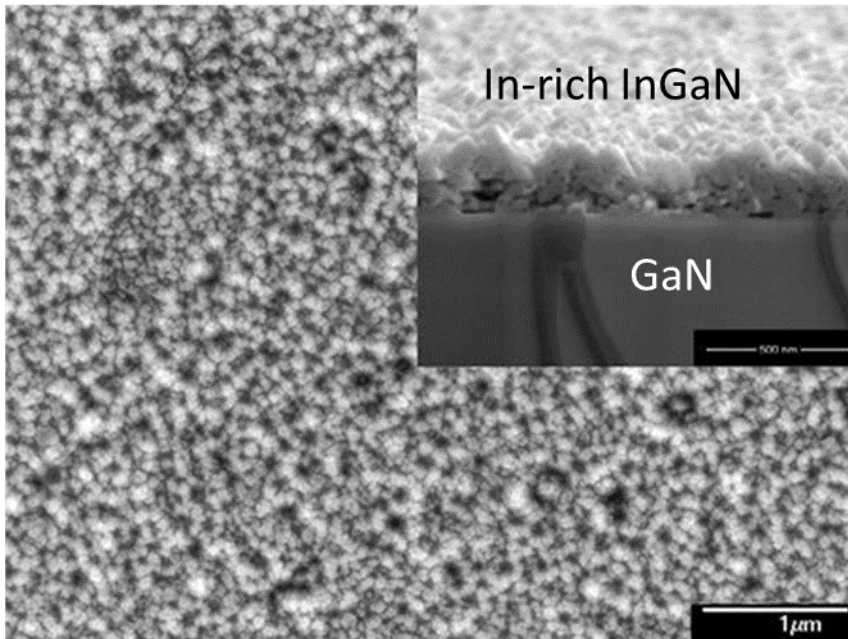


Figure 3.11 Plane view SEM image of In-rich InGaN film grown by MOCVD. The inset shows the cross-section view of specimen<sup>33</sup>

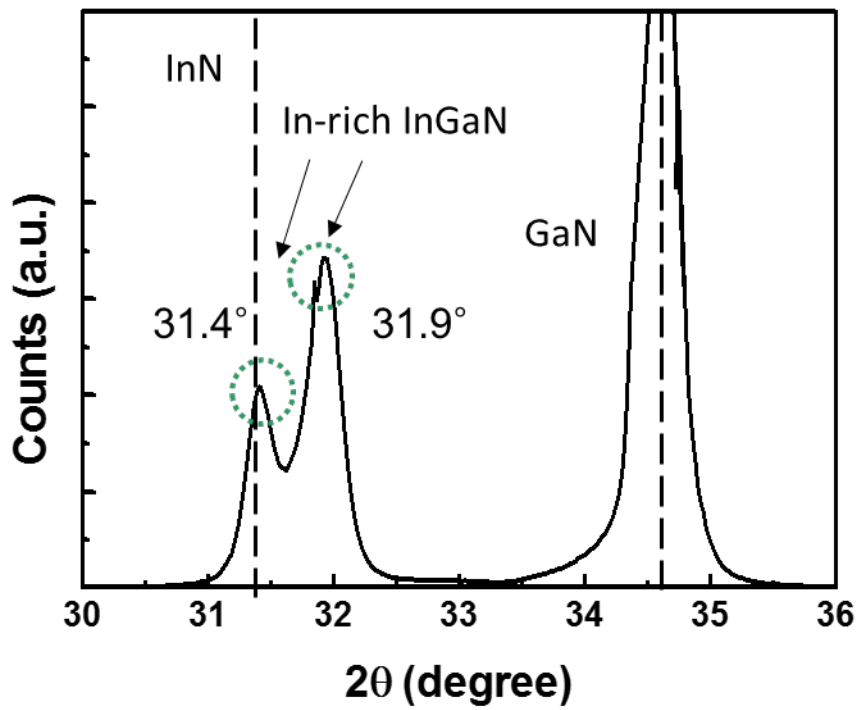


Figure 3.12 XRD measurement of In-rich InGaN<sup>33</sup>

### 3.5.2. FIB/SEM dual beam system: nanowire growth

Focused ion beam (FIB) / scanning electron microscope (FE-SEM) dual beam system (FEI Nova 200 NanoLab) in Figure 3.13 was used to grow indium nanowires in In-rich InGaN films. Schottkey type field-emission gun with the resolution of 1.1 nm and Magnum ion gun with gallium (Ga) liquid metal ion source, guaranteeing the resolution of 7 nm, are installed with the angular geometry of  $52^\circ$ . Both of ion and electron beam energy and their probe currents ranged from 5 kV to 30 kV and from 1 pA to 20 nA, respectively. This dual beam system does not only support 3D imaging analysis, but FIB system also utilizes a finely focused beam of Ga ions operated at low beam currents for imaging and at high beam currents for site specific milling. 5-axis motorized stage, gas injection system (GIS) for platinum deposition and in-situ nano-manipulator (Onmi-probe Model 100.7) are equipped for versatile use in this system as well as energy dispersive x-ray spectroscopy (EDS) and electron backscattered diffraction (EBSD) for nano-analysis capabilities.

### 3.5.3. Methods for the structural and chemical characterization

- Focused ion beam irradiation: Indium rich InGaN layers were exposed to FIB of Ga<sup>+</sup> ion with various ion current densities and accelerating voltages at room temperature using high resolution FIB/FE-SEM dual beam system equipped with a Ga liquid metal source. Pressure range inside the vacuum chamber was

maintained within  $2.0 \times 10^{-4}$  to  $6.0 \times 10^{-4}$  Pa during the experiment. During exposure to FIB, the formation of nanowires was monitored *in-situ* by a FE-SEM system.

- Characterization of synthesized nanowires: Since FIB/SEM could provide simultaneous secondary electron images and ion irradiation, *in-situ* monitoring of indium nanowire growth is possible during Ga ion irradiation. To characterize the size of indium nanowire, SEM images of nanowires at the same location were captured both in tilting angle  $0^\circ$  and  $52^\circ$ , and diameter and length of nanowires were calculated. To investigate the growth mechanism including indium source, nanowire growth direction, TEM specimens were prepared using FIB/SEM lift out technique. The target nanowire was detached from InGaN film by manipulating an Omni-probe, and detached nanowire was picked up by the attractive electrostatic force between the probe and the nanowire. The probe with the nanowire approached to a TEM Cu grid, and the nanowire was pasted with electron beam induced Pt deposition. The TEM sampling procedure is shown in Figure 3.14. For performing TEM analysis, the thickness of nanowires was reduced to 5~60 nm by milling using FIB for the analysis in TEM and EDS. This procedure was performed at the temperature of  $-90^\circ\text{C}$ , using a cooling stage to prevent the nanowire from melting with high temperature during milling. Then, the cross-section of the nanowires with the thickness  $\sim 60$  nm was examined using TEM (JEM-3000F, JEOL). The

chemical composition of nanowires was analyzed using energy dispersive x-ray spectroscopy (EDS, OXFORD). The structural properties of nanowires were confirmed by high-resolution TEM and electron diffraction pattern. The compositional change of InGaN layer during FIB irradiation was examined by electron energy loss spectroscopy (EELS) using high voltage electron microscope (HVEM, JEOL).

- Creation of functional networks of nanowires: Functional network of individual nanowires were created by adopting the maskless patterning method of the FIB equipment. This method permits the accurate selection of the areas exposed to FIB. The bitmap file of the exposure pattern was imported as a virtual mask in the FIB system. The ion beam was raster-scanned over the cross-shaped area with dwell time of 1  $\mu$ s.

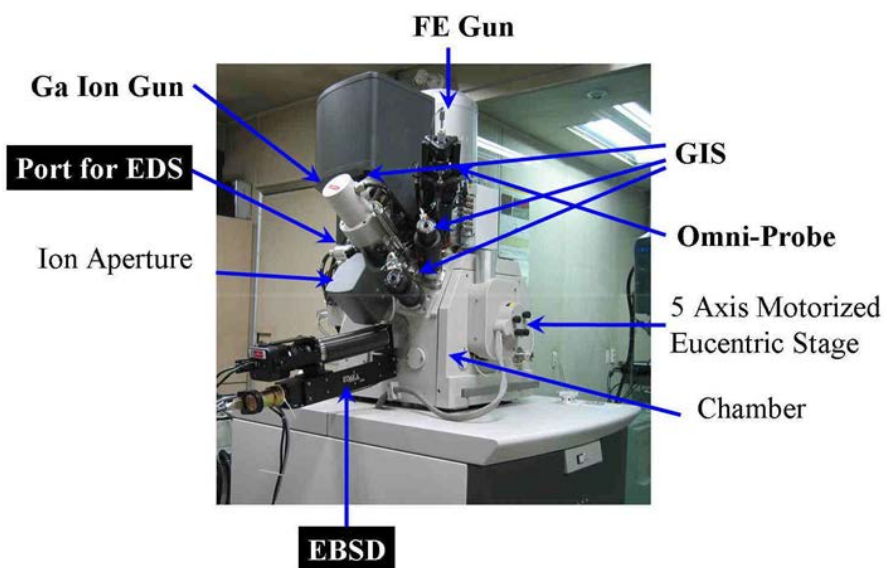


Figure 3.13 FIB/SEM dual beam system for nanowire growth

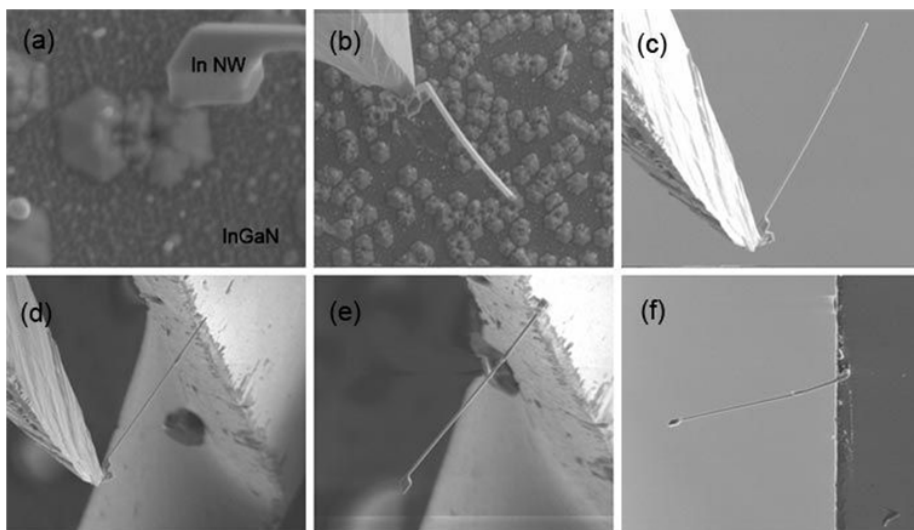


Figure 3.14 Procedure of nanowire TEM sampling: (a) the bottom of nanowire on InGaN film (b) Detachment of nanowire from substrate by Omni-probe, (c) The nanowire pick-up and transfer, (d) approaching to the Cu grid, (e) Pt deposition for nanowire to grid (f) completion of TEM sampling

## 3.6 Results and Discussion

### 3.6.1. Growth of nanowire

Indium rich InGaN surface was exposed to FIB with various ion current densities and accelerating voltage at room temperature without cooling or heating using a FIB/SEM dual beam system equipped with a Ga liquid metal source. The status and position of sample could be monitored in-situ by SEM in the condition described below. Pressure range inside the vacuum chamber was maintained with  $3.75 \times 10^{-5} \sim 2.75 \times 10^{-3}$  Pa, the accelerating voltage and current of the  $\text{Ga}^+$  ion beam were ranged 5 ~ 30 kV and 3 pA ~ 1 nA, respectively, while the working distance between ion gun and the sample surface was kept 19.5 mm. Exposure time was changed from several seconds to several tens of minutes at a fixed accelerating voltage.

The formation of nanowires was confirmed by in-situ SEM observation. The schematic of generation of nanowires using FIB on the surface area of the InGaN substrate is shown in Figure 3.15. During  $\text{Ga}^+$  ion beam irradiation on InGaN template, nanowires were growing as increased the irradiation time, and these nanowire were grown only on FIB-exposed region of InGaN layer. From the onset of irradiation, nanowires start to appear after 80 s and grow at an average rate of 50 nm/s until 260 s, at which point the indium source in the InGaN layer is exhausted as will be explained later. Figure 3.16 shows four snapshots of the growth sequence for nanowires taken at 50 s time intervals at

the ion current density of  $200 \text{ nA cm}^{-2}$  and an accelerating voltage of 10 kV, where the synthesized nanowires have lengths as large as  $30 \text{ }\mu\text{m}$  and diameters in the range 50~200 nm. By controlling the current density and accelerating voltages of  $\text{Ga}^+$  ion beam, the geometries of nanowires could be selected with the condition for longer length than  $130 \text{ }\mu\text{m}$  and thicker diameter than 300 nm. And for smaller length of  $20 \text{ }\mu\text{m}$  in length but as thin as 100 nm in diameter in Figure 3.16.

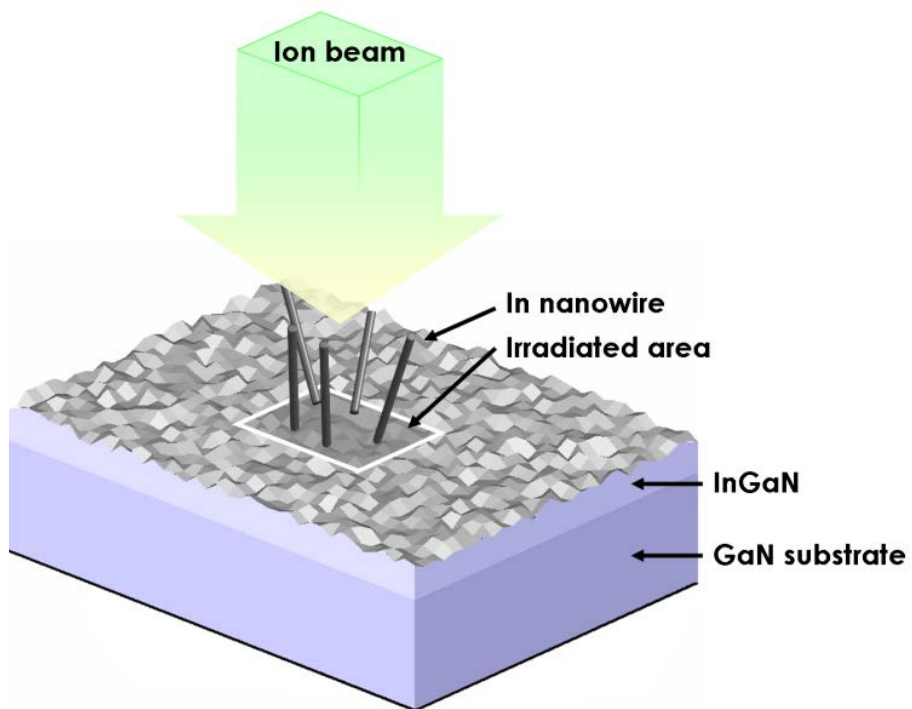


Figure 3.15 Schematic illustration of indium nanowire growth induced by FIB irradiation

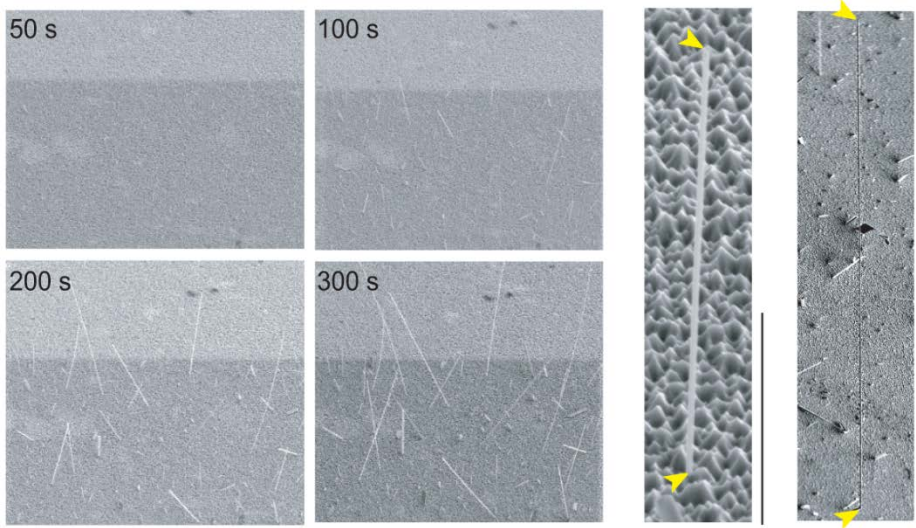


Figure 3.16 Time evolution of formation of straight nanowires after exposure to FIB with accelerating voltage of 10 kV and ion current density of  $200 \text{ nA cm}^{-2}$ , Scale bar =  $20 \mu\text{m}$  (left ) and  $10 \mu\text{m}$  (right)

### 3.6.2. Identification of nanowire

To identify the composition of nanowires induced by FIB irradiation, HR-TEM measurement was performed. As shown in Figure 3.17, the electron diffraction pattern from a nanowire with [110] zone axis confirmed that single crystalline nature of the indium nanowire. It could be indexed in terms of the body-centered tetragonal structure with lattice constants of  $a=0.325$  nm, and  $c=0.495$  nm, which agreed well with the reported values of indium bulk crystal. EDS built in to HR-TEM was also used for the identification of nanowires induced by FIB irradiation as an indium structure. In EDS spectrum, Cu peak was the artifact originated from Cu TEM grid. The detailed TEM observation indicated that indium nanowires grew along the  $[\bar{1}12]$  direction.

### 3.6.3 Controlled nanowire growth: dimensions and growth rate

The geometrical characteristics and growth rate of synthesized nanowires have been plotted as a function of  $\text{Ga}^+$  ion beam parameters, namely ion current density and accelerating voltage. Figure 3.18 (a) shows the length of individual straight nanowires synthesized on a  $420 \mu\text{m} \times 360 \mu\text{m}$  area by FIB irradiation with various accelerating voltages at a fixed ion current density of  $15 \text{ nA cm}^{-2}$ . At this ion current density, the average length of the synthesized nanowires increases by increasing the accelerating voltage: from  $0.503 \mu\text{m}$  at 5 kV to  $60.28 \mu\text{m}$  at 30 kV (The plot displays that length such that 10% of the wires

have equal or larger length). Furthermore, straight nanowires with lengths greater than 100  $\mu\text{m}$  were synthesized for acceleration voltages of 20 kV and 30 kV. The density of indium nanowires synthesized at all four accelerating voltages was also estimated (Figure. 3.18 (a)). At a low accelerating voltage of 5 kV, the nanowire density, defined as number of wires per unit area, is  $\sim 5.76 \mu\text{m}^{-2}$ . While for all other three accelerating voltages, the nanowires density is at least one order of magnitude lower and decreases by increasing the accelerating voltage. A simple calculation for the total mass of the synthesized nanowires per unit area based on the average diameter and length of the nanowires and the measured density yields  $2.2 \times 10^{-2} \text{ g m}^{-2}$  and  $8.7 \times 10^{-2} \text{ g m}^{-2}$  for the accelerating voltage of 5 and 30 kV, which are in the same order of magnitude as the indium content in the surface layer. We further measured the average length and diameter of the synthesized nanowires over a wider range of ion beam parameters. The results are summarized in Figure 3.18 (b). The dimensions of the synthesized nanowires depend on the ion beam parameters in a complex fashion. For current density of  $35 \text{ nA cm}^{-2}$ , increasing the accelerating voltage leads to thicker and longer indium nanowires, suggesting that the accelerating voltage is closely tied to the driving force in the process. This trend diminishes at higher current densities, since at high accelerating voltage and current density, the  $\text{Ga}^+$  ions etch the indium nanowires as well as the InGaN surface. This effect becomes significant at voltages exceeding 20 kV

for current densities  $350 \text{ nA cm}^{-2}$  and higher. In this range the effect of cutting and etching becomes dominant undermining the growth rate which is driven by accelerating voltage<sup>34,35</sup>.

Finally, the average growth rate of the nanowires was measured over a range of ion beam parameters, Figure 3.18 (c). Here, the growth rate is averaged over 5 distinct sets of experiment, all having the same ion current and accelerating voltage. The measured growth rate is an intricate function of ion beam parameters due to the complex interplay of the growth and erosion mechanisms discussed above. For example at the fixed voltage of 10 kV, the growth rate increases monotonically from  $50 \text{ nm s}^{-1}$  to  $400 \text{ nm s}^{-1}$  as the ion current density is increased from 15 to  $7000 \text{ nA cm}^{-2}$ . Further increase in the current density leads to gradual reduction of the growth rate as the surface of InGaN substrate started to be milled (eroded) by FIB irradiation, leading to considerable morphological changes of the substrate surface. The maximum growth rate achieved in the range of ion beam parameters in Figure 3.18 (c) is  $\sim 500 \text{ nm s}^{-1}$  at the accelerating voltage of 20 kV and current density of  $2000 \text{ nA cm}^{-2}$ . This growth rate is several orders faster than the current techniques<sup>36,37</sup>.

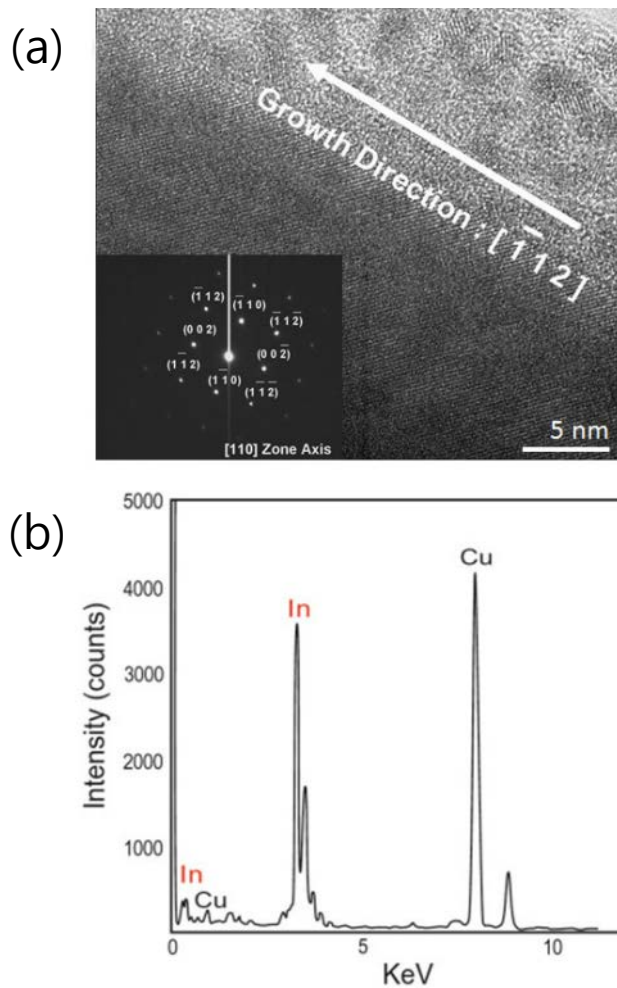
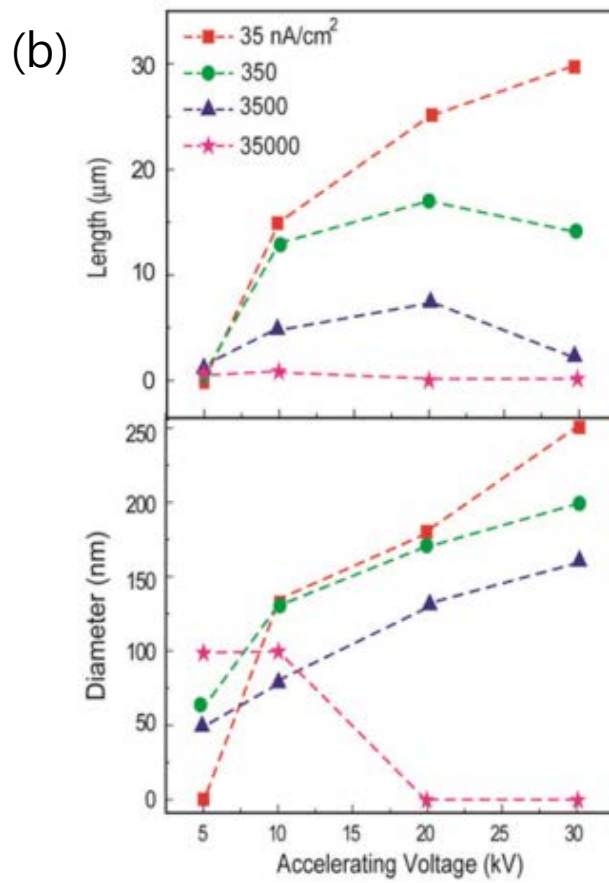
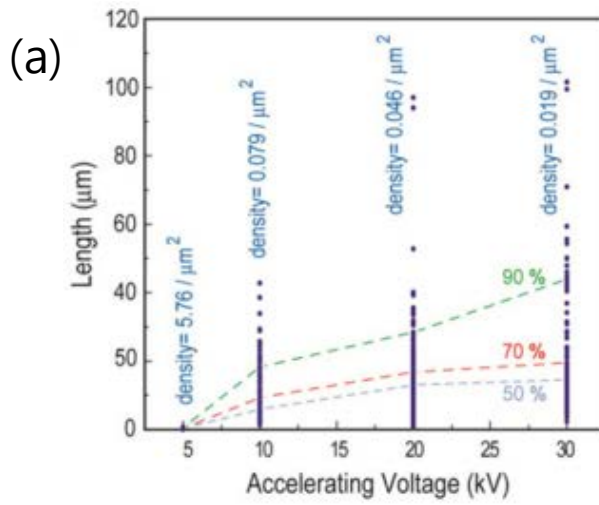


Figure 3.17 TEM analysis of the nanowire (a) Bright field image with growth direction. Inset shows the diffraction pattern of the indium nanowire along the [110] zone axis, (b) EDS spectrum of nanowire



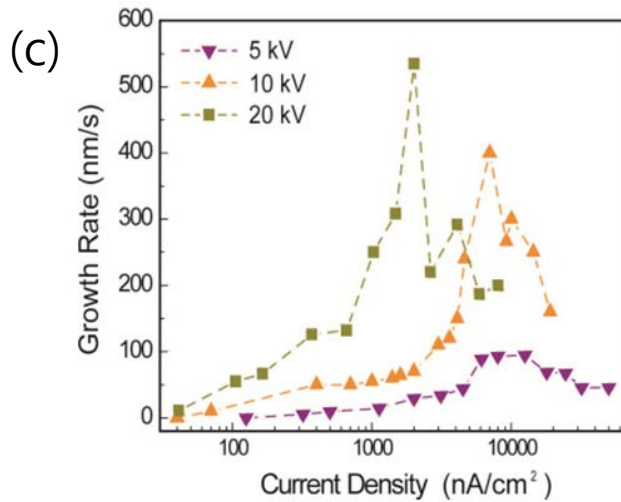


Figure 3.18 Dependence of the nanowires dimensions and growth rate on the ion beam parameters. (a) Length distribution of the nanowires synthesized at current density of 15 nA/cm<sup>2</sup> and different ion beam accelerating voltages. The lines denoted by 50%, 70% and 90% indicate the 50<sup>th</sup>, 70<sup>th</sup> and 90<sup>th</sup> percentile of the collected data for nanowires length at each accelerating voltage. (b) Dependence of nanowires average length and diameter on the ion beam parameters. (C) Dependence of the average growth rate of nanowires on the ion beam current density measured for three distinct voltages of 5, 10, 20 kV

### 3.6.4 Growth mechanism

#### - Origin of indium source: phase decomposition

To confirm the origin of indium source, 1MV high-voltage TEM and EELS analysis was performed for the investigation of chemical component on nanowires themselves and In-rich InGaN substrate before and after FIB irradiation as shown Figure 3.19, revealing the migration of indium toward surface after ion beam irradiation and resulting the growth of indium nanowire. Before ion beam irradiation, the InGaN layer was filled with over 80 at. % of indium content (red in EELS map) as indicated in Figure 3.19 (a). However, the nanowire region after the ion irradiation was detected in red, indicating indium, and InGaN layer was contained almost no indium left inside the layer.

Lian et al. reported about the ion irradiation induced phase decomposition of  $\text{Cd}_2\text{Nb}_2\text{O}_7$ <sup>38</sup>, and Lugstein et al. also reported that formation of Ga dots caused by the FIB induced phase decomposition of GaAs<sup>39</sup>. Similarly, as Ga<sup>+</sup> FIB was irradiated on the In-rich InGaN layer, the phase decomposition might occur inside the InGaN layer. The component of weaker bonding strength, InN, was promptly decomposed by Ga<sup>+</sup> ion, and the In source originated from the decomposed indium inside the InGaN layer was supplied enough for indium nanowire growth without additional indium source.

The effect of FIB irradiation on the morphological change of InGaN template was examined. During the Ga<sup>+</sup> ion beam irradiation, its cross-section was

monitored in-situ by FIB/SEM dual beam system, as shown in Figure 3.20. To exclude the effect of ion beam irradiation of the cross-section area, FIB was intentionally tilted and irradiated on the surface only. During the ion beam irradiation, the morphology of InGaN cross-section was gradually changed. Decomposed indium caused by FB irradiation was filling the existing pores of InGaN layer, exuding, and finally forming indium nanodots on its cross-section. On the surface of InGaN layer, indium nanowires grew up and the growth was confirmed to be the bottom-up one. It was reported that the melting temperature of indium could be considerably reduced by the reduction in size<sup>40</sup>. Nano-size indium clusters formed by ion irradiation might be liquid-like during the ion beam irradiation and become mobile to fill the pores.

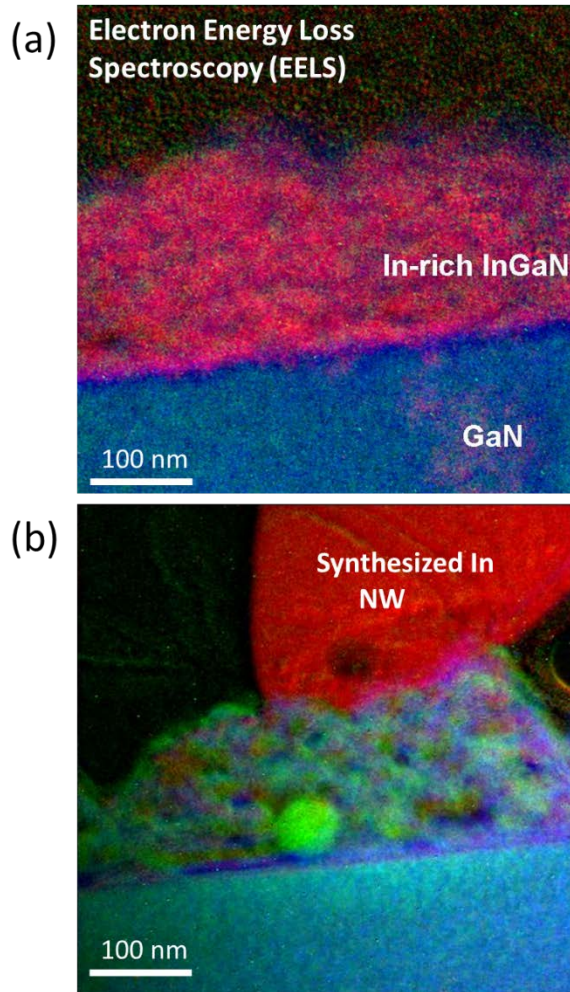


Figure 3.19 EELS composition map using HVEM (a) before and (b) after  $\text{Ga}^+$  ion irradiation on InGaN. Indium (red), Gallium (red), Nitrogen (green)

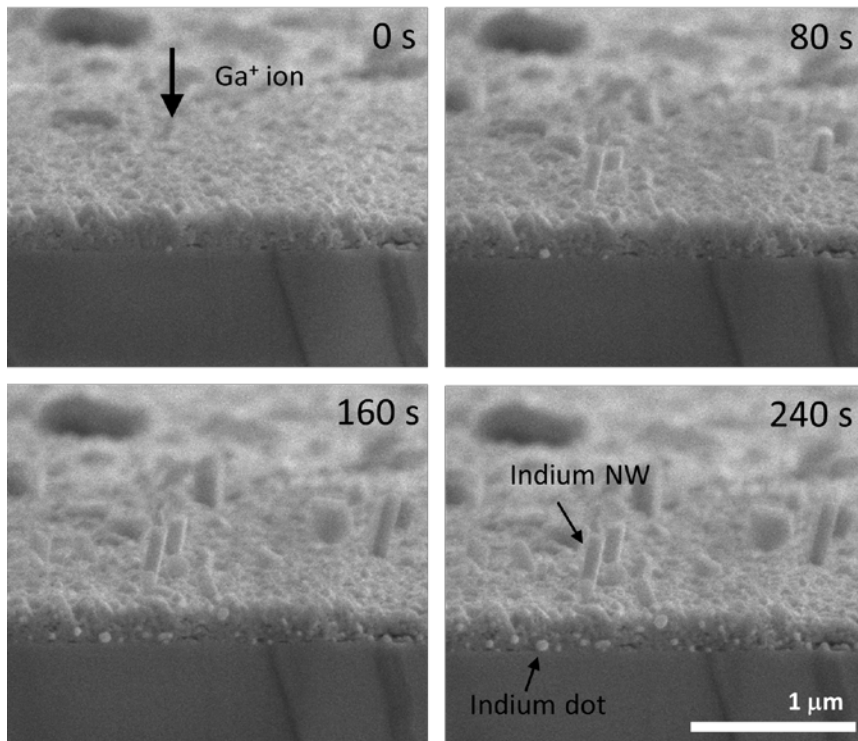


Figure 3.20 In-situ monitoring of cross-section view of InGaN during Ga<sup>+</sup> ion irradiation on the surface

- Ion beam induced stress and atomic migration

As we mentioned in the chapter 3.4, ion irradiation (or implantation) on crystalline surface can induce high levels of stress, which is generally known as compressive stress. The biaxial elastic stress  $\sigma_{11} = \sigma_{22} = \sigma$  at the depth  $x_3$  in the ion irradiated region can be expressed as follows<sup>41</sup>:

$$\sigma_e(x_3) = - \frac{E}{1-\nu} \varepsilon(x_3) \quad (3.4)$$

Where  $E$  is Young's modulus,  $\nu$  is Poisson's ratio and  $\varepsilon$  is the intrinsic strain tensor. This compressive stresses are usually attributed to the extensive defect production by ion collision cascade. Associated with each of these defect is an excess (relaxation) volume, thus creating internal stress. When we denote the atomic volume of the virgin crystalline material  $\Omega$  and the atomic volume related to the defect  $\Omega_r$ <sup>42</sup>, where the subscript  $r$  denotes different types defects. Vacancies ( $r = v$ ) act in the compressive way ( $\Omega_v - \Omega = \Delta\Omega_v < 0$ ) and, as a result, the local stress in the region of a vacancy is tensile. Interstitials ( $r=i$ ) and implanted ions ( $r = ion$ ) are expanding the lattice ( $\Omega_i - \Omega = \Delta\Omega_i > 0$ ,  $\Omega_{ion} - \Omega = \Delta\Omega_{ion} > 0$ ) and the local stress appearing due to interstitials and implanted ions is compressive. We assume that the tensor of the intrinsic strain depends on the density of defects  $n_r$  and on the atomic volume of the defect  $\Omega_r$ . Taking into account all the components of the strain tensor, one can write<sup>41</sup>

$$\varepsilon = \frac{1}{3} \left( \frac{\Delta\Omega_v}{\Omega} \frac{n_v(x_3)}{n_0} + \frac{\Delta\Omega_i}{\Omega} \frac{n_i(x_3)}{n_0} + \frac{\Delta\Omega_{ion}}{\Omega} \frac{n_{ion}(x_3)}{n_0} \right) \quad (3.5)$$

Where  $n_0$  is the atomic density. The density of the Frenkel defects ( $n_v = n_i = n$ ) depends on the ion dose.

Because  $\Delta\Omega_v > |\Delta\Omega_i|$  (typical values of the changes of atomic volumes are  $\Delta\Omega_v = -(0.3-0.6) \Omega$  and  $\Delta\Omega_i = (1.7-2.2) \Omega$ )<sup>43</sup> from equations of (3.4) and (3.5), it can be seen that compressive stress dominates in the ion-implanted region.

As a microstructural proof, we calculated the lattice mismatch strain by measuring the d-spacing of InGaN and GaN before and after ion irradiation. Substrate (InGaN/GaN) was grown as a single crystal with growth direction (z) of [001] and lateral direction (x) of [100]. By measuring the (100) plane d-spacing in InGaN and GaN (Figure 3.21), intrinsic stress and stress relaxation by ion irradiation could be obtained. Lattice mismatch strain along [100] direction was calculated as follows

$$\varepsilon_{100} = - \frac{d_{InGaN} - d_{GaN}}{d_{GaN}} \times 100(\%) \quad (3.6)$$

where  $d_{InGaN}$ , and  $d_{GaN}$  are d-spacing within InGaN and GaN along [100] direction. Before ion irradiation, lattice mismatch strain was - 9.3%, which is intrinsic strain by lattice mismatch during the sample synthesis (compressive strain due to larger d-spacing in InGaN than that of GaN). This misfit strain was reduced to - 4.3% after ion irradiation (Figure 3.22). As shown in Figure 3.20, during in-situ monitoring of cross-section view, we can observe the formation and growing indium droplet filling the pores in InGaN during ion irradiation. Since densities of solid and liquid indium<sup>44</sup> are known as  $7.31 \text{ g cm}^{-3}$  and  $7.02$

g cm<sup>-3</sup>, which provide the 4.1% of volume expansion during phase transformation. And this liquid indium was constrained within biaxially compressed InGaN before nanowire growth, thus stress state of indium under ion irradiation became hydrostatic compression due to the presence of liquid indium. Above the certain critical compressive stress, indium nanowires are expected to grow through the porous channel within the InGaN.

Another key factor which is responsible for the nanowire growth is stress-induced migration. The gradient of stress is the driving force for atomic diffusion. Since the atoms diffuse from position with higher compressive stress towards position with lower compressive stress<sup>23,27</sup>. The compressive stress accumulated within the InGaN structure induced indium atoms to diffuse toward the pores. The accumulated indium became liquid like droplet and filled the pores in InGaN. Finally, indium nanowires were grown through the InGaN surface to relax the compressive stress.

### 3.6.5 Site selective growth and patterning

As a final step, we controlled the growth region of individual indium nanowires using the method of maskless patterning built into the FIB system. When the InGaN surface is subject to the cross-shaped FIB irradiation shown in Figure 3.23, single nanowires emerge and grow at the center of the irradiated areas due to FIB overlapping<sup>45</sup>. In this set of experiments, the ion beam was raster-scanned over the cross-shaped area from left to right and from top to

bottom, leading to increased ion concentration at the center of the cross-shaped region. This method enables selection of the site of growth of individual nanowires. In Figure 3.23 (a) the current density and accelerating voltage are  $1.2 \mu\text{A cm}^{-2}$  and 10 kV, which results in indium nanowires with an average diameter and length of 80 nm and 6  $\mu\text{m}$ , respectively. The average growth rate is  $30 \text{ nm s}^{-1}$  in this case. This method of creation of well-defined functional networks of nanowires has a significant potential in a number of scientific fields and technological applications, such as electronics and optoelectronic devices. Owing to their low melting point, site-controlled indium nanowires can be also used for assisting the growth of aligned long nanotubes using vapor–liquid–solid mechanisms. This method can be used for building nanothermometer devices, opening avenues for designing novel temperature-driven switches and sensors. Furthermore, using the maskless patterning method, we have created blocks of  $25 \times 25 \mu\text{m}^2$  nanowire forests (Figure 3.23 (b)). In this case a  $\text{Ga}^+$  ion beam with accelerating voltage and current density of 5 kV and  $350 \text{ nA cm}^{-2}$ , respectively, was raster-scanned over areas of the substrate. The fabricated nanowires have average length and diameter of 2–3 microns and 50 nm, respectively.

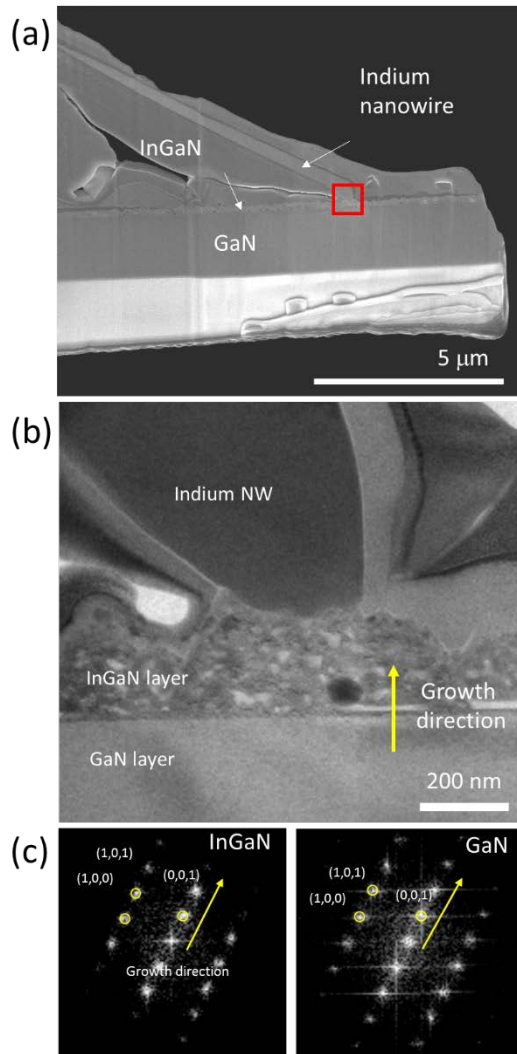


Figure 3.21 TEM analysis of InGaN and GaN substrate to calculate the misfit strain by measuring the d-spacing (a,b) Low magnification of sample, (c) diffraction patterns of InGaN and GaN

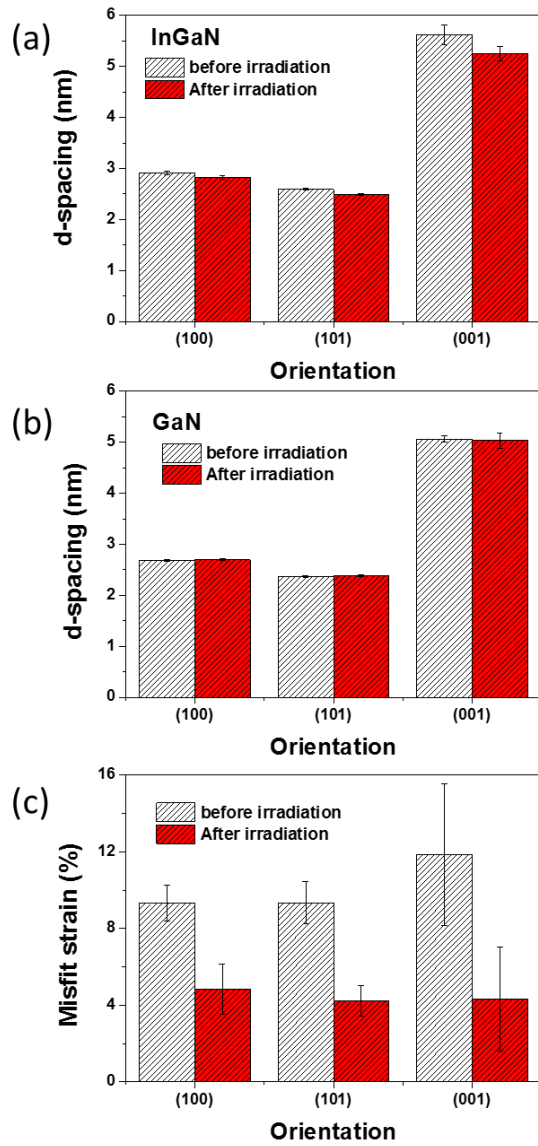


Figure 3.22 Measured d-spacings of (a) InGaN (b) GaN and (c) calculated misfit strain dependent on the orientation

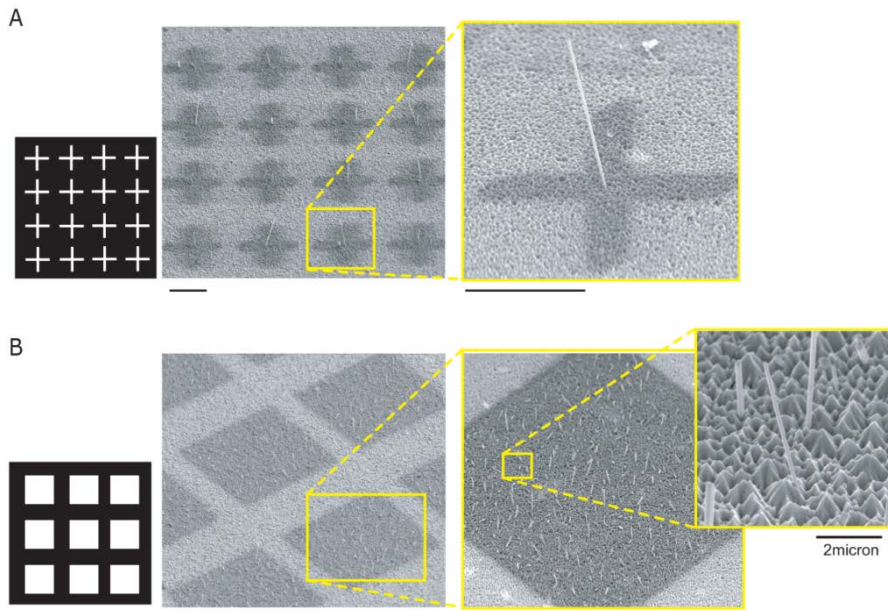


Figure 3.23. Functional networks of nanowires. (a) SEM image of a network of single indium nanowires created on selected locations using a maskless patterning. (b) Nanowire forests of  $25 \times 25 \mu\text{m}^2$  size. In both experiments, the current density and accelerating voltage of the ion beam were  $1.2 \mu\text{A cm}^{-2}$  and 10 kV for (a) and  $350 \text{ nA cm}^{-2}$  and 5 kV for (b). Scale bar =  $5 \mu\text{m}$ , unless denoted otherwise

### **3.7 Conclusion**

The growth of indium nanowire by ion beam induced stress was systematically investigated. To development and optimization of ion beam induced indium nanowire growth, the effect of major growth parameters such as acceleration voltage, current density was investigated for the controlled growth. Indium source for nanowire growth was originated from the ion beam induced InGaN phase decomposition. And compressive stress generated by ion beam irradiation and stress migration of indium atoms was the driving force for indium nanowire growth. Nanowires could be synthesized on desired areas of the substrate by simply controlling the regions exposed to the ion beam using maskless patterning. Extension of the developed technique allows for fabrication of variety of functional networks of indium nanowires, with control over individual nanowires sites and dimensions.

### 3.8 References

1. Y. Xia, P. Yang, Y. Sun, Y. Wu, B. Mayer, B. Gates, Y. Lin, F. Kim, H. Yan, *Adv. Mater.* **15**, 353 (2003).
2. X. Duan, C.M. Lieber, *Adv. Mater.* **12**, 298 (2000).
3. X. Duan, C.M. Lieber, *J. Am. Chem. Soc.* **122**, 188 (2000).
4. T.M. Whitney, J.S. Jiang, P.C. Searson, C.L. Chien, *Science* **261**, 1316 (1993).
5. R.S. Wagner, W.C. Ellis, *Appl. Phys. Lett.* **4**, 89, (1964).
6. Y. Wu, P. Yang, *J. Am. Chem. Soc.* **123**, 3165 (2001).
7. Y. Wu, P. Yang, *Chem. Mater.* **12**, 605 (2000).
8. C.C. Chen, C.C. Yeh, *Adv. Mater.* **12**, 738 (2000).
9. M.H. Huang, Y. Wu, H. Feick, N. Tran, E. Webber, P. Yang, *Adv. Mater.* **13**, 113 (2001).
10. H.J. Fan, F. Bertram, A. Dadgar, J.j Christen, A. Krost, M. Zacharias, *Nanotechnology* **15**, 1401 (2004).
11. S.M. Zhou, Y.S. Feng, L.D. Zhang, *Chem. Phys. Lett.* **369**, 610 (2003).
12. S.T. Lee, N. Wang, Y.F. Zhang, Y.H. Tang, *MRS Bulletin* **20**, 36 (1999).
13. M. Zheng, L. Zhang, X. Zhang, J. Zhang, G. Li, *Chem. Phys. Lett.* **334**, 298 (2001)
14. H. Ringsdorf, B. Schlarb, J. Venzmer, *Angew. Chem. Int. Ed. Engl.* **27**, 113 (1988).
15. C.N.R. Rao, A. Govindaraj, F.L. Deepak, N.A. Gunari, M.Nath, *Appl. Phys. Lett.* **78**, 1853 (2001).
16. Y. Yin, Y. Lu, Y. Sun. Y. Xia, *Nano Lett.* **2**, 427 (2002).
17. H.L. Cobb, *Mon. Rev. Am. Electroplaters Soc.* **33**, 28 (1946).
18. G.T. Galyon, SMTA International Conference, Chicago (2004).
19. C. Herring, J.K. Galt, *Phys. Rev.* **85**, 1060 (1952).

20. R.M. Fisher, L.S. Darken, K.G. Carroll, *Acta Metall.* **2**, 368 (1954).
21. M. Chen, Y. Yue, Y. Ju, *J. Appl. Phys.* **111**, 104305 (2012).
22. Y.-T. Cheng, A.M. Weiner, C.A. Wong, M.P. Balogh, *Appl. Phys. Lett.* **81**, 3248 (2002)
23. N. Settsu, M. Saka, F. Yamaya, *Strain* **44**, 201 (2008).
24. K. Zeng, K.N. Tu, *Mater. Sci. Eng. R* **38**, 55 (2002).
25. K.N. Tu, *Acta Metall.* **21**, 347 (1973).
26. W. Shim, J. Ham, K.-I. Lee, W.Y. Jeung, M. Johnson, W. Lee, *Nano Lett.* **9**, 18 (2009).
27. M. Saka, M. Yasuda, H. Tohmyoh, N. Settsu, *Proc. 2<sup>nd</sup> Electronics system-integration Technology Conference IEEE* (2008).
28. P.J. Burnett, T.E. Page, *J. Mater. Sci.* **20**, 4624 (1985).
29. G.B. Krefft, E.P. EerNisse, *J. Appl. Phys.* **49**, 2725 (1978).
30. G. Carter, W.A. Grant, *Ion Implantation of Semiconductors* (Edward Arnold, London), 42, (1976).
31. P.J. Burnett, T.F. Page, *J. Mater. Sci.* **19**, 845 (1984).
32. J.M. Williams, C.J. Mchargue, B.R. Appleton, *Nucl. Inst. Meth.* **209-210**, 317 (1983).
33. H.J. Kim, Y. Shin, S.-Y. Kwon, H.J. Kim, S. Choi, S.H. Hong, C.S. Kim, J.-W. Yoon, H. Cheong, E. Yoon, *J. Cryst. Growth* **310**, 3004 (2008).
34. A.A. Tseng, *Small* **10**, 924 (2005)
35. L. Frey, C. Lehrer, H. Ryssel, *Appl. Phys. A-Mater. Sci. Process.* **76**, 10107 (2003)
36. C.Y. Nam, J.Y. Kim, J.E. Fisher, *Appl. Phys. Lett.* **86**, 193112 (2005).
37. K. Soulantica, A. Maisonnat, F. Senocq, M.-C. Fromen, M.-J. Casanove, B. Chaudret, *Angew. Chem. Int. Ed.* **40**, 2984 (2001).
38. L. Lian, W. Zhou, Q.M. Wei, L.M. Wang, L.A. Boatner, R.C. Ewing, *Appl. Phys. Lett.* **88**, 093112 (2006).

39. A. Lugstein, B. Basnar, E. Bertagnolli, *Nucl. Instrum. Methods Phys. Res. Sect. B* **217**, 402 (2004).
40. M. Zhang, M.Y. Efremov, F. Schiettekatte, E.A. Olson, A.T. Kwan, S.L. Lai, T. Wisleder, J.E. Greene, L.H. Allen, *Phys. Rev. B.* **62**, 10548 (2000).
41. S. Tamulevicius, I. Pozela, J. Jankauskas, *J. Phys. D: Appl. Phys.* **31**, 2991 (1998).
42. Y.V. Trushin, *Techn. Phys.* **39**, 564 (1994).
43. P. Ehrhart, *Interactions of Atomic Defects in Metals and Alloys*, 25, chap. 2, Springer, Berlin (1991).
44. D.D. Williams, R.R. Miller, *J. Am. Chem. Soc.* **72**, 3821 (1950).
45. R. Buckmaster, T. Hanada, Y. Kawazoe, M. Cho, T. Yao, N. Urushihara, A. Yamamoto, *Nano Lett.* **5**, 771 (2005).

## **Chapter 4. Stress induced piezoresistive effect in $\text{Ge}_2\text{Sb}_2\text{Te}_5$ phase change nanowire**

### **4.1 Piezoresistive effect in semiconductor**

#### 4.1.1. Historical overview

Piezoresistive sensors are among the first Micro-Electro-Mechanical-Systems (MEMS) devices and comprise a substantial market share of MEMS sensors in the market today<sup>1</sup>. Silicon piezoresistance has been widely used for various sensors including pressure sensors, accelerometers, cantilever force sensors, inertial sensors, and strain gauges.

William Thomson (Lord Kelvin) first reported on the change in resistance with elongation in iron and copper in 1856<sup>2</sup>. Kelvin reported that parallel lengths of copper and iron wires were stretched with a weight and the difference in their resistance change was measured with a modified Wheatstone bridge. Since the elongation was the same for both wires, the effect observed depends truly on variations in their conductivities. Motivated by Lord Kelvin's work, Tomlinson confirmed this strain-induced change in conductivity and made measurements of temperature and direction dependent elasticity and conductivity of metals under varied orientations of mechanical loads and electrical currents (Figure. 4.1)<sup>3,4</sup>.

The steady-state displacement measurement techniques of Thomson and

Tomlinson were replicated, refined and applied to other polycrystalline and amorphous conductors by several researchers<sup>5,6</sup>. In 1932, Allen presented the first measurements of direction dependent conductivity with strain in single crystals of bismuth, antimony, cadmium, and zinc<sup>7-9</sup>. Based on this work, Bridgman developed a tensor formulation for the general case of homogeneous mechanical stress on the electrical resistance of single crystals<sup>5</sup>. In 1935, Cookson first applied the term piezoresistance to the change in conductivity with stress, as distinct from the total fractional change of resistance<sup>10</sup>. The now standard notation for piezoresistivity was adapted from analogous work on piezoelectricity<sup>11</sup>. Voigt formalized tensor notation for stress and strain in crystals and formulated tensor expressions for generalized Hooke's Law and piezoelectricity<sup>12</sup>. In 1950, Bardeen and Shockley predicted relatively large conductivity changes with deformation in single crystal semiconductors<sup>13</sup>. In his paper on semiconductor piezoresistance, C. S. Smith reported the first measurements of the exceptionally large piezoresistive shear coefficient in silicon and germanium<sup>14</sup>. Silicon piezoresistive devices evolved from bonded single strain gauges to sensing devices with integrated piezoresistive regions. In their 1961 paper, Pfann and Thurston proposed the integration of diffused piezoresistive elements with a silicon force collecting element<sup>15</sup>. The first such integrated device, a diffused piezoresistive pressure sensing diaphragm was realized by Tufte et al. in 1962<sup>16</sup>.

Piezoresistive sensors were the first commercial devices requiring three-

dimensional micromachining of silicon. Consequently, this technology was a singularly important precursor to the MEMS technology that emerged in the 1980's. In 1982, Petersen's seminal paper "Silicon as a Mechanical Material" reviewed several micromachined silicon transducers, including piezoresistive devices, and the fabrication processes and techniques used to create them<sup>17</sup>. Petersen's paper helped drive the growth in innovation and design of micromachined silicon devices over the subsequent years.

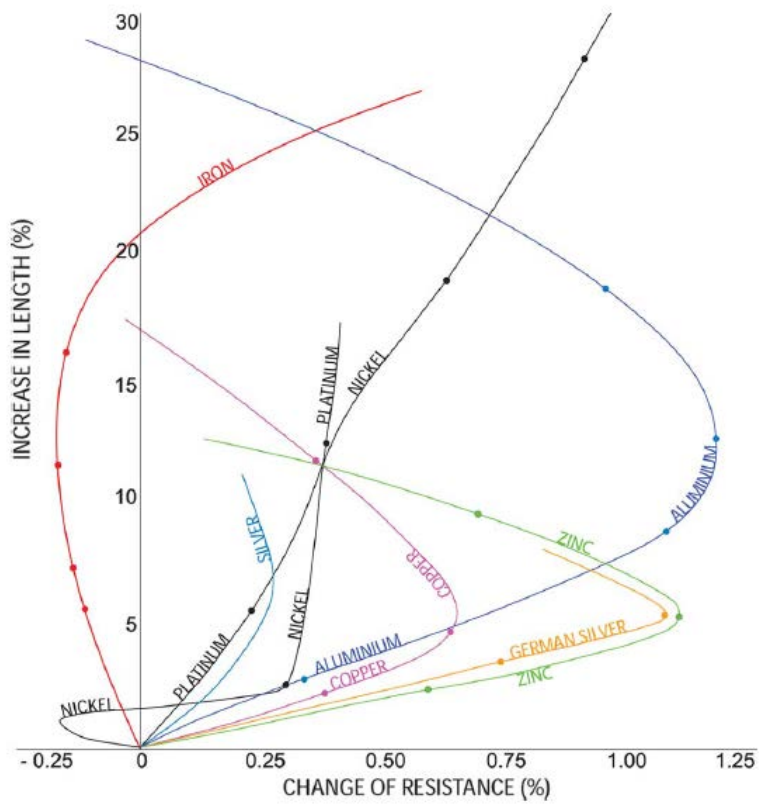


Figure 4.1 The alteration of specific resistance produced in different metals<sup>4</sup>

#### 4.1.2. Piezoresistivity fundamentals

##### - Piezoresistivity

Piezoresistivity is one of the most often used transducer effects, in particular for electromechanical sensors made out of silicon. Typical applications are pressure sensors, accelerometers, resonant micro structures used e.g. for chemical sensing<sup>18</sup> and for force sensors for atomic force microscopy<sup>19</sup>. The reason for the common use of the piezoresistive effect is its simplicity.

The electrical resistance ( $R$ ) of a homogeneous structure is a function of its dimensions and resistivity ( $\rho$ ),

$$R = \frac{\rho l}{A} \quad (4.1)$$

Here,  $l$  is length, and  $A$  is the cross sectional area the current is flowing. The change in resistance due to applied stress is a function of geometry and resistivity changes. The cross-sectional area of a bulk material reduces in proportional to the longitudinal strain by its Poisson's ratio,  $\nu$ , which for most metals ranges from 0.25 to 0.35. For anisotropic silicon, the effective directional Poisson's ratio ranges from 0.06 to 0.36<sup>20</sup>. The isotropic lower and upper limit for are  $-1/0$  and  $0.5$ <sup>21</sup>.

The gauge factor (GF) of a strain gauge is defined as

$$GF = \frac{\Delta R/R}{\varepsilon} \quad (4.2)$$

where  $\varepsilon$  is strain and  $\Delta R/R$  is fractional resistance change with strain. The change in resistance is due to both the geometric effects  $(1+2\nu)$  and the fractional change in resistivity  $(\Delta\rho/\rho)$  of the material with strain<sup>22</sup>,

$$\frac{\Delta R}{R} = (1 + 2\nu)\varepsilon + \frac{\Delta\rho}{\rho} \quad (4.3)$$

Geometric effects alone provide a GF of approximately 1.4 to 2.0, and the change in resistivity,  $\Delta\rho/\rho$ , for a metal is small - on the order of 0.3. However, for silicon and germanium in certain directions,  $\Delta\rho/\rho$  is 50–100 times larger than the geometric term. For a semiconductor, elasticity and piezoresistivity are direction-dependent under specified directions of loads (stress, strain) and fields (potentials, currents).

#### **- Mathematical description of the piezoresistive effect**

The name ‘piezo’ comes from the Greek word ‘piezin’ which means squeezing or pressing tightly. Combined with resistivity it describes the dependence of electrical resistivity  $\rho$  on a mechanical strain  $\varepsilon$  or stress  $\sigma$ . The formula is usually given in terms of stress  $\sigma$  applied to the resistor. For isotropic materials in the linear elastic region, the stress-strain relationship is given by Hooke’s law

$$\sigma_x = E \varepsilon_x \quad (4.4)$$

with the Young's modulus  $E$ . The strain  $\varepsilon$  is defined as the relative change in length ( $\varepsilon = \Delta l/l$ ).

The linear piezoresistive effect in one direction in an isotropic material is defined by

$$\frac{\Delta\rho_x}{\rho_x} = \pi_x \sigma_x \quad (4.5)$$

The piezoresistive coefficient  $\pi$  has units of  $\text{Pa}^{-1}$ . To describe the piezoresistive effect for isotropic materials in all three dimensions including normal and shear stress components, the coefficient  $\pi$  must be defined as a tensor and thus equation (4.5) becomes

$$\frac{\Delta\rho_i}{\rho_o} = \sum_j \pi_{ij} \sigma_j \quad (4.6)$$

The indexes describe the geometrical orientation of the effect. The stress component,  $j$  defines the three normal stresses and the three shear stresses. In the contractive notation, six components are used. To describe the directionality of the resistivity, the same relationship between voltage and current can be applied as between stress and strain. Therefore, the index  $i$  has six components as well. In the contractive notation, the general piezoresistive coefficient  $\pi$  becomes a second rank tensor with  $6 \times 6$  elements.

$$\pi_{ij} = \begin{bmatrix} \pi_{11} & \pi_{12} & \pi_{13} & \pi_{14} & \pi_{15} & \pi_{16} \\ \pi_{12} & \pi_{22} & \pi_{23} & \pi_{24} & \pi_{25} & \pi_{26} \\ \pi_{13} & \pi_{23} & \pi_{33} & \pi_{34} & \pi_{35} & \pi_{36} \\ \pi_{14} & \pi_{24} & \pi_{34} & \pi_{44} & \pi_{45} & \pi_{46} \\ \pi_{15} & \pi_{25} & \pi_{35} & \pi_{45} & \pi_{55} & \pi_{56} \\ \pi_{16} & \pi_{26} & \pi_{36} & \pi_{46} & \pi_{56} & \pi_{66} \end{bmatrix} \quad (4.7)$$

For anisotropic materials, the number of independent components can often be reduced due to symmetry effects. For example, in single-crystal silicon there are only 12 non-zero coefficients instead of 36. Due to the cubic crystal symmetry, only three of them are independent  $\pi_{11}$ ,  $\pi_{12}$  and  $\pi_{44}$ . For isotropic material, the number of independent components can be reduced to only two.

For most applications, only two arrangements of load and resistance change are of interest, resulting in the longitudinal and the transverse piezoresistive effect. The first one describes the change of the resistance if the force is applied in the same geometrical direction as the E-field and thus the current is flowing, while the second one describes the change to a load applied perpendicular to the E-field and the current direction. Both structures can be easily build and used to characterize the different piezoresistive effects. The effective values for the longitudinal piezoresistive coefficient ( $\pi_l$ ) and the transverse piezoresistive coefficient ( $\pi_t$ ) can be calculated from the piezoresistive coefficient tensor  $\pi_{ij}$ .

For anisotropic materials such as single-crystal silicon,  $(\pi_l)$  and  $(\pi_t)$  depend on the orientation of the resistor with respect to the crystal axis and the values can be computed using coordinate transformation techniques. For an unknown, isotropic material, the values of  $\pi_l$  and  $\pi_t$  can be identified directly by using appropriate test structures. A description of the linear piezoresistive effect can then be given by superposition of the longitudinal and the transverse piezoresistive effect:

$$\frac{\Delta\rho}{\rho} = \pi_l\sigma_l + \pi_t\sigma_t \approx \pi_l\sigma_l \quad (4.8)$$

with the stress components  $\sigma_l$  in longitudinal and  $\sigma_t$  in transverse direction. The  $\sigma_t$  can be neglected in the nanowire under uniaxial stress application, so this equation can be reduced to as shown in equation (4.8).

### **- Piezoresistivity Theory**

The theories of semiconductor piezoresistance are grounded in one-dimensional descriptions of electron and hole transport in crystalline structures under strain (potentially extended to three dimensions and to include crystal defects, electric potentials, and temperature effects). Unlike metals, whose piezoresistivity are based on geometric changes, the piezoresistive effect of silicon are based on mobility changes of carriers. Volume changes affect the energy gap between the valence and conduction and, the number of carriers and thus the resistivity changes. The solid state physics theory postulates that the

energy of electrons in the crystal lattices is not continuous but is separated as energy bands due to interaction between electrons and lattice atoms, namely conduction and valence bands.

In the conduction band, there is a minimum energy necessary for electrons to exist. This minimum energy is called band edge point (BEP), as shown in Figure 4.2. In the case of silicon, the peak of valence band and valley of conduction band are not aligned at the same wave-number  $k$ . This refers to indirect band gap semiconductor. Instead the valleys of conduction band sit on the six  $\langle 100 \rangle$  equivalent axes. This is called the one band many valley model. At room temperature, there will be electrons getting enough thermal energy to partially fill these valleys. In the absence of stress, these six valleys have the BEP at the same energy level, and electrons fill these valleys equally. But when the stress is introduced into crystal, the lattice structure and the distance between lattice points will also be distorted by stress. As a result, the interaction between the electrons and lattice atoms will also be changed accordingly. This causes the band edge point (BEP) for some valleys to decrease and for some other valleys to increase. Therefore, more electrons would get enough energy to get into some valleys and fewer electrons would get into other valleys.

Figure 4.2 illustrates that as an isotropic stress is applied in  $[100]$  direction, it causes lattice compression in the same direction<sup>14</sup>. Usually this compressive stress would reduce lattice traction in other principal axes and under this situation, the minimum energy of conductive band valley in  $[100]$  direction will

be lowered while the minima on the other axes will be raised. The Fermi levels does not change according to crystal lattice distortion, hence when there is a compressive stress in [100] and results in its BEP to be lower, it causes the redistribution of electrons between the band valleys and more electrons will move in [100] valley from [010] and [001] valleys, which experience traction stress. Consequently, the average mobility of electrons in [100] direction, the direction of compressive will decrease. While, the mobility of electrons in the direction of traction will increase. This phenomenon can be better explained using quantum mechanics. In quantum mechanics, the mass of electrons varies due to the interaction with lattice atoms<sup>24</sup>. When the energy band structure is distorted due to application of stress, the curvature of energy band in k space,  $d^2E/d^2k$ , will also be changed (Figure 4.3). This change therefore, alters the effective mass of carriers and further changes the mobility of carriers.

$$\mu = q\tau/m^* \quad (4.9)$$

$\tau$  is the mean time between collisions of carriers with lattice atoms,  $q$  is the charge of carriers and  $m^*$  is the effective mass. It can be calculated that the electrons moving from [010] and [001] into [100] carry smaller effective mass.

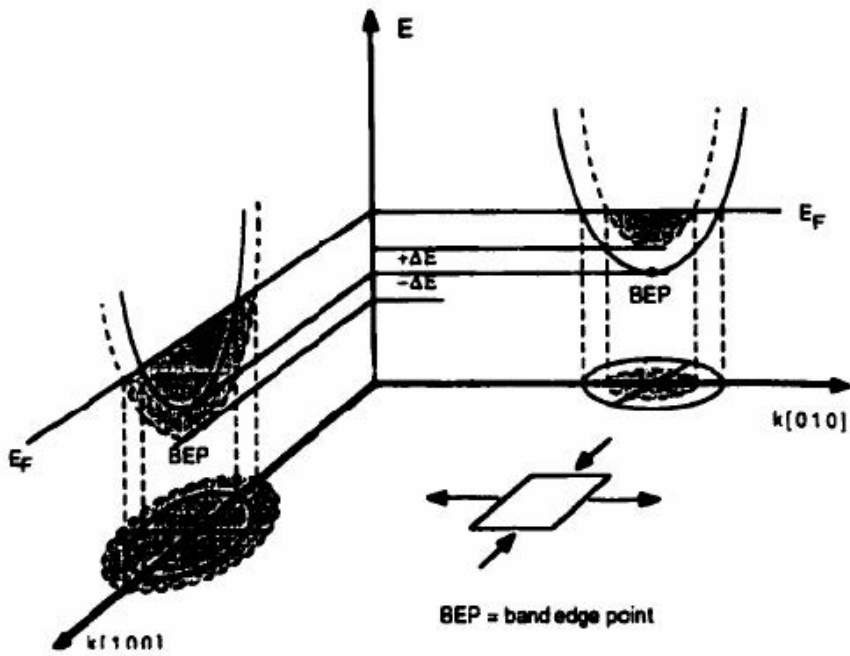


Figure 4.2 Isotropic stress applied on silicon crystal. BEP refers to the minimum energy for electron to exist in conduction band<sup>14</sup>

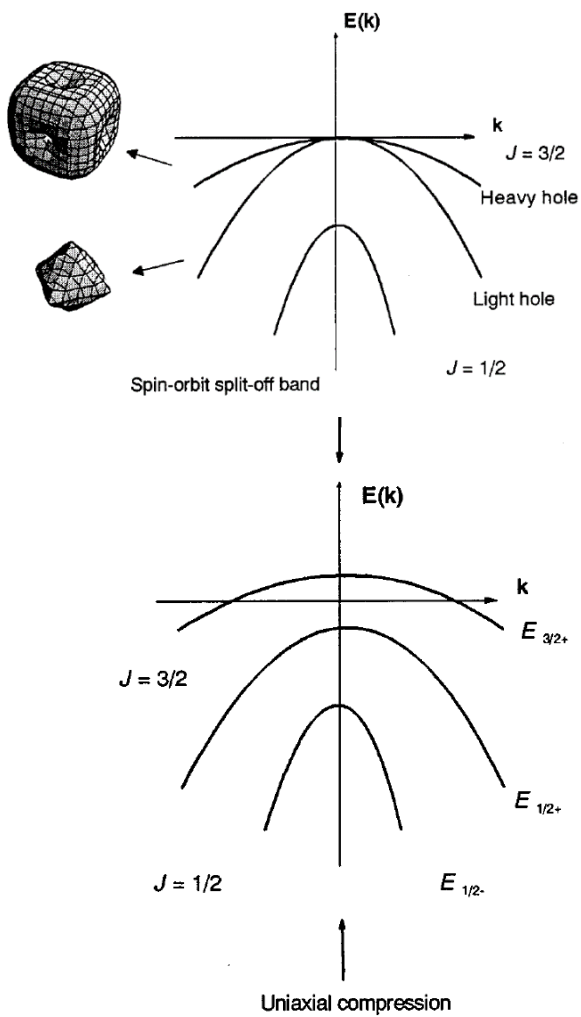


Figure 4.3 Schematic of hole energy of silicon subjected to uniaxial stress<sup>24</sup>

## 4.2. Phase change memory

### 4.2.1 General introduction

Since the first demonstration of resistance switching phenomenon by S. R. Ovshinsky<sup>25</sup>, there has been a great interest and study on the phase change memory. Switching of chalcogenides can be summarized in 2 ways; memory switching and threshold switching<sup>26</sup>. Memory switching involves phase transition from amorphous to crystalline phase; permanent change in material properties results from the memory switching. Threshold switching refers to the abrupt reduction of the electrical resistance which does not involve phase transformation. By using these switching characteristics, non-volatile memory can be constructed which is referred to as phase change memory (PRAM). An operation scheme of PRAM is shown in Figure 4.4. Memory switching requires Joule heating to make a phase transformation. But electrical resistivity of the amorphous phase is larger than crystalline phase. As a result, it requires high voltage to make enough current to flow through amorphous material to induce phase transition by Joule heating. But amorphous chalcogenides make threshold switching at relative low voltage and turns into low resistance state. This allows large current flow at relatively low voltage and enables SET (crystallization) and RESET (amorphization) switching to occur at similar voltages<sup>26</sup>. For RESET of the crystalline device, a short ( $t_{\text{reset}} \sim 50$  ns) and intense ( $I_{\text{reset}} \sim 1$  mA at 50 nm-diameter contact) pulse is applied to induce local

heating at the contact region between  $\text{Ge}_2\text{Sb}_2\text{Te}_5$  and bottom electrode; resultant resistance of the device is determined by high resistive amorphous cap above the bottom electrode and this state is called high resistance state (HRS). For SET of the amorphous device, a relatively long ( $t_{\text{set}} \sim 500$  ns) and intermediate ( $I_{\text{set}} \sim 0.2$  mA at 50 nm-diameter contact) is used to induce crystallization by increasing temperature of the amorphous cap to above crystallization temperature. Major limitation of PRAM operation is caused by the large RESET current.

Though the concept of PRAM appeared in 1960s, early devices suffered from low thermal efficiency because of the large size of the device. Also, materials for PRAM were not optimized and the required properties such as fast crystallization, thermal stability of amorphous phase, and high endurance were not realized<sup>27</sup>. A breakthrough was made by Chen et al.'s report about Ge-Te binary system<sup>28</sup> and N. Yamada et al.'s report on Au-Ge-Sn-Te alloy<sup>29</sup>. Several years later, N. Yamada et al. made a report on the phase transformation properties of GeTe-Sb<sub>2</sub>Te<sub>3</sub> pseudo-binary compound which have been studied most intensively for the application of optical memory and PRAM<sup>30</sup>. Till 2004, single/dual layer blue-ray disk with the capacity of 25/50 GB were commercialized using GeTe-Sb<sub>2</sub>Te<sub>3</sub> compound<sup>26</sup>. These materials are intended to achieve the conflicting properties; for example, high crystallization speed for fast SET and stability of the amorphous phase at room temperature (or somewhat elevated temperature for high-temperature application) for the good

retention of the RESET state. To enhance the performance of PRAM, optimization of the device structure and material characteristics using doping or composition tuning has been tried.

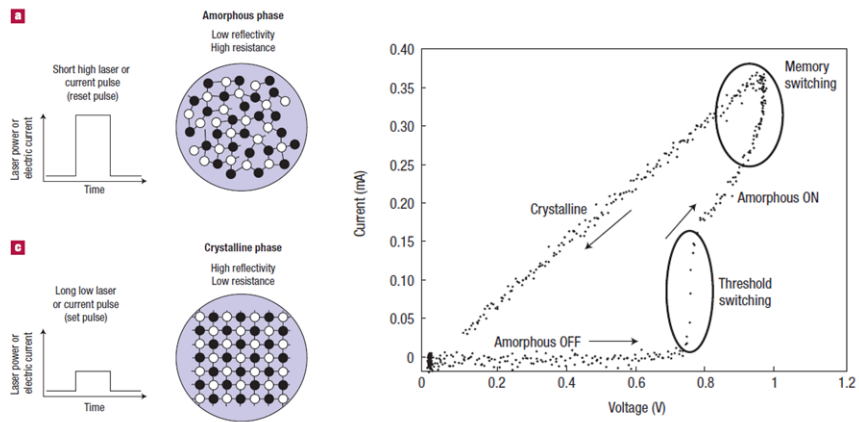


Figure 4.4 Operation principles of PRAM: (L) application of current pulse and resultant phases of phase change material, (R) typical current-voltage curves of PRAM<sup>26</sup>.

#### 4.2.2 Ge<sub>2</sub>Sb<sub>2</sub>Te<sub>5</sub> compound

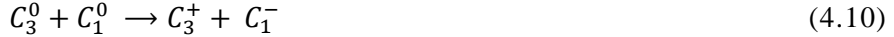
Among the chalcogenide alloys, the ternary compound Ge<sub>2</sub>Sb<sub>2</sub>Te<sub>5</sub> (GST), is the most popular compound employed in the realization of phase change memories. The high conductive GST state is related to a polycrystalline phase with grains organized in a distorted face-centered-cubic (fcc) lattice where a sublattice is constituted by six-fold coordinated tellurium atoms and the other one is randomly occupied by germanium and antimony<sup>30-32</sup>. Due to the stoichiometry of the GST, the germanium and antimony sublattices present one atomic position unoccupied for each basic cell, leading to a 20% of vacant sites<sup>33,34</sup>. Since the crystalline phase shows a long-range structural order, it can be treated as a Bloch semiconductor. Despite a long-range atomic order disappear in the vitreous insulating state, a short-range order still exists. Absorption spectra show the existence of an optical gap of about 0.7 eV with an exponential Urbach tail with a decay of 80 meV, related to localized states, probably the lone pairs<sup>31,35</sup>. Since the transitions induced by programming operations require about 100–200 ns and since more than 10<sup>12</sup> switching operations have been demonstrated on prototype devices, they assumed that atomic positions remain quite the same both in the amorphous and the crystal GST and that phase transition occurs without a significant atomic diffusion. Their work was supported by recent work<sup>32</sup> where a distorted fcc is proposed for c-GST, constituted by rigid building blocks that are bonded to each other in

a crystal lattice. During melting, the interblock bonds break, still maintaining unbroken intrablock bonds, leading to an increase in GST volume. Due to the weakened intrablock bonds, the Ge atoms can flip into the natural tetrahedral coordination, determining an “umbrella flipped” structure of the a-GST.

#### 4.2.3 Electronic state of amorphous $\text{Ge}_2\text{Sb}_2\text{Te}_5$

Due to long-range atomic order, the electronic dynamics in crystalline chalcogenides can be treated according to the Bloch's theorem. On the other hand, amorphous solids are mainly characterized by the absence of a long-range order, with a spatially uneven profile of both the conduction and valence bands. However, investigations on amorphous compounds demonstrated the existence of localized states with variable transport properties<sup>36,37</sup>. It thus became a common practice in the 1960s to describe these materials as in Figure 4.5 (left), where the carrier mobility is a function of the energetic level in the band diagram and “mobility edges” separate fully conductive bands from low mobility states. However, by assuming that the low mobility localized states behave like trapping centers and that more conductive levels resemble delocalized states, it is thus possible to describe the amorphous materials as very defective “semiconductors,” where the “mobility edges” separate the delocalized levels (free bands) from low mobility states, defining a mobility gap larger than the real energy gap (Figure 4.5, right). The theory of localized states in amorphous alloys has been theoretically developed<sup>38-41</sup> in the 1970s.

In those works, they suggest the existence of a short-range chemical order also in the disordered solids and, in particular, it has been suggested that the structural unit of the amorphous chalcogenide is the twofold coordinated chalcogen, usually indicated as  $C_2^0$  (neutral twofold coordinated chalcogen). Different coordinations of the chalcogen atoms thus result in deviant electronic configurations, acting as electronic defects<sup>40</sup>. Moreover, since chalcogen atoms are twofold instead of fourfold coordinated, the two unpaired electrons are supposed to lead to lone pair states<sup>38</sup>, while neutral threefold  $C_3^0$  and onefold  $C_1^0$  coordinated chalcogen lead to a stable charged valence alternation pair (VAP) defect through the reaction<sup>39,41</sup>



Although the exact microscopic structure and the nature of the electronic defects in chalcogenide compounds is still under discussion, the existence of a large concentration of low mobility states is a key element for a comprehensive description of their peculiar electronic properties.

#### 4.2.4 Band structure of $\text{Ge}_2\text{Sb}_2\text{Te}_5$

The physics of both crystalline and amorphous phases has been mapped in a standard semiconductor model by properly implementing band diagrams and transport properties. Absorption measurements on crystalline GST (c-GST) show an optical indirect transition with an energy gap of about 0.5 eV. Since

the conduction is mainly related to free holes with a measured density of about  $10^{19}\sim 10^{20}\text{ cm}^{-3}$ , practically independent from temperature<sup>32,35</sup>, c-GST has been modeled as a quasidegenerate semiconductor. Because no measurement of the density of states has been documented in the literature, they assumed the values as in Table I<sup>37</sup>. Since the density of vacant sites is about 20% of the total atomic density and at thermal equilibrium they are negatively charged, an acceptor level with a density of  $5 \times 10^{20}\text{ cm}^{-3}$  has been introduced in the band diagram, as reported in Figure 4.6 on the left. To take into account the low temperature dependence of conductivity, the trap level has been positioned at 100 meV from the valence band. As a result of the Poisson equation, the Fermi level lies close to the valence band (at about 50 meV), thus causing the p-type quasidegenerate behavior of crystal.

The amorphous phase can also be correctly described with a band diagram. The absorption spectra in the amorphous phase shows the existence of an optical band gap of 0.7 eV<sup>32,35</sup>. A strong exponential activation of the electrical conductivity with temperature has been reported in the literature, suggesting that amorphous GST behaves practically as an intrinsic semiconductor with a Fermi level at about 300 meV from the free hole band<sup>32,35</sup>. Furthermore, absorption spectra also show the existence of an Urbach tail with a decay constant of about 80 meV, thus extending for about 200 meV inside the band gap<sup>35</sup>. To map the Mott and Davis mobility model in their model, they translate the band diagram of Figure 4.6 (left) into the band diagram of Figure 4.5 (right).

The low mobility tail, underlined by the Urbach tail and probably related to the lone pairs is a signature of the existence of a mobility edge in the valence band. As depicted in Figure 4.6, they model this tail with donor states, close to the free hole band, which are neutral at thermal equilibrium with a uniform density of  $10^{20}\sim 10^{21} \text{ cm}^{-3} \text{ eV}^{-1}$  in an energy range of 200 meV from the valence band mobility edge. On the other hand, VAPs have been modeled as couples of donor-acceptor levels with a density of  $10^{18}\sim 10^{20} \text{ cm}^{-3}$ , respectively, close to the conduction and valence bands.

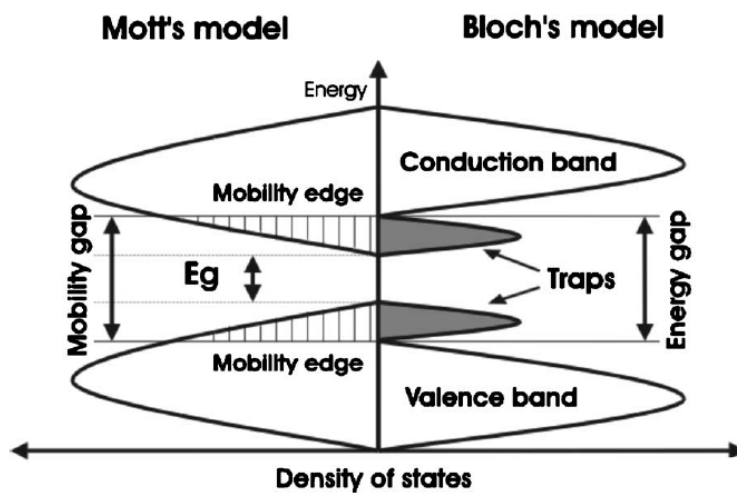


Figure 4.5 Band diagram for amorphous chalcogenide. On the left is Mott's model and on the right is the mapping in a standard semiconductor band diagram

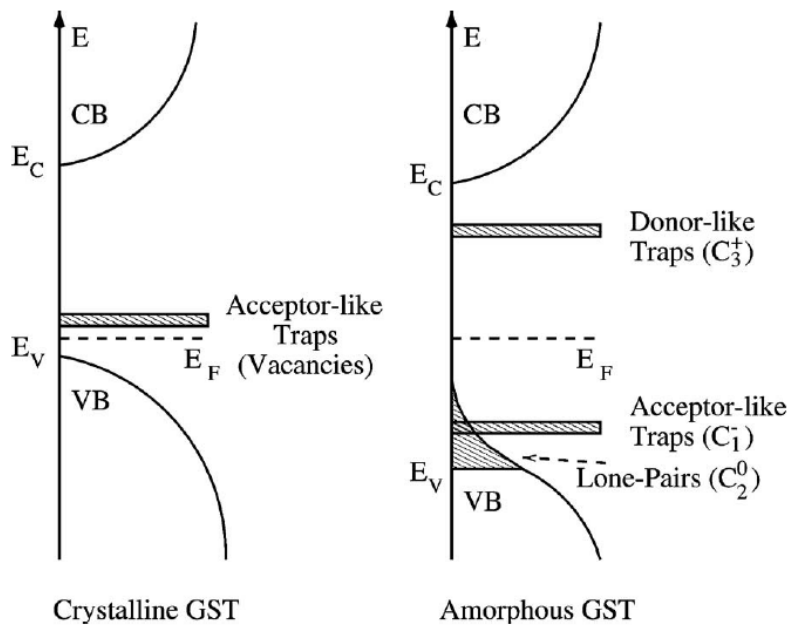


Figure 4.6 Band diagrams for both crystal and amorphous phases implemented in numerical model<sup>31</sup>

Property	GST crystalline	GST amorphous
$\mu_n$ ( $\text{cm}^2 \text{V}^{-1} \text{s}^{-1}$ )	0.1	5
$\mu_p$ ( $\text{cm}^2 \text{V}^{-1} \text{s}^{-1}$ )	23.5	200
$F_C$ ( $\text{V cm}^{-1}$ )	$3.3 \times 10^5$	$3.3 \times 10^5$

Table 4.1 Numerical values of the parameters describing the band structure for crystalline and amorphous GST<sup>37</sup>.

#### 4.2.5. Mechanisms of threshold switching

Threshold switching (OTS) is a fundamental mechanism for PCM devices, allowing a high current density in the device active area of amorphous bits, without developing enormous electrical fields. Despite this fundamental role of OTS effect, the nature of the physical principle responsible for the conductance switching is still controversial. In the past 40 years, several theoretical effects have been devoted to explain this crucial phenomenon<sup>25,42</sup>. Due to the large thermal activation energy of amorphous chalcogenide electrical conductivity<sup>31</sup>, the switching phenomenon has been first ascribed to a thermal breakdown in the amorphous film. By increasing the applied voltage, in fact, the current density increases and as a result of Joule effect, the temperature increases too, thus, locally enhancing the electrical conductivity. When the temperature sufficiently rises, a positive feedback switches on and a huge thermal generation of electrical carriers takes place. The voltage drop on the amorphous film can thus decrease while maintaining a high current density<sup>42</sup>. The balance between the thermal generation, localized along the current pattern, and the lateral carrier diffusion leads to the creation of a hot filament.

Meanwhile, Adler et al. proposed that the OTS effect is not related to a thermal breakdown but in agreement with the original Ovshinsky point of view, he explained the threshold switching as a pure electronic phenomenon<sup>43</sup>. In fact, he supported a purely electronic mechanism primary related to the balance

between a strong Shockley Hall Reed (SHR) recombination through trap levels and a generation mechanism driven by both electric field and carrier densities<sup>44</sup>. In his original model, he considered the chalcogenide material as a doped homogeneous semiconductor resistor with a single trap level closed to one band, and the doping level closed to the opposite band (e.g., an acceptor doping density  $N_a$  close to the valence band and a  $C_c^{tot}$  donor trap concentration near the conduction band). This description represents an attempt to describe the electrical behaviors of chalcogenide glasses with a minimum number of assumptions. The acceptor doping density  $N_a$  is assumed greater than  $C_c^{tot}$  to mimic the p-type low-field conductivity experimentally observed on the majority of chalcogenide compounds<sup>45,46</sup>, while the donor trap concentration near the conduction band  $C_c^{tot}$  can represent the positively charged traps of the VAP pairs. Additional elements (e.g., the negatively charged traps of VAP pairs) can be neglected because their contribution is not necessary to explain the electronic switching effects.

## 4.3 Experimental procedure

### 4.3.1. Synthesis of $\text{Ge}_2\text{Sb}_2\text{Te}_5$ nanowire

$\text{Ge}_2\text{Sb}_2\text{Te}_5$  (GST) nanowires were synthesized using the metal catalyst mediated vapor–liquid–solid (VLS) process in a horizontal vacuum tube furnace<sup>47</sup>. Bulk GeTe and  $\text{Sb}_2\text{Te}_3$  powders (99.99%, Sigma-Aldrich) were used to serve as precursors. The powders were separately located inside a horizontal tube furnace in different temperature zones in order to simultaneously produce vapor-phased reactants. GeTe ( $T_m=724^\circ\text{C}$ ) powder was placed in the middle of the furnace and  $\text{Sb}_2\text{Te}_3$  ( $T_m=617^\circ\text{C}$ ) at the upstream side (5 cm away from the middle of the furnace). The silicon substrate coated with sputtered-Au/Pd film was placed at the downstream side of the furnace (~20 cm away from the middle) as shown in Figure 4.7. The furnace was ramped to  $670^\circ\text{C}$  with a flow of Ar gas (130 sccm) at 100 torr pressure and maintained for 1 hour. After the growth, the furnace was slowly cooled down to room temperature. The as-synthesized nanowires were characterized by scanning electron microscopy (SEM, FEI DB strata 235 FIB) equipped with energy dispersive x-ray spectroscopy (EDS, Oxford INCA) and transmission electron microscopy (TEM)

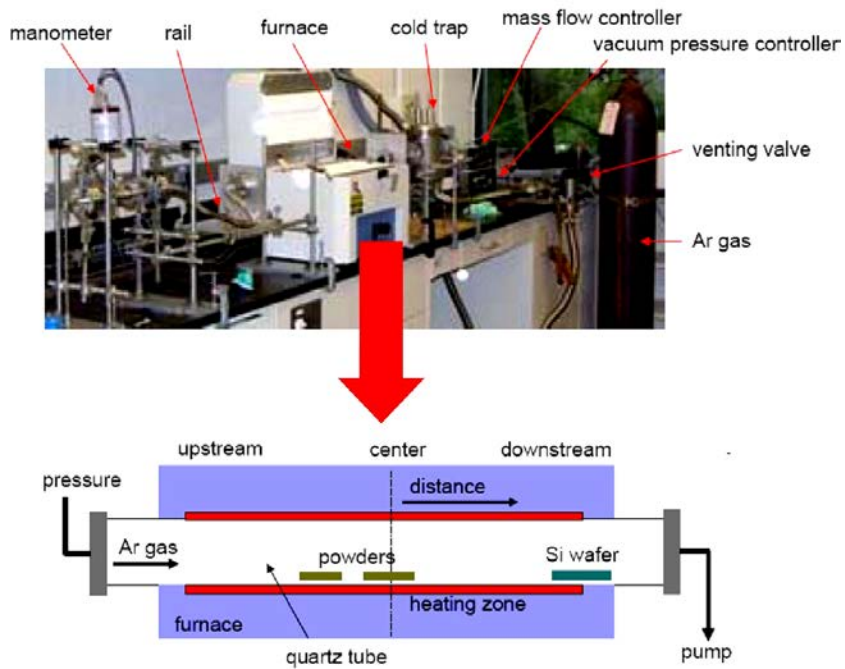


Figure 4.7 CVD system and furnace schematic diagram for nanowire growth.

#### 4.3.2. Device fabrication

As-grown GST nanowire were transferred from grown substrate to polyimide (PI) film (300nm thickness) by contact printing method<sup>48</sup>. A piece of PI film was gently in contact with as grown GST nanowire substrate, and then PI film was gently slid in one direction and detached from the substrate. Even though large numbers of GST nanowires were transferred and aligned with sliding direction on the PI substrate, great care was needed to select the individual nanowire to filter out overlaid nanowires as shown in Figure 4.8. Position of a single GST nanowire on PI substrate was aligned with optical microscope and Au (200 nm)/Ti (or Cr, 50 nm) electrodes were deposited by electron-beam evaporation using a metal shadow mask (Figure 4.9). And then, specimens was uniaxially strained by bending the PI substrate with custom-built strain stage. Schematic illustration for overall process was shown in Figure 4.10.

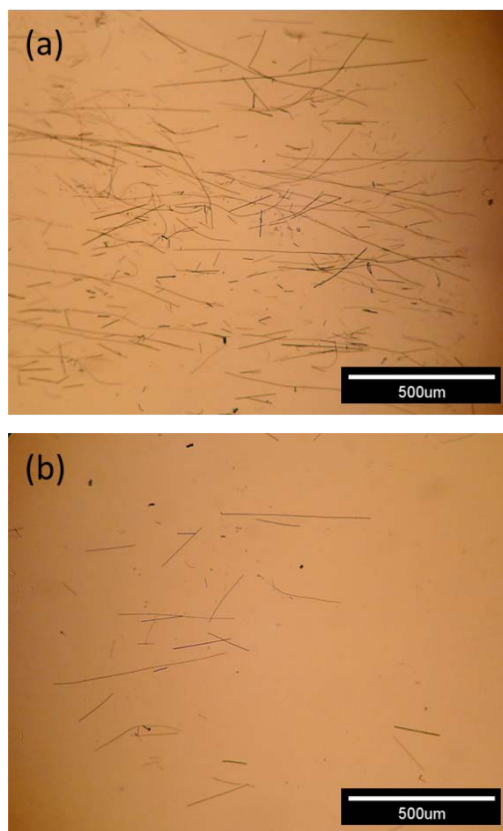


Figure 4.8 Aligned GST nanowires on PI substrate by contact printing method: (a) high density and (b) low density transfer by controlling the contact pressure

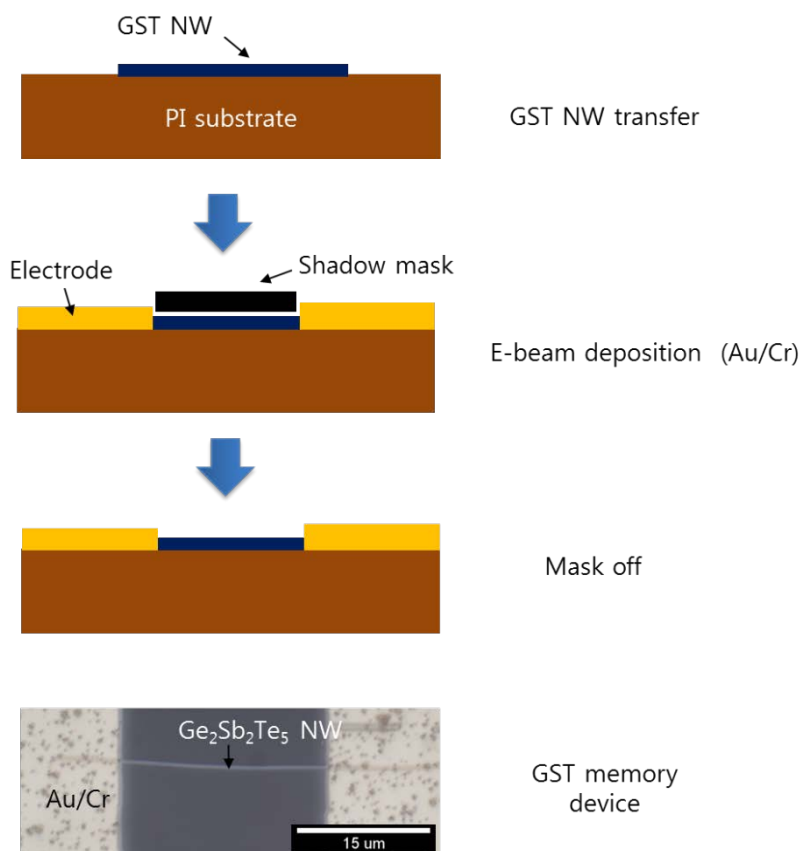


Figure 4.9 Process for device fabrication and optical image of fabricated memory device.

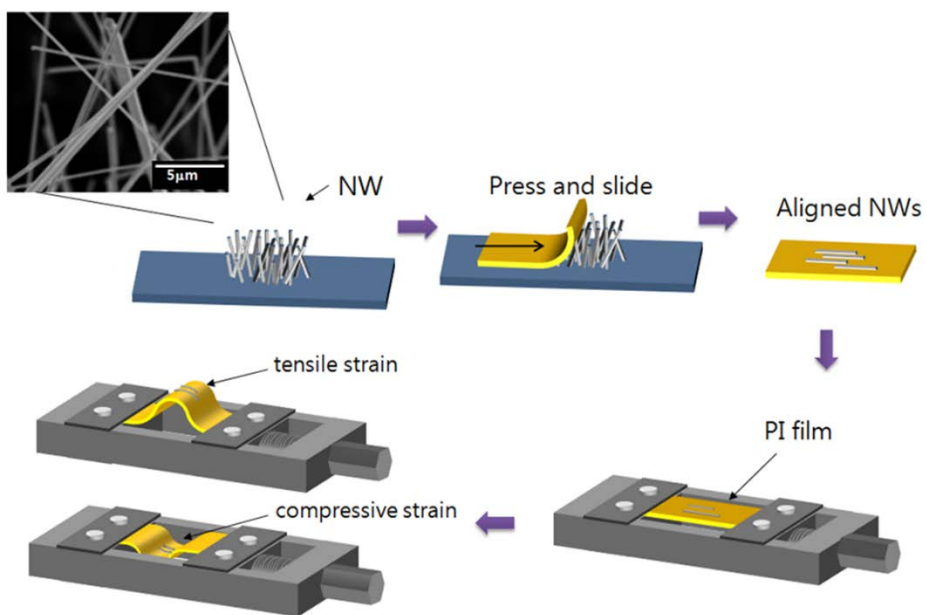


Figure 4.10 Sequence of experiment to exert the external stress/strain to GST nanowire including nanowire transfer, alignment, and straining

#### 4.3.3 Method for mechanical stressing and electrical measurement

The fabricated memory devices (metal electrode-NW-PI substrate) was mounted on custom-built uniaxial strain stage. Reducing the distance between two grip parts by rotating the screw provided the memory devices to be bent upward or downward, which exert the uniaxial tensile or compressive strain (or stress) to the single nanowire device, respectively. All electrical measurement were performed with Keithley 2602 (I-V analyzer), Keithley 2700 (switching box), and Keithley 3401 (pulse-generator)

## 4.4 Results and Discussion

### 4.4.1. Analysis of GST nanowires

The structure and chemical composition of the synthesized GST nanowires were characterized with SEM, EDS, and TEM. Figure 4.11 (a) is a representative SEM image of as synthesized GST nanowires on the surface of Si substrate, showing high-yield nanowire growth. The nanowires have a diameter in the range of 80~400 nm and are up to tens of micrometers in length ( $> 40 \mu\text{m}$ ). Closer structural inspection reveals that majority of nanowires display Au/Pd particles at their ends (Figure 4.11 (b)), indicating that nanowire growth was achieved based on the vapor-liquid-solid (VLS) mechanism<sup>47</sup>. The chemical composition of the synthesized nanowires were identified with EDS as Ge (27.05 at. %), Sb (23.58 at. %), and Te (49.38 at. %) (Figure 4.11 (c)) which is almost close to the ideal atomic ratio of  $\text{Ge}_2\text{Sb}_2\text{Te}_5$ . Further structural characterization of the GST nanowires was performed with TEM analysis. Figure 4.12 (a) shows a low-magnification bright field TEM image of a single GST nanowire with uniform diameter of  $\sim 80$  nm along its entire length. The high resolution TEM image and selected area diffraction (SAD) pattern (Figure 4.12 (b-c)) obtained in the  $[0001]$  zone axis suggest that these nanowires are defect-free single crystals with growth direction of  $[10\bar{1}0]$ , which corresponds to the d-spacing ( $\sim 3.65\text{\AA}$ ) of  $(10\bar{1}0)$  plane for hexagonal GST structure.

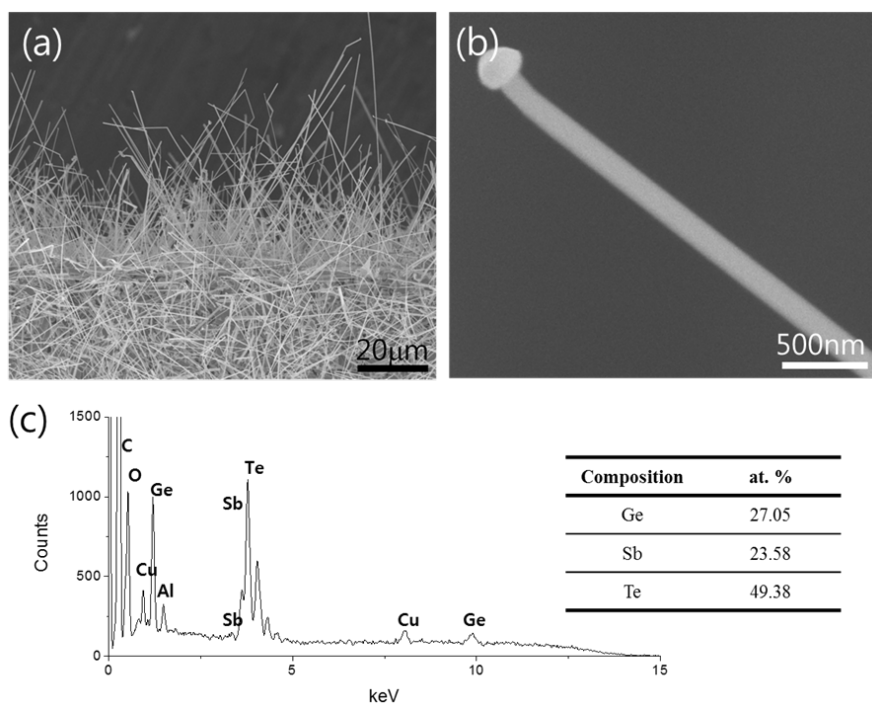


Figure 4.11. Morphology and chemical composition of GST nanowires by SEM and EDS analysis: (a) low magnification, and (b) high magnification SEM images of GST nanowires, and EDS spectrum with chemical composition.

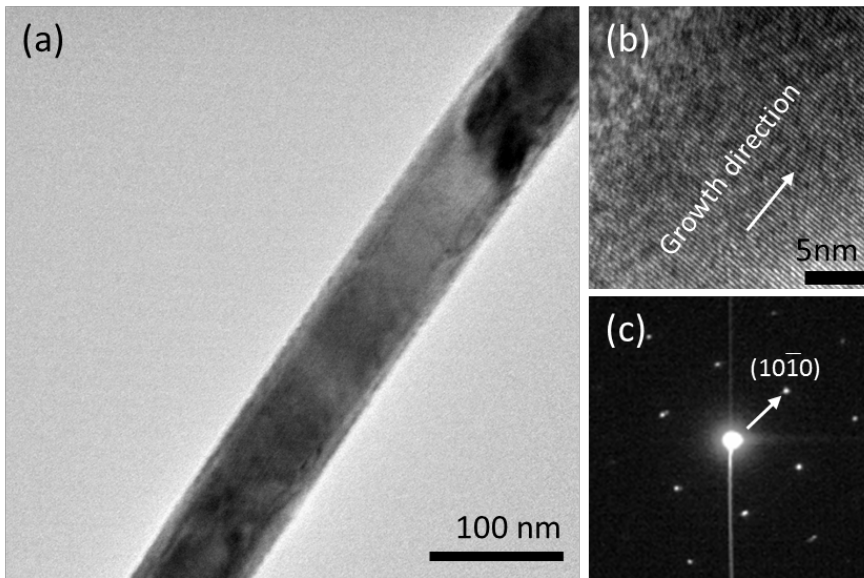


Figure 4.12 (a) Bright field TEM image of a single crystalline GST nanowire, (b) high-resolution TEM image of the nanowire: the white arrow indicates the growth direction of the nanowire, (c) diffraction pattern of hexagonal GST structure (ZA [0001])

#### 4.4.2. Young's modulus of GST nanowire

Young's modulus of GST nanowires were measured by in-situ uniaxial tensile test inside the scanning electron microscope (SEM) chamber. Individual GST nanowire was mounted on a microelectromechanical system (MEMS)-based tensile testing device (Figure 4.13 (a-b)) and controlled uniaxial tensile strain was applied. Nanowires were drop cast onto a lacey carbon TEM grid and a single nanowire was harvested using a nanomanipulator inside a SEM chamber. The single GST nanowire was aligned to the grips of the MEMS device and clamped using electron beam induced Pt-C deposition (Figure 4.13 (c)). Force on the specimen was measured by the displacement of the load cell, which consists of a compound flexure beam system with a stiffness of 44 N/m. Displacements of the nanowire, the actuator, the load cell, and on the substrate beneath the suspended grips were determined from SEM image series with resolution better than 0.1 pixels or 1 nm. The effective engineering strain was measured from the relative displacements of the two grips and the original gauge length. Typical engineering stress-strain curves of GST nanowires during loading-unloading was shown in Figure 4.13 (d). GST nanowire with diameter of 240 nm (red curve in Figure 4.13 (d)) showed elastic behavior. Smallest nanowire (d=115 nm) appeared to be capable of measurable albeit limited inelastic deformation (blue curve in Figure 4.13 (d)). Given relatively low elastic modulus of the material, the nanowires can sustain ~1 to 1.5% elastic

strain before inelastic deformation. Young's modulus of GST nanowires was size-independent over the range of 100~300 nm, with an average value of ~45 GPa as shown in Figure 4.13 (e). This is slightly higher than thin films measurements<sup>49</sup>, which give ~35 GPa (assuming a Poisson's Ratio of 0.3). The measured Young's modulus was used to calculate the piezoresistive coefficient of GST nanowire.

The GST phase change memory device was uniaxially strained by bending the PI substrate. When the substrate is bent upward (downward), the top surface is in tension (compression), and the bottom surface is in compression (tension). One surface inside the sheet, known as the neutral surface, has no strain. The strain in the top surface in the bending direction equals the distance from the neutral surface divided by  $R$ . Uniaxial strain in the top surface is given by<sup>50</sup>

$$\varepsilon = (d_S + d_{NW})/2R \approx d_S/2R \quad (4.11)$$

where  $d_S$ ,  $d_{NW}$ , and  $R$  were thickness of substrate, thickness of nanowire, and curvature radius, respectively. Since thicknesses GST nanowire and PI film were about 200nm ( $d_{NW}$ ) and 50 $\mu$ m ( $d_S$ ),  $d_{NW}$  was negligible for strain calculation due to large thickness difference. Therefore, uniaxial compressive (tensile) strain was exerted to GST NW when PI substrate was bent to downward (upward). Because the applied strain level was less than 0.4%, deflection or delamination of nanowire from the PI substrate was not observable during reversible straining from 0 to +/- 0.4% of uniaxial strain.

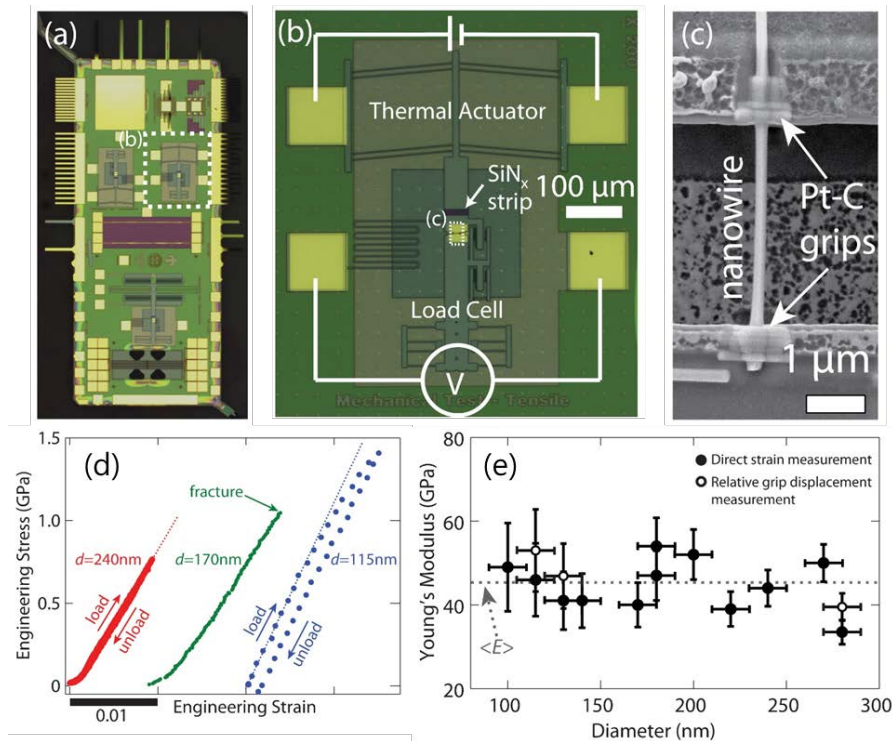


Figure 4.13 In-situ uniaxial tensile test of GST nanowire for Young's modulus measurement inside SEM chamber. (a-b) Optical images of the MEMS tensile testing device. (c) GST nanowire is attached to load cell using electron beam induced Pt-C deposition. (d) Engineering stress-strain curves with varying nanowire diameter. (e) Measured Young's modulus values of GST nanowire.

#### 4.4.3. Piezoresistivity in GST nanowire

To characterize the overall electrical response of a GST nanowire device, we applied a voltage sweep from -1.0 to 1.0 V and monitored the current flow in the GST NWs at different strain levels ranging -0.4 ~ +0.4 %. Figure 4.14 (a) illustrates the typical current (I) - voltage (V) characteristic of GST nanowire for various strain levels. Before introducing the external strain, strain free GST nanowire showed linear I-V characteristics with resistance of 13 k $\Omega$ , and ohmic behavior was readily established at the interfaces for the p-type nanowires studied here. As we introduced the external strain, resistance was linearly changed to 21.7 k $\Omega$  and 5.8 k $\Omega$  at the strain of 0.4% and -0.4%, respectively. The conductance increases under compression and decreased under tension. This trend is qualitatively consistent with typical p-type semiconductor<sup>51</sup>. Relative change of resistance (R) was surprisingly large up to  $\pm$  60%, and resistance change by strain were reversible.

As the nanowire became slightly narrower (thicker) under uniaxial tension (compression) due to Poisson's ratio, the change in resistance caused by an applied stress or strain is the result of not only from dimensional change, but also piezoresistance, which is the first report for GST nanowire.

Relative change in resistance was converted to relative change of resistivity by subtracting the dimensional changes of NWs as follows<sup>52</sup>,

$$R/R_o = (1 + 2\nu)\varepsilon + \rho/\rho_o \quad (4.12)$$

where  $\nu$  is the Poisson's ratio (0.3 for GST), and  $\varepsilon$  is the uniaxial strain along the GST nanowire with resistance,  $R$ . The resistance and the resistivity in the strain free GST are denoted by  $R_o$  and  $\rho_o$ , respectively. Since the changes in resistance are significantly larger than the dimensional changes, it is worth noting that GST nanowire as p-type semiconductor showed large piezoresistance effect.

The quantitative relation between resistivity and stress/strain is given by the fourth-rank piezoresistance tensor<sup>1</sup>. When a uniaxial stress is applied and the electric field and current are along the same direction, the longitudinal piezoresistance coefficient<sup>53</sup> can be measured and defined as the relative change in resistivity per unit stress as follows,

$$\pi_l^\rho = \frac{1}{X} \frac{\Delta\rho}{\rho_o} \quad (4.13)$$

where  $\rho_o$  is the resistivity under zero stress and  $X$  is the stress. Uniaxial stresses were applied on GST nanowires along their lengths by bending the PI substrates. The longitudinal piezoresistance coefficients along the  $\langle 10\bar{1}0 \rangle$  direction was examined. The relationships between  $\Delta\rho/\rho_o$  and stress  $X$  are shown in Figure. 4.14 (b). Moreover, piezoresistance effect was linear in the stress range performed here due to low stress level. From the equation (4.13), we could obtain the  $\pi_l^\rho$  for  $\langle 10\bar{1}0 \rangle$  GST nanowires ranging from 92.5 to 448.5 x 10<sup>-11</sup> Pa<sup>-1</sup>, which is comparable to that for Si nanowire<sup>54</sup>.

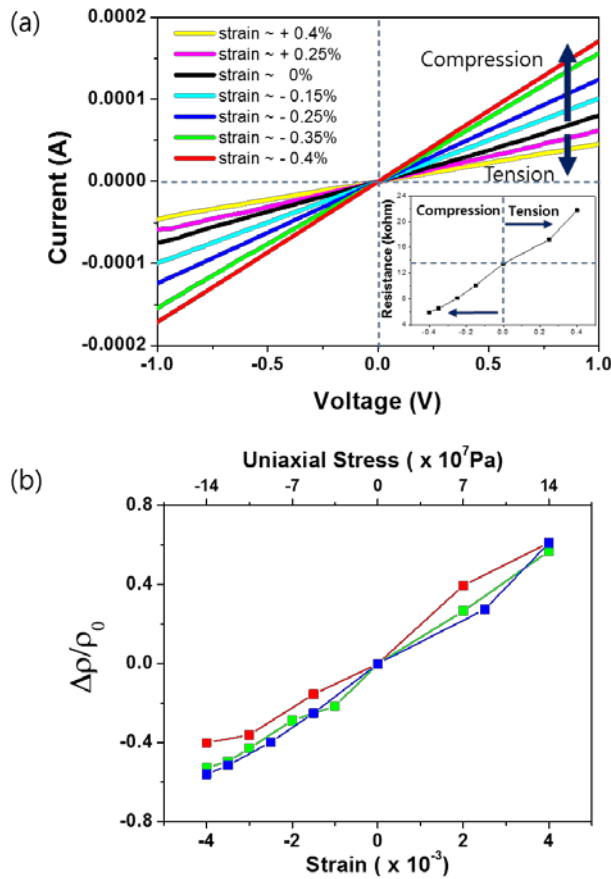


Figure 4.14 Current (I)-Voltage (V) measurement of GST NW under different strain condition: (a) I-V sweep curves of GST nanowire with uniaxial strain from -0.4% (compression) to 0.4% (tension), Inset shows resistance changes with external strain. Electrical measurements show that GST nanowire exhibits reversible responses to external strain, and original resistance was recovered after releasing strain. (b) Plot of relative resistivity changes of representative GST nanowires vs. external strain and stress representing piezoresistance effect.

#### 4.4.4 Origin of piezoresistivity in GST

##### - Stress induced variation of melting temperature

Since GST in one dimensional nanowire, we firstly consider the variation of  $T_c$  (crystallization temperature) by applying stress. Modified  $T_c$  by uniaxial stress is given by the Clausius-Clapeyron equation<sup>55</sup>,

$$\frac{dT_c}{d\sigma} = \frac{\varepsilon_o T_c^o}{\Delta H} \quad (4.14)$$

$$\frac{\Delta T_c}{T_c^o} = \frac{\varepsilon_o \Delta\sigma}{\Delta H} \quad (4.15)$$

Where  $\Delta H$  is the latent heat of transition ( $\sim 610\text{J}/\text{cm}^3$ <sup>56</sup>), maximum uniaxial stress ( $\Delta\sigma$ ) in this study is  $\sim 0.14$  GPa.  $\Delta T_c/T_c$  was 0.0043, which is negligible change in transition temperature. This implies that uniaxial stress induced conductivity tuning is originated from the electronic properties and band structure.

##### - Effect of band gap, carrier concentration and mobility

For both theoretical considerations and practical applications, it is worth examining whether band gap, carrier concentration or mobility plays the dominant role these remarkable resistivity change for GST nanowires.

Generally, stress-induced conductivity rise for semiconductor is often associated with the broadening and eventual overlap of the valence and conduction band<sup>57</sup> due to the shortening and the rotation of bond (change in

bond lengths and bond angles). Xu et al. reported that resistance of hexagonal GST (h-GST) declines monotonically with increasing hydrostatic pressure<sup>58</sup>. And they concluded that dependency of the resistivity on the hydrostatic pressure as follows,

$$\frac{d \ln R}{dP} = \frac{d \ln \rho}{dP} = \frac{d \ln 1/n}{dP} = \frac{1}{2k_B T} \frac{dE_g}{dP} \quad (4.16)$$

Where  $E_g$  is the electronic band gap of semiconductor, and  $P$  denotes the hydrostatic pressure. As we know, in many chalcogenide semiconductors the energy gap decreases as the pressure increases, or  $dE_g/dP < 0$ <sup>57,58</sup>. According to their work, there needs high pressure over several GPa levels of stress to change the band gap ( $dE_g/dP \sim -0.04 \text{ eV/GPa}$ ). However, very small stresses of maximum 0.14 GPa were applied to GST nanowire as shown in Figure 4.14. Therefore, there would be negligible changes of band gap and carrier concentration. This relation showed that a significant change in resistivity and origin of piezoresistance effect can only be attributed to a significant mobility change. Relationship between resistivity, carrier mobility, and effective mass can be defined as follows,

$$\rho = \frac{1}{\sigma} = \frac{1}{q(n\mu_n + p\mu_p)} = \frac{1}{qp\mu_p} \quad (4.17)$$

$$\mu_p = \frac{q\tau_{mp}}{m_p^*} \quad (4.18)$$

$$\frac{1}{\hbar^2} \frac{d^2 E}{dk^2} = \frac{1}{m^*} \quad (4.19)$$

where,  $q$ ,  $n$ ,  $p$ ,  $\mu_n$ ,  $\mu_p$ , and  $m^*$  are charge of carrier ( $1.602 \times 10^{-19}$  C), carrier concentrations of electron and hole, electron mobility, hole mobility, and effective mass, respectively. Because GST is p-type semiconductor, majority carriers are hole, and stress dependent hole mobilities, which originated from effective mass deviation from band diagram under stress, were calculated. With hole concentration of  $\sim 10^{20} \text{ cm}^{-3}$  for crystalline GST<sup>37</sup>, relative change in hole mobility is tuned to 130% (at strain -0.4%), which is remarkable hole mobility enhancement. Since GST nanowire (diameter less than 100nm) can sustain the elastic strain up to 1.5%, hole mobility could be even more enhanced up to 480%.

#### 4.4.5 Effect of stress on phase change behavior

As a phase change memory device, resistance of amorphous and crystalline phases were compared according to the stress. And threshold switching behavior was conducted. As shown in Figure 4.15, both of crystalline and amorphous GST showed higher (lower) resistance when tensioned (compressed) and change in threshold voltage was almost linear to the change in resistance of amorphous GST. Han et al. reported that compressive pressure increased the densities of fourfold rings in amorphous GST, shifting the local order toward the crystalline phase, which lower the activation energy toward crystallization<sup>57</sup>.

Therefore, PCM device is expected to show fast crystallization when compressed.

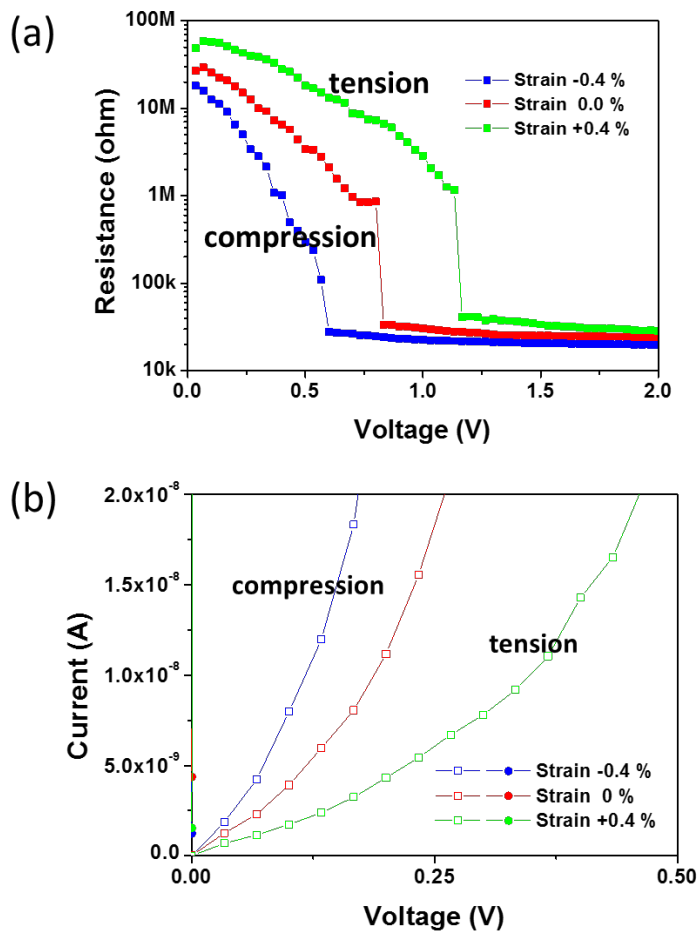


Figure 4.15 Resistance of amorphous and crystalline GST nanowire under the compressive (blue), tensile (green) stress and unstrained (red) state

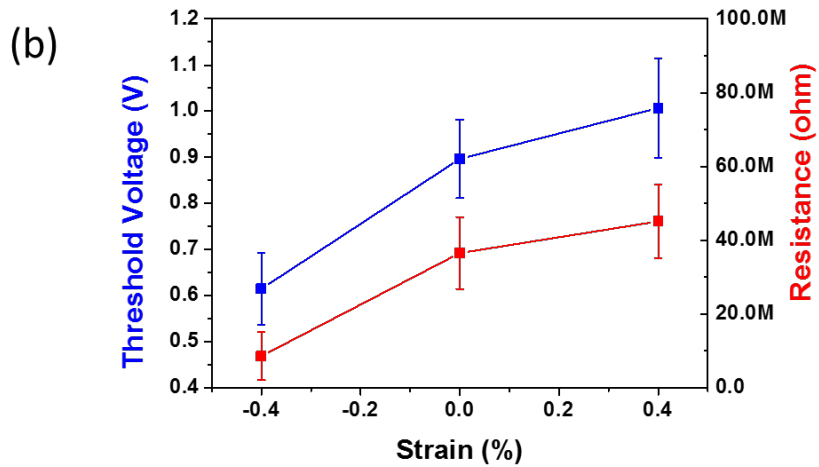
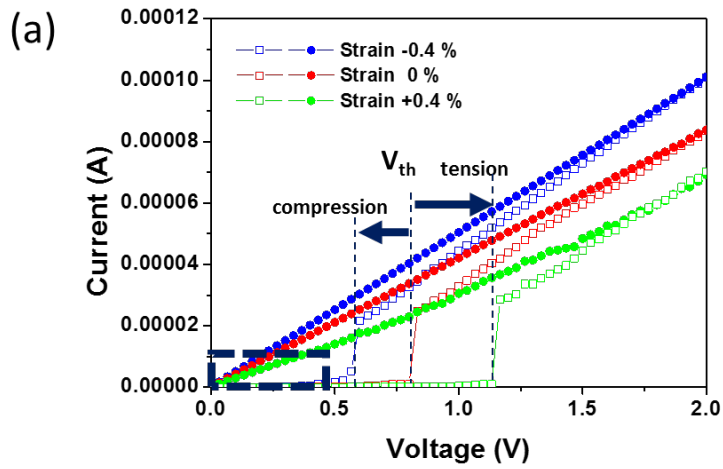


Figure 4.16 (a) Threshold switching behavior of GST and (b) relation between threshold voltage and resistance

## 4.5 Conclusion

Strain engineering can be utilized to tune the properties of phase change materials (PCM) for the applications in advanced electronic and memory devices. Recently, the effects of strain or stress on the phase changing properties of  $\text{Ge}_2\text{Sb}_2\text{Te}_5$  (GST) are being investigated to further expand our insights into physics and applications of nanostructure materials. In this work, GST nanowires possess a large piezoresistive effect and stress/strain dependent electrical switching behavior of PCM devices. For example, the longitudinal piezoresistance coefficient along  $\langle 10\bar{1}0 \rangle$  direction for p-type GST NWs reach as high as  $440 \times 10^{-11} \text{ Pa}^{-1}$ , which is comparable to the values of Si. Large piezoresistivity of GST was originated from the hole mobility enhancement. This piezoresistance effect in GST may have significant implication in PCM device to further expand its application to flexible electronics.

## 4.6 References

1. J. Bryzek, *MEMS: A closer look at part2*, Sensors, (1996).
2. W. Thomson, *Proc. R. Soc. London* **8**, 546 (1856).
3. H. Tomlinson, *Proc. R. Soc. London* **25**, 451 (1876).
4. H. Tomlinson, *Philos. Trans. R. Soc. London* **174**, 1 (1883).
5. P.W. Bridgman, *Proc. Nat. Acad. Sci. U.S.A.* **10**, 411 (1924).
6. W.E. Williams, *Phil. Mag.* **13** (1907).
7. M. Allen, *Phys. Rev.* **42**, 848 (1932).
8. M. Allen, *Phys. Rev.* **43**, 569 (1933).
9. M. Allen, *Phys. Rev.* **49**, 248 (1936).
10. J.W. Cookson, *Phys. Rev.* **47**, 194 (1935).
11. J. Curie, P. Curie, *C. R. Acad. Sci.* **91**, 294 (1880).
12. W. Voigt, *Lehrbuch der Kristallphysik. Leipzig (mit ausschluss der kristalloptik)* Springer-Verlag (2014).
13. J. Bardeen, W. Shockley, *Phys. Rev.* **80**, 72 (1950).
14. C.S. Smith, *Phys. Rev.* **94**, 42 (1954).
15. W.G. Pfann, R.N. Thurston, *J. Appl. Phys.* **32**, 2008 (1961).
16. O.N. Tufte, *J. Appl. Phys.* **33**, 3322 (1962).
17. K.E. Petersen, *Proc. IEEE* **70**, 420 (1982).
18. A. Hierlemann, D. Lange, C. Hagleitner, N. Kerness, A. Koll, O. Brand, H. Baltes, *Sensor. Actuat. B* **70**, 2 (2000).
19. M. Tortonese, R.C. Barrett, C.F. Quate, *Appl. Phys. Lett.* **62**, 834 (1993).
20. W. A. Brantley, *J. App. Phys.* 44, 534 (1973).
21. I. S. Sokolnikoff, *Mathematical Theory of Elasticity*. Malabar, FL: R.E. Krieger Pub. Co. (1983).
22. H. Rolnick, *Phys. Rev.* **36**, 506 (1930).
23. Y. Kanda, *IEEE Tran. Elect. Dev.* **19**, 64 (1982).

24. T. Toriyama, S. Sugiyama, *J. Microelectromechanical Sys.* **11**, 598 (2002).
25. S.R. Ovshinsky, *Phys. Rev. Lett.* **21**, 1450 (1968).
26. M. Wuttig, N. Yamada, *Nat. Mater.* **6**, 824 (2007).
27. E. Bozorg-Grayeli, J.P. Reifenberg, M. Asheghi, H.-S.P. Wong, K.E. Goodson, *Annual Review of Heat Transfer* **16**, 397 (2013).
28. M. Chen, K.A. Rubin, R.W. Barton, *Appl. Phys. Lett.* **49**, 502 (1986).
29. N. Yamada, M. Takao, M. Takenaga, *Proc. SPIE* **695**, 79 (1987).
30. N. Yamada, E. Ohno, K. Nishiuchi, N. Akahira, M. Takao, *J. Appl. Phys.* **69**, 2849 (1991).
31. A. Pirovano, A.L. Lacaita, A. Benvenuti, F. Pellizzer, R. Bez, *IEEE Trans. Electron Devices* **51**, 452 (2004).
32. A. Kolobov, P. Fons, A.I. Frenkel, A.L. Ankudinov, J. Tominaga, T. Uruga, *Nat. Mater.* **3**, 703 (2004).
33. N. Yamada and T. Matsunaga, *J. Appl. Phys.* **88**, 7020 (2000).
34. T. Nonaka, G. Ohbayashi, Y. Toriumi, Y. Mori, and H. Hashimoto, *Thin Solid Films* **370**, 258 (2000).
35. B.-S. Lee, J.R. Abelson, S.G. Bishop, D.-H. Kang, B.-K. Cheong, K.-B. Kim, *J. Appl. Phys.* **97**, 093509 (2005).
36. N.F. Mott, E.A. Davis, *Electronic Processes in Non-crystalline Materials*, Clarendon, Oxford (1967).
37. M.H. Cohen, H. Fritzsche, S.R. Ovshinsky, *Phys. Rev. Lett.* **22**, 1065 (1969).
38. S.R. Ovshinsky, *Phys. Rev. Lett.* **36**, 1469 (1976).
39. M. Kastner, D. Adler, H. Fritzsche, *Phys. Rev. Lett.* **37**, 1504 (1976).
40. M. Kastner, H. Fritzsche, *Philos. Mag. B* **37**, 199 (1978).
41. K. Kunghia, Z. Shakoor, S. O. Kasap, and J. M. Marshall, *J. Appl. Phys.* **97**, 033706 (2005).
42. A.C. Warren, *IEEE Trans. Electron Devices* **20**, 123 (1973).
43. D. Adler, H.K. Henisch, S.D. Mott, *Rev. Mod. Phys.* **50**, 209 (1978).

44. D. Adler, M. S. Shur, M. Silver, and S. R. Ovshinsky, *J. Appl. Phys.* **51**, 3289 (1980)
45. S.A. Baily, H.L.D. Emin, *Solid State Commun.* **139**, 161 (2006).
46. E.J. Yoffa, D. Adler, *Phys. Rev. B* **15**, 2311 (1977).
47. S.-H. Lee, Y. Jung, R. Agarwal, *Nat. Nanotechnol.* **2**, 626 (2007).
48. Z. Fan, J.C. Ho, Z.A. Jacobson, R. Yerushalmi, R.L. Alley, H. Razavi, A. Javey, *Nano Lett.* **8**, 20 (2008).
49. T.P.L. Pedersen, J. Kalb, W.K. Njoroge, D. Wamwangi, M. Wuttig, F. Spaepen, *Appl. Phys. Lett.* **79**, 3597 (2001).
50. Z. Suo, E.Y. Ma, H. Gleskova, S. Wagner, *Appl. Phys. Lett.* **74**, 1177 (1999).
51. S.E. Thompson, et al., *IEEE Trans. Electron Devices* **51**, 1790 (2004).
52. A. Lugstein, M. Steinmair, A. Steiger, H. Kosina, E. Bertagnolli, *Nano Lett.* **10**, 3204 (2010).
53. W.P. Mason, R.N. Thurston, *J. Acoust. Soc. Am.* **29**, 1096 (1957).
54. R. He, P. Yang, *Nat. Nanotechnol.* **1**, 42 (2006).
55. J. Cao et al., *Nat. Nanotechnol.* **4**, 732 (2009).
56. S. Senkader, C.D. Wright, *J. Appl. Phys.* **95**, 504 (2004).
57. J. Im, E. Cho, D. Kim, H. Horii, J. Ihm, S. Han, *Phys. Rev. B* **81**, 245211 (2010).
58. B. Xu, Y. Su, Z.G. Liu, C.H. Zhang, Y.D. Xia, *Appl. Phys. Lett.* **98**, 142112 (2011).

## Chapter 5. Conclusion

In this thesis, I investigated the effect of external stress on (1) the growth of indium nanowire, and (2) piezoresistive effect in phase change  $\text{Ge}_2\text{Sb}_2\text{Te}_5$  nanowires.

First, external stress driven nanowire growth was characterized. External stress was induced by using  $\text{Ga}^+$  focused ion beam. To develop and optimize the ion beam induced indium nanowire growth, the effect of major growth parameters such as acceleration voltage, current density was investigated for the controlled growth. Since focused ion beam can be precisely controlled by changing the accelerating voltage, current density, and location of irradiation, the diameter and length of the nanowires as well as their growth rate could be effectively controlled. Indium nanowires with diameter of 40-200 nm and length up to 120  $\mu\text{m}$  were fabricated at growth rate as high as 500 nm/s, which is remarkably faster compared with other nanowire growth methods. Indium source for nanowire growth was originated from the ion beam induced InGaN phase decomposition. And compressive stress generated by ion beam irradiation and stress migration of indium atoms was the driving force for indium nanowire growth. Nanowires could be synthesized on desired areas of the substrate by simply controlling the regions exposed to the ion beam using maskless patterning. Extension of the developed technique allows for fabrication of variety of functional networks of indium nanowires, with control

over individual nanowires sites and dimensions.

Second, stress and strain engineering can be utilized to tune the properties of phase change materials (PCM) for the applications in advanced electronic and memory devices. Recently, the effects of strain or stress on the phase changing properties of  $\text{Ge}_2\text{Sb}_2\text{Te}_5$  (GST) are being investigated to further expand our insights into physics and applications of nanostructure materials. In this work, GST nanowires possess a large piezoresistative effect and stress/strain dependent electrical switching behavior of PCM devices. For example, the longitudinal piezoresistance coefficient along  $\langle 10\bar{1}0 \rangle$  direction for p-type GST NWs reach as high as  $440 \times 10^{-11} \text{ Pa}^{-1}$ , which is comparable to the values of Si. Large piezoresistivity of GST was originated from the hole mobility enhancement. This piezoresistance effect in GST may have significant implication in PCM device to further expand its application to flexible electronics, memories, and strain sensors.

## **Appendix I. UV-responsive nanoparticle and its application to oil recovery**

### **6.1 Oil absorption/desorption materials and wettability**

Collecting oil in the ocean or other bodies of water has been considered as a challenging environmental issue. Therefore, oil collection has become a highly important research topic due to the increasing amounts of industrial oily wastewater and frequent oil spills. Several methods for oil cleanup have been developed, such as the use of oil absorbents or oil skimmers<sup>1-4</sup>. However, recovered oil by these methods typically contain at least 5~10% of water<sup>3,4</sup>. To separate oil from water, recent approaches have focused on controlling the wettability of the oil or water. Two types of structures or materials have been explored: oil removal and water removal. The oil-removing materials are required to have superhydrophobicity while possessing superoleophilicity in air, to absorb only the oil from the water under the surface by using various porous sponge-like materials<sup>5-11</sup>. However, because oil-removing materials are easily fouled by high oil adhesion due to their oleophilic nature, the reusability of the materials is limited by degraded separation or absorption capacity<sup>7,8</sup>. In the case of water-removing materials, the wettability needs to be superhydrophilic; however, the material or structure needs to be superoleophobic underwater<sup>12-18</sup>. Due to high water adhesion to the material surface, water has a very low wetting

angle. The underwater superoleophobic interface with low affinity for oil drops prevents the coated materials from oil fouling, which makes the oil and the material to be easily recycled. Therefore, this water-removing property has been applied to oil-water separation filters<sup>13-18</sup>.

Recently, it has been reported that surface wettability can be switched or tuned using external stimuli such as light irradiation<sup>19,20</sup>, mechanical loading<sup>21</sup>, chemical treatment<sup>22</sup>, electric fields<sup>23</sup>, magnetic fields<sup>24</sup>, temperature<sup>25</sup>, and pH<sup>26,27</sup>. In particular, switchable wettability between superhydrophilicity and superhydrophobicity has been studied on various photo-responsive materials such as TiO<sub>2</sub><sup>28-32</sup>, ZnO<sup>19</sup>, and SnO<sub>2</sub><sup>20</sup>. The switchable wettability of TiO<sub>2</sub> has been reported. Its original water CA of 35° undergoes a dramatic wettability transition due to UV irradiation, causing it to become superhydrophilic with a CA<sub>water/air</sub> less than 5°; however, the underwater oleophobicity increases, as evidenced by the change in the oil (heptane) CA underwater from 146° to 167°<sup>30</sup>. The role of TiO<sub>2</sub> under UV irradiation is known to enhance the surface superhydrophilicity and underwater superoleophobicity. Thus, UV irradiation on TiO<sub>2</sub> enables versatile applications for antifogging and self-cleaning<sup>28</sup>, photo-controllable oil/water filtration<sup>30</sup>, and water purification<sup>31</sup>. Although many researchers have focused on oil/water separation using photo-responsive TiO<sub>2</sub>, the uses of wettability conversion between hydrophilicity and hydrophobicity are limited to mesh type filtration<sup>30</sup>. To work as oil absorbing materials in the presence of water, TiO<sub>2</sub> should have both hydrophobicity and

oleophilicity. However, as-prepared TiO<sub>2</sub> surface typically shows hydrophilicity, and subsequent surface modifications are needed to be hydrophobic, which degraded by UV irradiation<sup>32</sup>. Furthermore, a TiO<sub>2</sub>-coated nanocellulose aerogel was reported to show photo-induced switchable wettability<sup>33</sup>, illustrating that water could be absorbed and repelled with and without UV irradiation. However, the main focus of the paper is to explore the photo-induced switchable water absorption and wettability.

## **6.2 Experimental procedure**

### **6.2.1. Synthesis of hydrocarbon and TiO<sub>2</sub> nanoparticles (NPs)**

Hydrocarbon NPs<sup>11</sup> were deposited by glow discharge on the bottom of a vacuum chamber. The chamber was evacuated to a base pressure of approximately  $2 \times 10^{-5}$  Torr. C<sub>2</sub>H<sub>2</sub> was introduced into the chamber at a flux rate of 20 sccm (standard cubic centimeter per minute) as the hydrocarbon precursor. The deposition temperature of the bottom of chamber was held at room temperature by water cooling, and the working pressure was maintained at 500 mTorr. The discharge was sustained at a radio frequency (RF) and power of 13.56 MHz and 600 W for a total process time of 30 min. TiO<sub>2</sub> nanoparticles<sup>50</sup> were prepared by chemical vapor synthesis (CVS) using titanium tetrakispropoxide (TTIP, 98%; Junsei, Japan) as the precursor for Ti. The

nebulized precursor mist was transported into the preheated tube furnace ( $\sim 1350^\circ\text{C}$ ) with nitrogen as a carrier gas; the gas then reacted with the oxygen gas that was supplied separately. The respective flow rates of nitrogen and oxygen were controlled at 4.0 and 5.0 slm (standard liter per minute), respectively. The synthesized  $\text{TiO}_2$  NPs were collected in a thermophoretic chamber equipped with halogen lamps and cooling jackets. The  $\text{TiO}_2$  NPs deposited on the surface of cold jackets were scraped off as a white powder.

### 6.2.2. Fabrication of nanoparticle sponge (nano-sponge)

Hydrocarbon<sup>11</sup> and  $\text{TiO}_2$ <sup>50</sup> NPs were synthesized by glow discharge and chemical vapor synthesis, respectively. Because both hydrocarbon and  $\text{TiO}_2$  NPs have similar diameters ( $\sim 30$  nm in average), hydrocarbon/ $\text{TiO}_2$  NPs were mixed at the volume ratios of 10/0, 8/2, 6/4, 4/6, 2/8, and 0/10 (Figure 6.1 and Table 6.1). The mixed NPs were dispersed in isopropyl alcohol (IPA) and were ultrasonicated. IPA solutions containing hydrocarbon/ $\text{TiO}_2$  NPs with different volume ratios were coated by drop casting on glass slides. The slides were left to evaporate and were used to measure both the water and oil contact angle in the air and the oil contact angle underwater.

### 6.2.3 Fabrication of the NS/p-PDMS

A porous PDMS was selected as the membrane for oil absorption-desorption experiments under UV irradiation. Because PDMS has high transmittance and

low absorption under UV irradiation, TiO<sub>2</sub> NPs within a Nano-sponge coated porous PDMS can act as a photocatalyst for hydrocarbon decomposition and display a wettability transition for oil absorption and desorption. The porous PDMS was fabricated using a sugar templating method.<sup>[6]</sup> The fabricated porous PDMS was dipped into IPA solutions containing hydrocarbon/TiO<sub>2</sub> NPs, ultrasonicated for 10 min, and finally dried in a vacuum chamber.

#### 6.2.4 Characterization methods

A scanning electron microscope (SEM, Inspect F50, FEI) operated at an accelerating voltage of 10 keV, which was used to observe the morphology and configuration of hydrocarbon/TiO<sub>2</sub> NPs. All of the specimens for SEM observation were coated with Pt to reduce the charging effect. Compositional analysis was performed using energy-dispersive X-ray spectroscopy (EDS) to confirm the compositional ratio of the mixed NPs. High-resolution transmission electron microscopy (HR-TEM) and electron energy loss spectroscopy (EELS) were used to confirm the distribution of hydrocarbon and TiO<sub>2</sub> NPs, with the corresponding compositional mapping of carbon, oxygen, and titanium. CA was measured by sessile drop method, after 5 seconds from the liquid drop placement on the surface for stabilization, and it was kept constant for each CA measurement. The UV-responsive wettability of the nano-sponge coated glass slides was characterized by measuring the CA of deionized (DI) water and oil (n-hexane) droplets in the air and underwater, respectively. After each nano-

sponge was UV-irradiated for 2 hours (18 W Hg lamp with wavelength 280~360 nm and irradiance of 51  $\mu\text{W}/\text{cm}^2$ ) with a distance of ~10 cm between the UV light source and the specimen, superhydrophilicity in the air and superoleophobicity underwater were realized. For the CA measurements of DI water in air, droplets of approximately 5  $\mu\text{L}$  were gently deposited on the substrates, using a microsyringe. To measure the underwater oil CA, the nano-sponge coated glass slides were inverted and placed in a transparent container filled with DI water. Then, oil drops were gently inserted by a syringe needle to the coated surface. All of the measurements were recorded using a digital camera at room temperature. Two different types of oils, n-hexane (density of 0.6548 g/ml) as a light oil and 3 M Fluorinert FC-770 lubricant (density of 1.793 g/ml) as a heavy oil, were tested for the release of the adhered oil under UV irradiation. The effects of  $\text{TiO}_2$  on the wetting transition and the oil release behaviors with UV irradiation were evaluated by comparing the oil desorption from the 10/0 and 6/4 (hydrocarbon/ $\text{TiO}_2$ ) nano-sponges. X-ray photoelectron spectroscopy (XPS, PHI 5000 VersaProbe (Ulvac-PHI)) was used to determine the binding energy of the 6/4 nano-sponge before and after UV irradiation. The background pressure was decreased to  $\sim 6.7 \times 10^{-8}$  Pa. The XPS data were collected using monochromatized Al K $\alpha$  radiation at 1486.6 eV. All of the binding energies were calibrated using the C 1s peak at 284.6 eV. Gas bubbles grown on the surface of the nano-sponge during UV irradiation were collected

under water. To prevent interference by other gas molecules in the atmosphere, the collected gas bubble were directly injected to a Quadrupole mass spectroscopy (HPR20, Hiden Analytical) with He as a carrier gas; the sample were analyzed to identify and quantify the gas phases. UV-visible spectrophotometer (Varian Cary 100) was used to investigate the transmission of UV light into the NS/p-PDMS. Additional air bubble flow was supplied to the NS/p-PDMS to enhance the oil desorption rate, after crude oil (32.8° API, density: 860 kg/m<sup>3</sup>) absorption under UV irradiation.

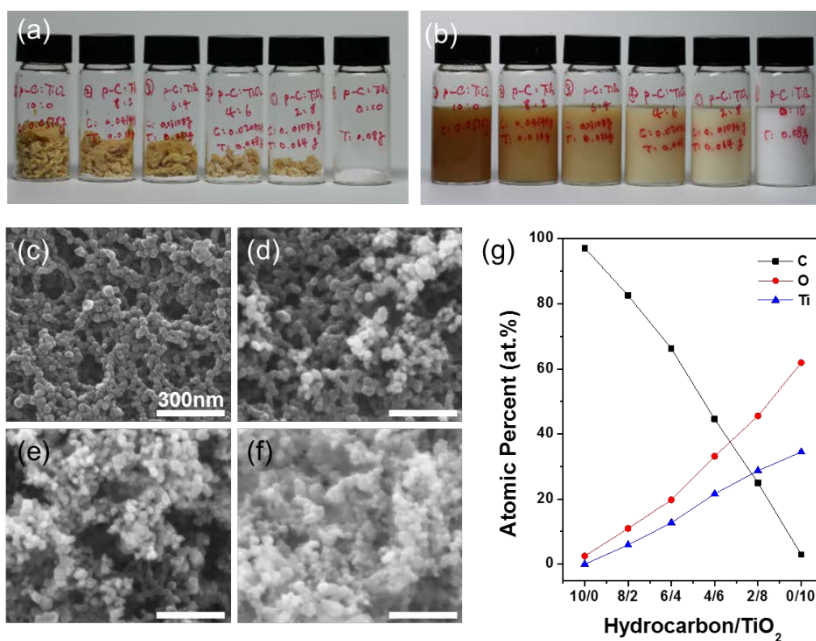


Figure 6.1 Preparation of nano-sponge, composed of Mixture of hydrophobic hydrocarbon and hydrophilic TiO<sub>2</sub> nanoparticles and the surface morphology and chemical composition of the nano-sponge using scanning electron microscopy (SEM) and energy-dispersive X-ray spectroscopy (EDS). Photograph of hydrocarbon/TiO<sub>2</sub> NPs (a) before and (b) after mixing in an IPA solution. SEM images of the nano-sponges (hydrocarbon/TiO<sub>2</sub> NPs) with volume ratios of (c) 10/0, (d) 6/4, (e) 4/6 and (f) 0/10. (g) Atomic composition of the nano-sponges with different mixing volume ratios measured with EDS.

Hydrocarbon [g]	TiO <sub>2</sub> [g]	Volume mixing ratio [Hydrocarbon/TiO <sub>2</sub> ]	Carbon (at.%)	Oxygen (at.%)	Titanium (at.%)
0.0518	0.0	10 / 0	97.11	2.5	0.0
0.04144	0.016	8 / 2	82.58	10.98	5.93
0.03108	0.032	6 / 4	66.28	19.74	12.74
0.02072	0.048	4 / 6	44.56	33.15	21.61
0.01036	0.064	2 / 8	25.0	45.57	28.71
0.0	0.08	0 / 10	2.94	61.92	34.47

Table 6.1 Weight and volume mixing ratio of each nano-sponge and its atomic composition determined using energy-dispersive X-ray spectroscopy.

## 6.3 Results and Discussion

### 6.3.1 Tunable surface wettability underwater

Because surface wettability is determined by the surface chemical composition and microstructure, changing the mixing ratio of hydrocarbon and  $\text{TiO}_2$  in each nano-sponge would provide different wettabilities for water or oil in different environments, such as in air or underwater. As shown in Figure 6.2 and 6.3, the surface wettabilities of water and oil (n-hexane) on a glass slide coated with the nano-sponge were explored in air and water. The CAs for water and oil in the air were measured with respect to the mixture ratio before and after UV irradiation, as shown in Figure. 6.3. By increasing the  $\text{TiO}_2$  content on the nano-sponge coated flat glass slide, the water CA in the air reduced from  $128^\circ$  for the mixing ratio of 10/0 (hydrocarbon/ $\text{TiO}_2$ ) to  $0^\circ$  for that of 0/10. This indicates that the surface wettability could be controlled from mild hydrophobic to superhydrophilic without UV irradiation. However, all of the water CAs was significantly reduced upon UV irradiation. In the case of ratios from 4/6 to 0/10, the water CA was almost zero in the air. In the case of oil droplets, regardless of the  $\text{TiO}_2$  content and UV irradiation, superoleophilicity was exhibited on all of the samples in which oils were totally absorbed by the nano-sponge in the air. However, the underwater wettability for oil dramatically changed with respect to the sample composition and UV irradiation, as shown in Figure 6.3 (b). As the  $\text{TiO}_2$  content in the nano-sponge increased, the underwater

oleophobicity was enhanced from 45° for the 10/0 ratio to 125° for the 6/4 ratio. The samples with mixing ratios of 2/8 and 0/10 showed superoleophobicity underwater with CAs greater than 150°, even before UV irradiation. After UV irradiation, the underwater oil CAs were also improved and all of the samples except for the 10/0 ratio (131°) showed superoleophobicity with oil CAs over 150°.

The significant changes in underwater oil CA by UV irradiation were due to the changes in the surface energy of the nano-sponge. Thus, the work of adhesion or surface energy can be calculated using the Young-Dupré equation<sup>34,35</sup> as follows:

$$W_{ows} = \gamma_{ow}(1 + \cos \theta) \quad (6.1)$$

where  $W_{ows}$ ,  $\gamma_{ow}$ , and  $\theta$  are the work of adhesion in the oil-water-solid system, the interfacial tension of oil and water, and the apparent underwater oil CA, respectively. Theoretically, equilibrium CA should be used to calculate the work of adhesion. However, only the advancing CA can be reliably measured and derives minimum work of adhesion<sup>36</sup>. In this study, we assumed that the apparent CA is equivalent to advancing CA due to low CA differences less than 8°. Therefore, the work of adhesion was calculated by using apparent CA, and this would show a similar trend with the minimum work of adhesion calculated by using advancing CA. Because  $W_{ows}$  is the work necessary to separate a unit area of the oil-solid interface in water, it was calculated using the interfacial

tension of the oil-water and underwater oil CAs. The interfacial tension between n-hexane and water was measured as 50.2 mN/m, and each value of  $W_{ows}$  was calculated from equation (6.1) and plotted in Figure 6.3 (b). Before UV irradiation, oil droplets adhered onto the surfaces with ratios from 10/0 to 4/6. However, oil droplets adhered only to the samples with the ratios of 10/0 and 8/2 after UV irradiation. For the other mixing ratios, oil droplets easily rolled off the nano-sponge surface under water, with a very low sliding. As the underwater oil CA increased, the work of adhesion decreased, indicating that the interfacial adhesion of each nano-sponge drastically decreased with UV irradiation. The CAs under salt water (3.5% dissolved NaCl) were also compared with those of pure DI water, and it was found that the effect of salt was negligible. And there was a report that 10% of UV irradiation of 305 nm can reach maximum depth of 16 m in sea water<sup>37</sup>. Therefore, UV induced high contrast in work of adhesion is still effective for the application in the ocean.

Because the hydrophilicity increased as the oleophilicity decreased with UV irradiation, one can suppose that water may have a greater chance to replace oil at the nano-sponge and oil interface due to the increased water affinity. Therefore, the depletion of adhesion at the interface could be explained by photocatalytic oxidation (PCO) and the wetting transition of TiO<sub>2</sub> during UV irradiation<sup>38-40</sup>. X-ray photoelectron spectroscopy (XPS) measurements were performed to reveal the chemical state of the 6/4 nano-sponge before and after UV irradiation (Figure 6.3 (c)). The XPS data were analyzed for the C, O, and

Ti core levels of a 6/4 nano-sponge sample. The change in the C 1s spectrum clearly showed that the hydrocarbon (C-H, 284.6eV) was drastically decomposed into carboxyl carbon (O=C-O, 288.3eV) and oxidant carbon (C-O, 285.8eV). In addition, the change in the O 1s spectra corresponded to the adsorption of the hydroxyl group (-OH, 532.5eV), which converted the surface to a superhydrophilic surface after UV irradiation<sup>41</sup>. Before UV irradiation, the Ti 2p XPS spectrum showed two typical values of TiO<sub>2</sub> at 458.6 and 464.3eV, which were assigned to the binding energies of Ti 2p<sub>3/2</sub> and Ti 2p<sub>1/2</sub>, respectively. Additionally, two new peaks at 460.1 and 465.4 eV (related with Ti 2p<sub>3/2</sub> and Ti 2p<sub>1/2</sub>) with strong intensities were found and could be attributed to the presence of strong interactions at the interfaces between TiO<sub>2</sub> and hydrocarbon as Ti-O-C bond<sup>42</sup>. The formation of the Ti-O-C bond was also shown at 531.4eV in the O 1s spectrum before UV irradiation, and this bond was decomposed upon UV irradiation by the PCO of TiO<sub>2</sub>. As a result, one can consider that the oil-hydrocarbon interface may deteriorate due to the PCO of TiO<sub>2</sub> NPs. Therefore, the interfacial bond becomes very weak, and the water molecule may replace the decomposed sites of hydrocarbon NPs on the nano-sponge.

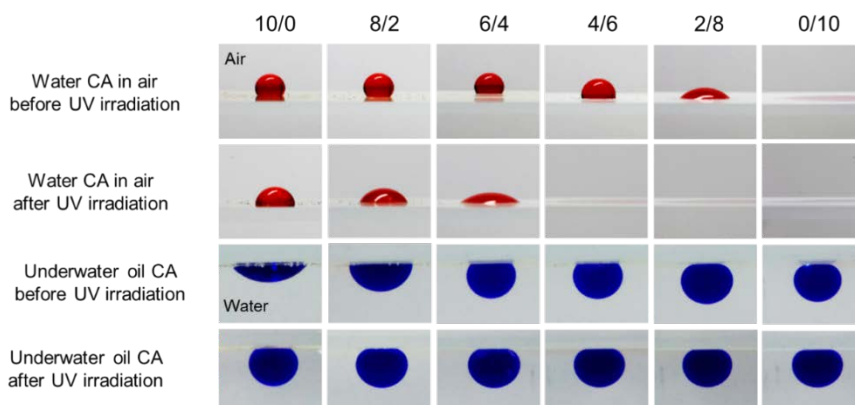


Figure. 6.2 Water CA in air and oil (n-hexane); CA underwater on the nano-sponges for each volume ratio (hydrocarbon/TiO<sub>2</sub>: 10/0, 8/2, 6/4, 4/6, 2/8, 0/10) before/after UV irradiation for 2 hrs

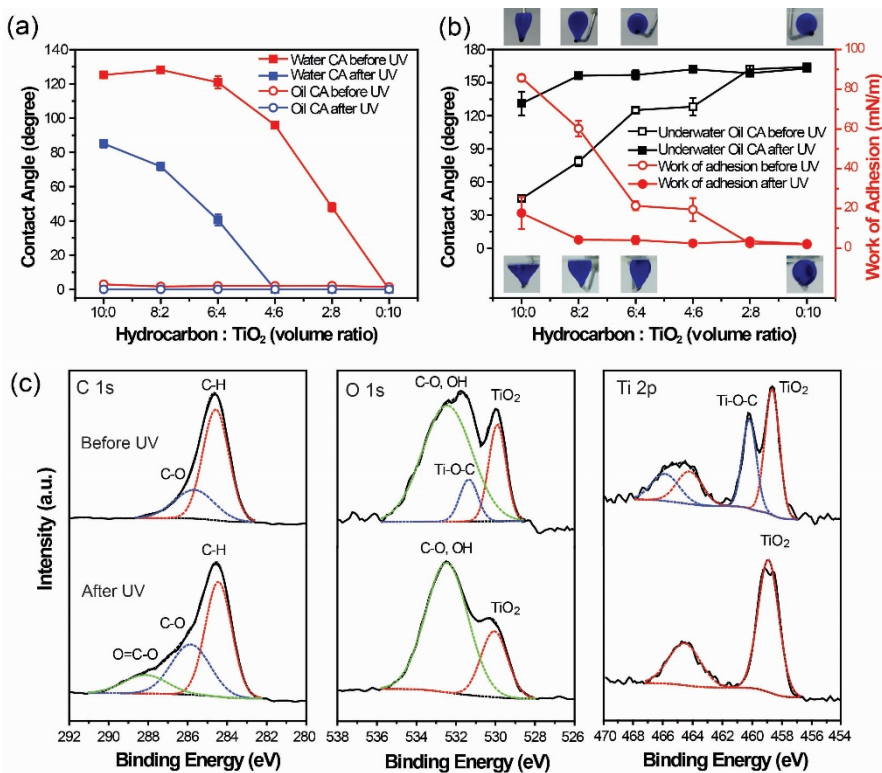


Figure 6.3 Surface wettability of water and oil (n-hexane) on a nano-sponge before and after UV irradiation. (a) Water and oil contact angle (CA) in air, (b) underwater oil CA and work of adhesion. Insets are snapshots of the oil droplets immediately prior to detachment from the injection needle before (lower inset) and after (upper inset) UV irradiation. (c) X-ray photoelectron spectroscopy analysis before (upper graph) and after (lower graph) UV irradiation

### 6.3.2 Spontaneous bubble growth

The underwater oil CAs were monitored *in-situ* under UV irradiation on the nano-sponge coated glass slide, as shown in Figure 6.4. A light oil droplet (n-hexane, density: 0.6548 g/ml) was placed on the 6/4 nano-sponge coated glass slide, in which the mixing ratio was selected to show high adhesion contrast; underwater oleophobicity with high adhesion before UV irradiation and superoleophobicity with low adhesion after UV irradiation. As the nano-sponge coated glass was immersed into water, air bubbles with an average volume of 0.015 mm<sup>3</sup> were trapped on the surface of the nano-sponge, which were mainly captured by the hydrophobic hydrocarbon NPs. As the oil droplet contacted the surface, the nano-sponge was partially wetted by the oil, resulting in a CA of 113°. Simultaneously, air bubbles trapped on the surface of nano-sponge were encapsulated within oil droplets due to the positive oil spreading coefficient,  $S_o$  (+4.2 mN/m for n-hexane). Interestingly, air bubbles encapsulated within oil droplets continuously grew with the increasing UV irradiation time, and the oil CA increased from 113° to 157°, which indicated that a wetting transition occurred from mild oleophobicity to superoleophobicity underwater. Several small bubbles began to grow and coarsen. Then, these bubbles became one larger bubble and provided increased buoyancy to the bubble containing the oil droplet until it finally released the oil droplet.

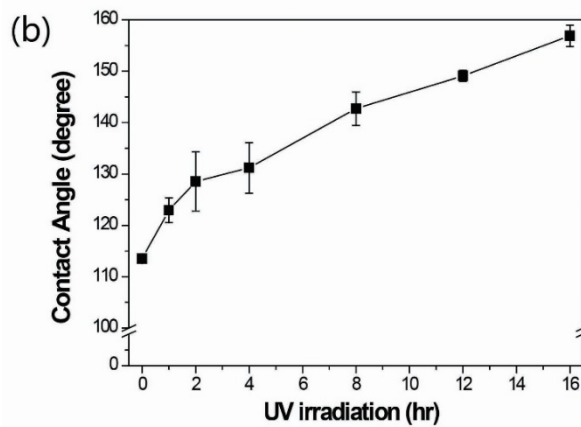
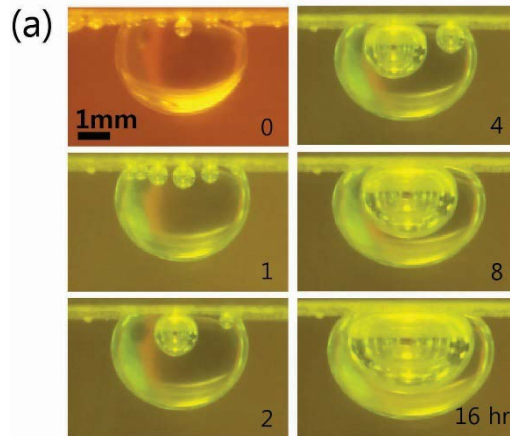


Figure 6.4 Spontaneous growth of bubbles within an oil droplet on the surface of nano-sponge underwater with UV irradiation. (a) Bubble growth within a light oil (n-hexane, density: 0.6548 g/ml) droplet in contact with 6/4 nano-sponge underwater with increasing UV irradiation times of 0, 1, 2, 4, 8, and 16 hr and (b) underwater oil CA measured from (a)

### 6.3.3 Oil absorption and desorption using the nano-sponge.

To investigate the self or spontaneous release of oil droplet due to TiO<sub>2</sub> on the wetting transition and hydrocarbon decomposition at the interface, heavy oil droplets (3M Fluorinert FC-770, density of 1.793 g/ml) were explored in contact with the nano-sponge coated glass slides with different mixing ratios of hydrocarbon/TiO<sub>2</sub> (6/4 and 10/0) under UV irradiation. Heavy oil was used to show that the buoyancy of the bubble could be large enough to overcome the sum of the interfacial adhesion and the weight of the oil. In Figures 6.5 (a) and (b), both of the samples showed mild oleophobicity underwater, with oil CAs of 125° and 113°, respectively. Due to the content of hydrophilic TiO<sub>2</sub> in the 6/4 nano-sponge, oleophobicity showed slightly higher in underwater oil CA. Initially, both of the samples contained tiny air bubbles on their surfaces under water, which were captured by hydrophobic hydrocarbon NPs. Air bubbles were encapsulated by the oil immediately after the contact with heavy oil droplets, due to the positive spreading coefficient,  $S_o$  (+3.8 mN/m for FC-770).

As UV light was irradiated, the bubbles inside of the oil droplets spontaneously grew and dragged the oil droplet upward due to the increased bubble buoyancy. The change in the oil contact radius ( $R_C$ ) and underwater oil CA were monitored during the bubble growth under UV irradiation (Figures 6.5 (c) and (d)). Because changes in  $R_C$  were attributed to receding contact angles<sup>43</sup> and interfacial adhesion, which varies with UV irradiation time on the

nano-sponge, the oil and bubble desorption behaviors with varying underwater oil CA and  $R_C$  can be explained. In the case of the 6/4 nano-sponge, the underwater oil CA slightly increased due to the lateral bubble growth at the beginning of UV irradiation. As the bubble buoyancy increased, the lateral force exerted on the center of the oil droplet gradually increased. The underwater oil CA gradually decreased from  $136^\circ$  to  $115^\circ$ , and discrete contact line movements between the oil and the 6/4 nano-sponge surface were observed, as shown Figure 6.5 (a). When the underwater oil CA was lowered to the receding contact angle (RCA) value, the oil droplet receded with the reduction of  $R_C$ . The underwater oil CA gradually decreased to  $85^\circ$  and abruptly reduced to  $59^\circ$ , before the moment of oil detachment from the surface, leaving only a small amount of oil residue on the surface after 33 hours of UV irradiation. As  $R_C$  was reduced to  $0.65R_C$ , necking of the oil droplet occurred close to the oil-solid interface (Inset in Figure 6.5 (d)). The neck of the oil became unstable and the oil/bubble was pinched off. In contrast, the underwater oil CA for the 10/0 nano-sponge gradually decreased from  $113^\circ$  to  $94^\circ$ , whereas  $R_C$  was almost unchanged, as shown in Figures 6.5 (c) and (d). The RCA for the 10/0 nano-sponge was expected to be smaller than that of the 6/4 nano-sponge, due to different  $\text{TiO}_2$  content. The decrease in the underwater oil CA in the 10/0 nano-sponge was not enough to decrease the RCA. Thus, the necking and pinching off occurred at the oil-bubble interface farthest from the oil-solid interface, leaving most of the oil droplet adhered to the surface. This phenomenon was

attributed to the oleophilic hydrocarbon NPs, which firmly held the oil droplet at the interface with relatively high interfacial adhesion strength over the buoyancy of the oil-encapsulated bubble.

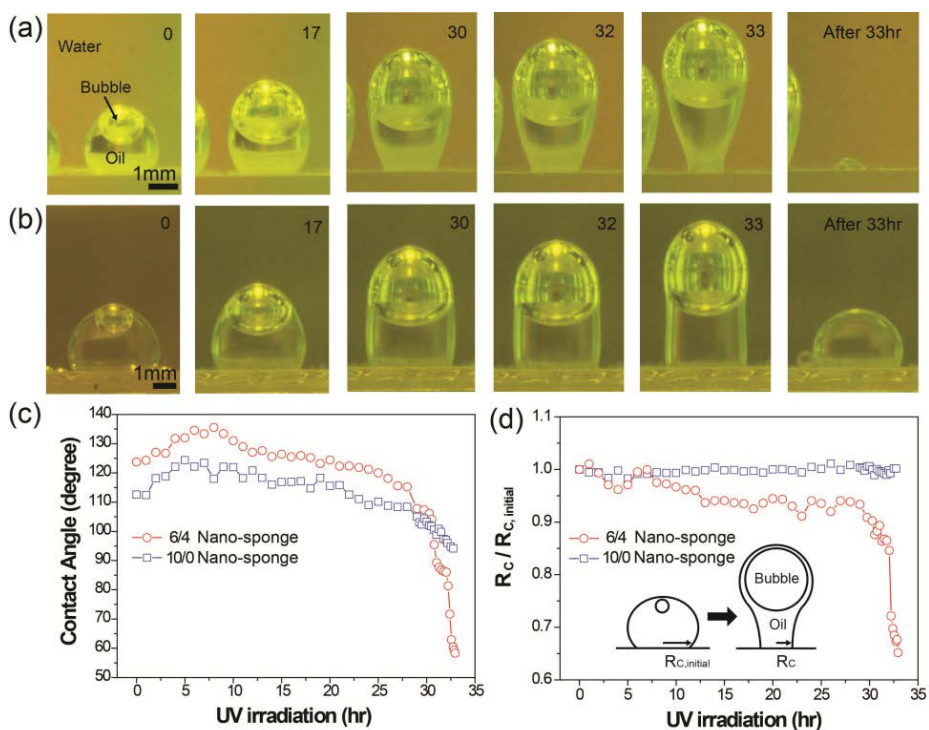


Figure 6.5 Spontaneous growth of bubbles within an oil droplet and oil/bubble release behavior on the surface of the nano-sponge underwater with UV irradiation: A heavy oil (3 M Fluorinert FC-770, density: 1.793 g/ml) release behaviors from the nano-sponges with hydrocarbon/TiO<sub>2</sub> volume ratios of (a) 6/4, (b) 10/0 with UV irradiation for 0, 17, 30, 32, and 33 hr, as well as after 33 hr. (c) Underwater oil CA and (d) ratio of the oil contact radius ( $R_C$ ) to the original oil contact radius ( $R_{C, initial}$ ) for the 6/4 and 10/0 nano-sponges with UV irradiation.

### 6.3.4 Vertical force balance at the oil-solid interface

Regarding the forces acting at the oil-solid interface, the vertical forces of buoyancy, pressure, and surface tension are expressed as follows,

$$F_B = F_{B,bubble} + F_{B,oil} = \rho_w g V_b + \rho_w g V_o - \rho_o g V_o \quad (6.2)$$

$$F_P = \Delta P (\pi R_C^2) = \left( \frac{2\gamma_{ow}}{R} - (\rho_w - \rho_b)gh_1 - (\rho_w - \rho_o)gh_2 \right) \times (\pi R_C^2) \quad (6.3)$$

$$F_S = \gamma_{ow} (2\pi R_C) \sin \theta \quad (6.4)$$

$$F_S = F_P + F_B \quad (6.5)$$

where  $F_B$ ,  $F_{B,bubble}$ ,  $F_{B,oil}$ ,  $F_P$ ,  $F_S$ ,  $\gamma_{ow}$ ,  $R_C$ ,  $\theta$ ,  $\rho_w$ ,  $\rho_o$ ,  $g$ ,  $V_b$ ,  $V_o$ ,  $R$ ,  $h_1$ , and  $h_2$  are the force induced by buoyancy, buoyancy forces of the bubble and oil, pressure force due to excess pressure ( $\Delta P$ ) inside the oil and bubble acting on the contact area, surface tension force, oil-water interfacial tension, oil contact radius, underwater oil CA on solid, the densities of water and oil, acceleration due to gravity, bubble volume, oil volume, radius of curvature at the top of the oil droplet, bubble height, and height between the solid surface and bubble bottom, respectively. The magnitude of the excess pressure across the curved oil-water interface from the Young-Laplace equation is  $2\gamma_{ow}/R$ . If hydrostatic pressure under gravity is applied, the total excess pressure can be taken as the right hand side of equation (6.3).

Because the bubble growth rate was very small, only static forces were considered. Therefore, each force was balanced in equation (6.5), and the surface tension force  $F_S$  and buoyancy force  $F_{B,oil}$  of the oil droplet were responsible for holding the oil on the nano-sponge surface. The pressure,  $F_P$ , and bubble buoyancy,  $F_{B,bubble}$ , forces were responsible for pulling the bubble and oil off from the surface. Each force was non-dimensionalized by dividing the buoyancy force of the oil to illustrate the force exerted for the unit density and unit volume of oil. In the beginning of UV irradiation,  $F_B$  was negative (downward direction) due to large oil density and  $F_{B,bubble}$  was negligible. As buoyancy force of the bubble increased with the growth of bubble while that of the oil was unchanged, the total buoyancy force acting upward increased (became positive) with UV irradiation. Additionally, the surface tension force ( $F_S$ ) of the 6/4 nano-sponge working against the buoyancy and the Laplace pressure forces decreased due to receding-induced  $R_C$  reduction ( $R_B/R_C \approx 2.36$ ), whereas that of the 10/0 nano-sponge was maintained due to contact line pinning ( $R_B/R_C \approx 1.04$ ), as shown in Figures 6.6 (b) and (c). At the moment of detachment,  $F_P$  would be nearly zero due to the negligible neck radius. Consequently, the remaining oil volumes were determined by the magnitude of the surface tension force acting at the oil-solid interface before oil or bubble detachment.

Because the  $R_C$  for both cases were almost the same as the radius of the neck, during all of the bubble growth processes, a modification of Tate's law can be

written as follows<sup>44,45</sup>

$$2\pi R_c \gamma \varphi = \Delta \rho g V \quad (6.6)$$

where the correction factor  $\varphi$  is ratio of the detached mass to the total mass, as a function of  $r/V^{1/3}$ . In general,  $\varphi(r/V^{1/3})$  increased with a decreasing  $r/V^{1/3} < 0.85$ <sup>45</sup>. In this case,  $r$  is the contact radius  $R_c$ , and  $V$  is the oil volume which is constant. As a result, one can consider that the remaining oil volume on the nano-sponge surface depends on the  $R_c$ . Reduction of the  $R_c$  at the detachment corresponded to the reduction of the surface tension force, which resulted in the small amount of the oil residue left on the 6/4 nano-sponge. However, a constant  $R_c$  for the 10/0 nano-sponge was responsible for the constant surface tension force by contact line pinning, which held most of the oil on the 10/0 nano-sponge even after bubble detachment. Overall, this oil detachment was driven not only by the buoyancy force from growing bubbles in oil but also by the reduction of the surface tension force induced by the wetting transition to superoleophobicity, further reducing  $R_c$ .

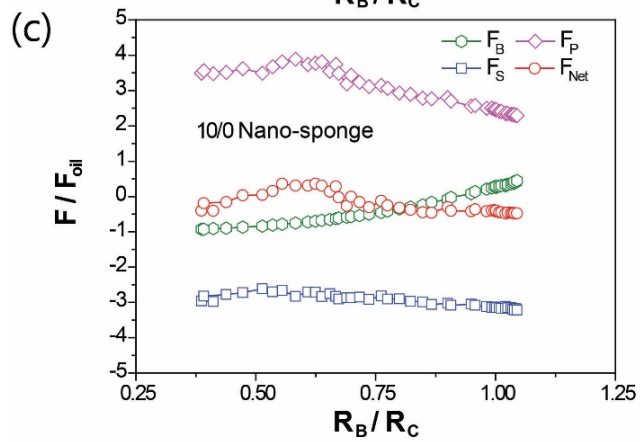
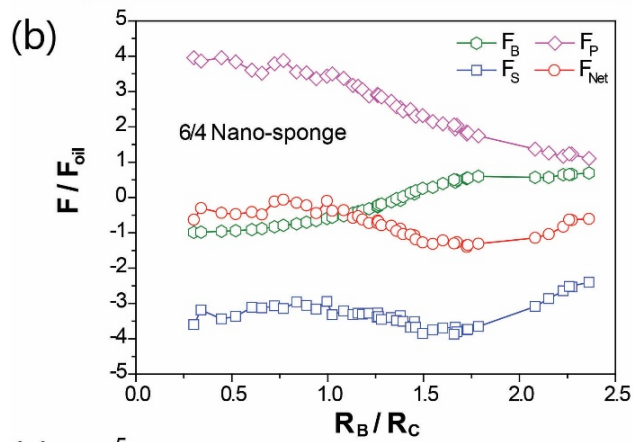
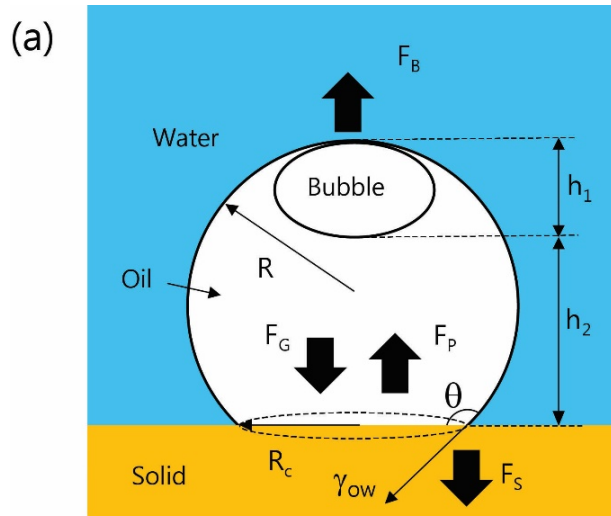


Figure 6.6 Vertical force components of the surface tension ( $F_S$ ), pressure force ( $F_P$ ), and buoyancy ( $F_B$ ) of the oil/bubble at the oil-solid interface underwater during UV irradiation: (a) schematic illustration of each force component. The buoyancy, pressure force, surface tension force, and net force ( $F_{NET}$ ) were non-dimensionalized and plotted as bubble radius ( $R_B$ )/contact radius ( $R_C$ ) for (b) 6/4 and (c) 10/0 nano-sponges.

### 6.3.5 Oil absorption and desorption with NS/p- PDMS

To visualize oil absorption/desorption with the nano-sponge, the 6/4 nano-sponge was coated on the inner and outer surfaces of a porous PDMS sponge<sup>6</sup> by dip coating, which showed superhydrophobicity in air and superoleophilicity underwater. Even after full oil absorption (Figure 6.7 (a)), many bubble nuclei were still observed inside and on the surface of the NS/p-PDMS. As the UV was irradiated, oil was dragged along with the bubbles in the upward direction because the increased buoyancy, which was due to the continuous generation and coarsening of bubbles, exceeded the lowered interfacial adhesion energy between the oil and the nano-sponge by the UV-activated TiO<sub>2</sub>. Then, the oil was finally detached with the bubbles from the NS/p-PDMS, as shown in Figure 6.7 (c). It is worth noting that UV light at the wavelength of 300 nm can penetrate through p-PDMS and NS/p-PDMS (thickness ~5 mm) up to ~50 % and ~8 % of transmittances, respectively. Intrinsic PDMS transmittance and porous structure enabled all TiO<sub>2</sub> NPs within NS/p-PDMS to be activated by UV irradiation.

Because continuous bubble growth was observed on the surface of the nano-sponge, as shown in Figures 6.5 and 6.7, the bubbles were analyzed for their chemical composition. Rising bubbles that are released with oils were collected by covering the transparent container over the oil-absorbed NS/p-PDMS, as shown in Figure 6.7 (d). As the duration of UV irradiation increased, the

number of desorbed oil/bubbles increased; subsequently, the number of bubbles trapped at the bubble/oil collecting surface increased. The collected bubbles were analyzed using mass spectroscopy, confirming that the bubbles were composed of oxygen (17.3%) and nitrogen (82.7%), similar to the contents in air (Figure 6.7 (e)). Through the control experiment using deaerated DI water, it was found that the bubble source originated from dissolved oxygen and nitrogen in the water, indicating that bubble growth was a diffusion-controlled phenomenon. Due to the pre-existing air bubble nuclei in the oil droplets, bubble growth could have occurred by molecular diffusion from the DI water to the air bubble, even at low levels of gas supersaturation in the water<sup>46</sup>. Furthermore, it has been discussed that oil having high gas solubility acts as a gas storage trap; therefore, the mass transfer of oxygen or nitrogen molecules could be enhanced through the oil layer between the air bubble and water phases<sup>47,48</sup>. Thus, there is an increased driving force for dissolved air to diffuse through the oil. The bubbles in oil can grow larger due to lower oil surface tensions (organic liquids including oils: 10~30 mN/m) than the surface tension of water (72.8 mN/m). It is concluded that the mechanism of oil desorption is a combined effect of air bubble growth, wetting transition, and PCO by the UV-responsive TiO<sub>2</sub>, as shown in Figure 6.8.

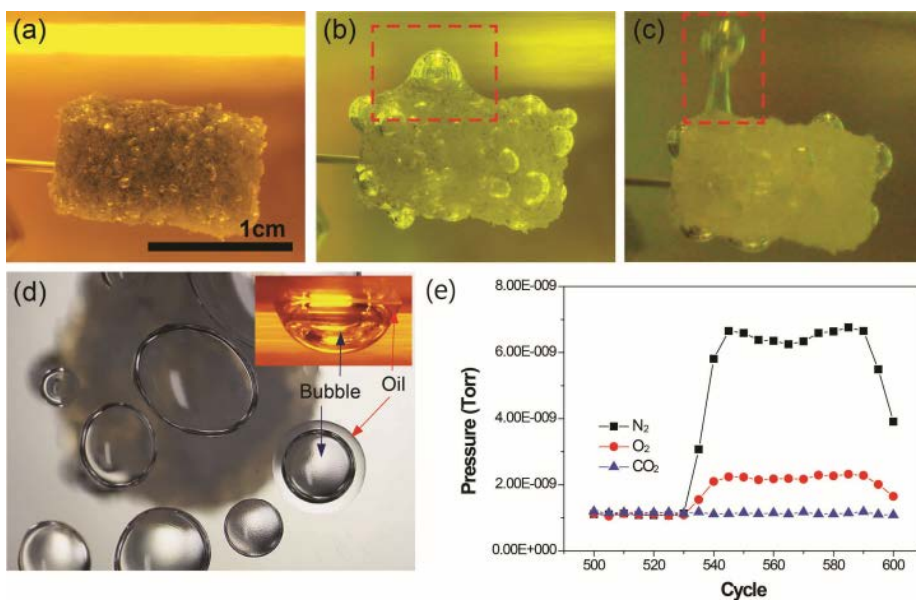


Figure 6.7 Spontaneous oil (n-hexane, dyed in blue) absorption/desorption of a 6/4 NS/p-PDMS during UV irradiation, and the origin of bubble growth with the oil desorption mechanism. Oil desorption with UV irradiation time (a) 0 hr and (b) 8 hr, respectively. (c) Snapshot of oil/bubble release (~ 24 hr). (d) Top view of the collected oil/bubbles. The inset shows the side view of the collected oil/bubble. (e) Mass spectroscopy analysis of collected gas bubbles.

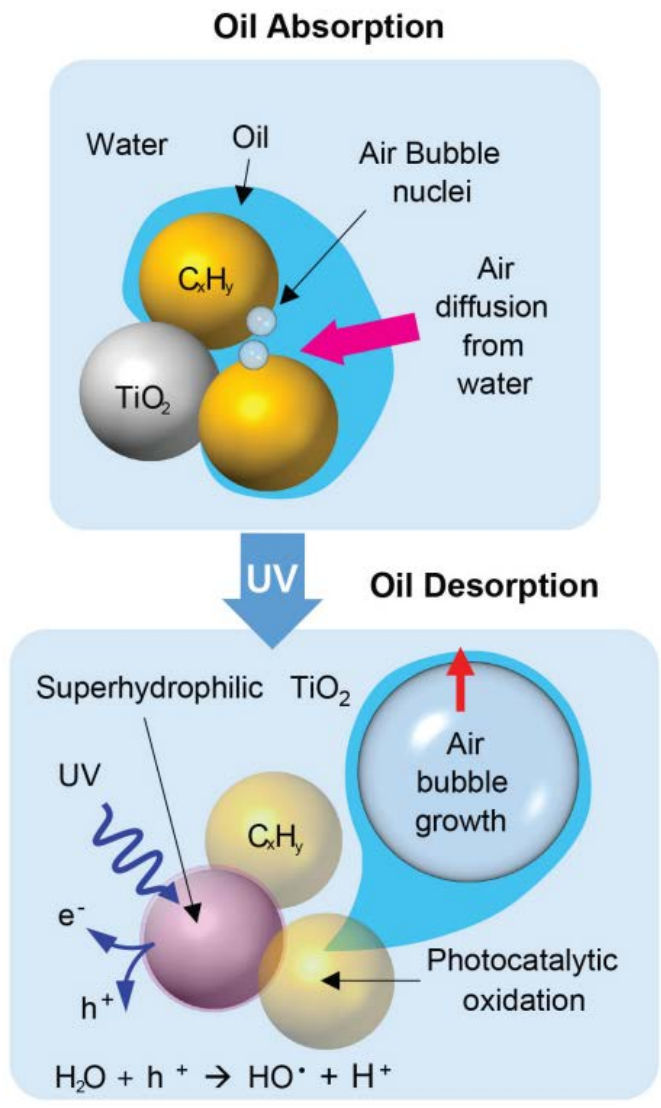


Figure 6.8 Mechanism of bubble growth and oil desorption with UV-responsive TiO<sub>2</sub>

### 6.3.6 Recyclable oil absorption and desorption.

To function as a promising smart material for oil absorption/desorption, the oil absorption capacity and recyclability are the key requirements for practical oil clean-up applications. Thus, the absorption capacity and recyclability of a 6/4 NS/p-PDMS and a p-PDMS were compared using crude oil and different desorption methods of UV/bubbling, only bubbling, and simple squeezing, as shown in Figure 6.10. There have been several reports showing that gas bubbles remove contaminants, such as chemicals, powders, and oils, with high efficiency by several gas flotation techniques<sup>49</sup>. Thus, air bubbling was externally supplied to the 6/4 NS/p-PDMS during UV irradiation, resulting in a similar effect to spontaneous bubble formation and growth from dissolved air in water, but with an enhanced oil desorption rate. Figure 6.9 shows the typical sequence for crude oil absorption and desorption by UV/bubbling: air-filled NS/p-PDMS before oil absorption, oil-filled NS/p-PDMS, desorption of oil, and water-filled NS/p-PDMS after full desorption. During the recycling test, the oil absorption capacity and oil desorption efficiency were determined by weighing the sponges and were calculated as follows:

$$\text{Absorption capacity (\%)} = \frac{W - W_0}{W_0} \times 100(\%) \quad (6.7)$$

$$\text{Desorption efficiency (\%)} = \frac{W_D}{W_A} \times 100 (\%) \quad (6.8)$$

where  $W_0$  and  $W$  are the weight of the sponges before and after oil absorption,

respectively.  $W_A$  is weight of absorbed oil, and  $W_D$  is weight of desorbed oil.

After crude oil desorption, the NS/p-PDMS and p-PDMS were dried in a vacuum for several hours to evaporate the infiltrated water and residue of crude oil, respectively. The oil absorption capacity of the NS/p-PDMS was slightly higher due to the increased porosity of the hydrocarbon and TiO<sub>2</sub> NPs, compared with that of the p-PDMS (459% and 430%, respectively). However, the oil absorption capacity of the NS/p-PDMS was maintained at 459±4% after 10 cycles, whereas that of the p-PDMS gradually reduced from 430% (441%) to 361% (424%) by squeezing (bubbling) (Figure 6.10 (a)). Regarding the oil desorption efficiency, with only UV irradiation on the 6/4 NS/p-PDMS, 65% of oil was desorbed for 48 hours due to slow bubble growth. However, with only air bubbling without UV irradiation, 91±2% of absorbed oil was desorbed from the p-PDMS sponge within 1 hour while the oil residues were continuously increased with the number of cycling. The oil desorption by squeezing was 80±3%. According to other researchers, p-PDMS maintained their absorption capacity during recycling tests by squeezing. However, they cleaned the p-PDMS to remove the oil residues using other chemical solvents such as ethanol<sup>6</sup>. This rinsing process itself caused secondary contamination and required effort to dispose of the chemicals. With together of UV/bubbling, the oil residues could be mostly removed and desorption efficiency was as high as 98±1% in the 6/4 NS/p-PDMS sponge as shown in Figure 6.10 (b). As discussed earlier, wetting transition under UV irradiation would occurred at the

interface between the absorbed oil and the NS/p-PDMS surface, which resulted in almost perfect desorption even after 10 cycle tests. As shown in Figure 6.11 (a), crude oil slicks continuously appeared from the p-PDMS (black color, containing greater than 19% oil) on the water surface even after squeezing and subsequent drying in a vacuum. On the other hand, the NS/p-PDMS sponge showed no slick due to almost complete desorption of the oil during UV/bubbling (yellow color after water evaporation, Figure 6.11 (b)). The underwater oil wettability on the NS/p-PDMS was altered to superoleophobicity as the oil was replaced with infiltrated water during UV/bubbling (Figure 6.11 (b)). For the reuse of the sponge, the NS/p-PDMS sponge restored its original wettability from underwater superoleophobicity to oleophilicity with the sequential process of evaporating the infiltrated water and storage in the dark. Therefore, the oil desorption method of UV triggered wetting transition, when using with bubbling together, had a superior capability for oil clean-up and recyclability without secondary contamination, compared with simple squeezing of the p-PDMS sponge.

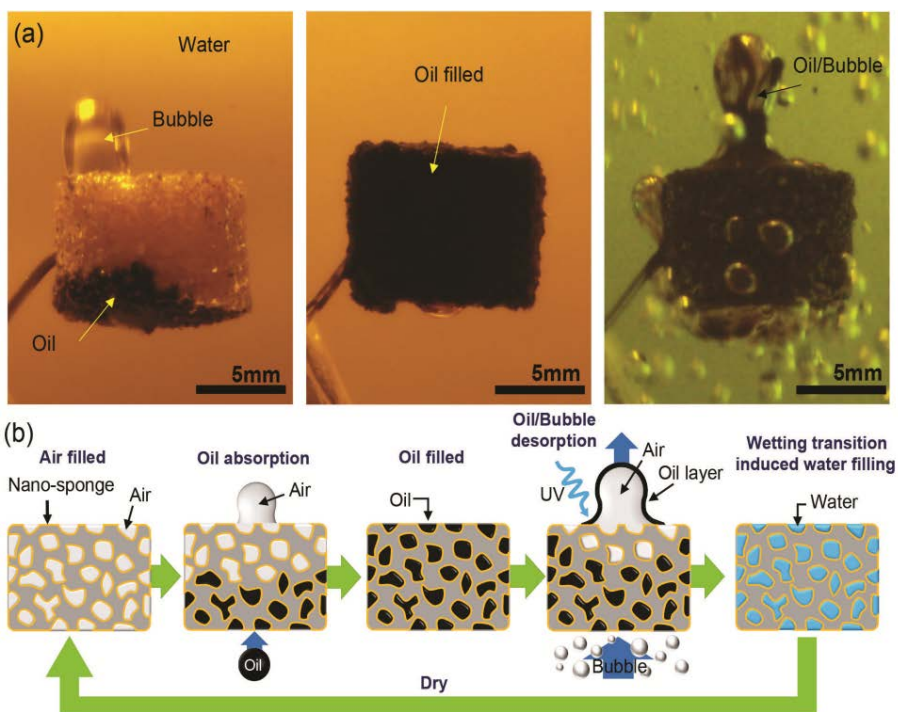


Figure 6.9 (a) Underwater crude oil absorption of the 6/4 NS/p-PDMS, fully absorbed state, and oil desorption with air bubble flow/UV irradiation. (b) A schematic procedure of oil absorption and desorption with UV-responsive wettability and air bubble flow

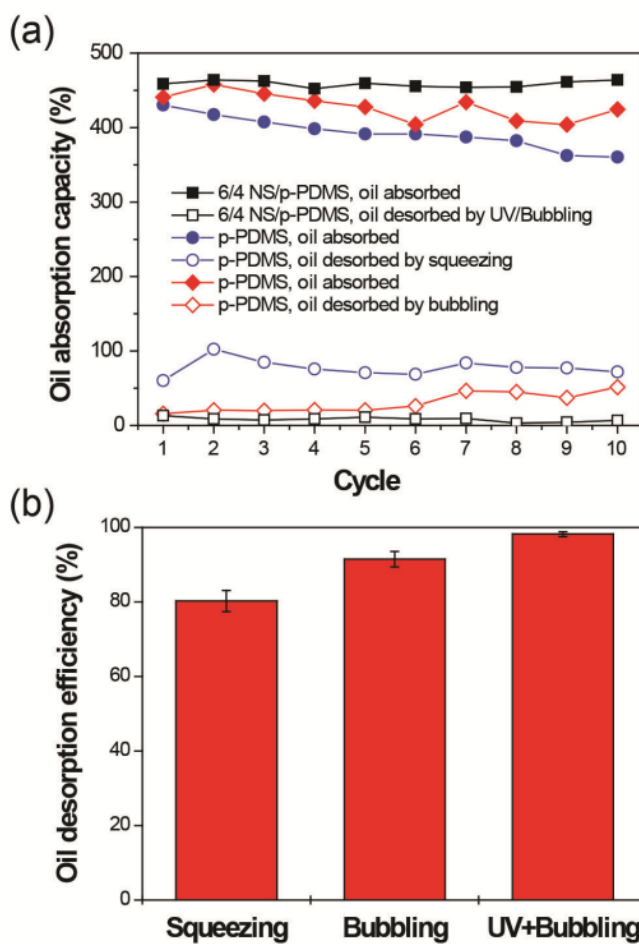
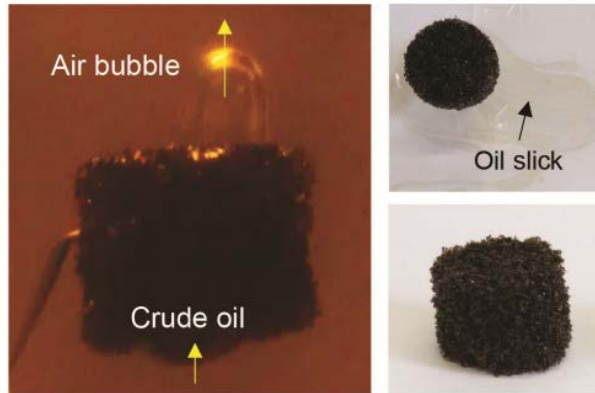


Figure 6.10 (a) Oil absorption/desorption capacities and recyclabilities of the NS/p-PDMS (desorption by UV/bubbling) vs. a p-PDMS (desorption by squeezing or bubbling). (b) Oil desorption efficiency: bubbling and UV irradiation on the NS/p-PDMS sponge vs. squeezing the p-PDMS for oil desorption

(a) Squeezed p-PDMS



(b) UV/Bubbling – 6/4 NS/p-PDMS



Figure 6.11 (a) Underwater oleophilic nature of the p-PDMS after squeezing. (b) Underwater oleophobic nature of the 6/4 NS/p-PDMS after UV/bubbling

## 6.4 Conclusion

A smart approach to control the oil absorption/desorption of the nano-sponge has been demonstrated by the simple mixing of a hydrophobic hydrocarbon and photo-responsive, hydrophilic TiO<sub>2</sub> NPs. The role of the hydrophobic nature of the hydrocarbon NPs was to selectively absorb only the oil from water. Then, a UV-induced wetting transition by TiO<sub>2</sub> NPs from a mild oleophilic state to an underwater superoleophobic state released the absorbed oil from the nano-sponge with UV irradiation. This was further demonstrated by the NS/p-PDMS with high oil absorption/desorption efficiency without the occurrence of secondary pollution. Because materials for smart control of oil absorption/desorption are not limited only to hydrocarbons and TiO<sub>2</sub> NPs, any type of mixture of hydrophobic and hydrophilic materials with photo-switchable wettability could be used to realize oil-water separation and oil spill clean-up. Furthermore, nano-sponge is expected to separate the various type of emulsions, due to the wide range of tunable wettability with several tens of nanometer scale pores for practical application for emulsion separation.

## 6.5 References

1. M.O. Adebajo, R.L. Frost, J.T. Kloprogge, O. Carmody, S. Kokot, *J. Porous Mater.* **10**, 159 (2003).
2. N.P. Ventikos, E. Vergetis, H.N. Psarftis, G. Triantafyllou, *J. Hazard. Mater.* **107**, 51 (2004).
3. M. Fingas, *The Basics of Oil Spill Cleanup*. Ch. 7 (CRC Press, 2012).
4. H.-M. Choi, R.M. Cloud, *Environ. Sci. Technol.* **26**, 772 (1992).
5. J. Yuan, X. Liu, O. Akbulut, J. Hu, S. Suib, J. Kong, F. Stellacci, *Nat. Nanotechnol.* **3**, 332 (2008).
6. S.-J. Choi, T.-H. Kwon, H. Im, D.-I. Moon, D.J. Baek, M.-L. Seol, J.P. Duarte, Y.-K. Choi, *ACS Appl. Mater. Interfaces* **3**, 4552 (2011).
7. Q. Zhu, Q. Pan, F. Liu, *J. Phys. Chem. C* **115**, 17464 (2011).
8. X. Gui, H. Li, K. Wang, J. Wei, Y. Jia, Z. Li, L. Fan, A. Cao, H. Zhu, D. Wu, *Acta Mater.* **59**, 4798 (2011).
9. X. Gui, J. Wei, K. Wang, A. Cao, H. Zhu, Y. Jia, Q. Shu, D. Wu, *Adv. Mater.* **22**, 617 (2010).
10. J. Zhao, W. Ren, H.-M. Cheng, *J. Mater. Chem.* **22**, 20197 (2012).
11. W. Dai, S.J. Kim, W.-K. Seong, S.H. Kim, K.-R. Lee, H.-Y. Kim, M.-W. Moon, *Sci. Rep.* **3**, 2524 (2013).
12. M. Liu, S. Wang, Z. Wei, Y. Song, L. Jiang, *Adv. Mater.* **21**, 665 (2009).
13. Z. Xue, S. Wang, L. Lin, L. Chen, M. Liu, L. Feng, L. Jiang, *Adv. Mater.* **23**, 4270 (2011).
14. L. Zhang, Y. Zhong, D. Cha, P. Wang, *Sci. Rep.* **3**, 2326 (2013).
15. A.K. Kota, G. Kwon, W. Choi, J.M. Mabry, A. Tuteja, *Nat. Commun.* **3**, 1025 (2012).
16. J. Yang, Z. Zhang, X. Xu, X. Zhu, X. Men, X. Zhou, *J. Mater. Chem.* **22**, 2834 (2012).
17. M. Tao, L. Xue, F. Liu, L. Jiang, *Adv. Mater.* **26**, 2943 (2014).

18. Y. Xiang, F. Liu, L. Xue, *J. Membr. Sci.* **476**, 321 (2015).
19. X. Feng, L. Feng, M. Jin, J. Zhai, L. Jiang, D. Zhu, *J. Am. Chem. Soc.* **126**, 62 (2004).
20. W. Zhu, X. Feng, L. Feng, L. Jiang, *Chem. Commun.* 2753 (2006).
21. J. Zhang, X. Lu, W. Huang, Y. Han, *Macromol. Rapid Commun.* **26**, 477 (2005).
22. F. Zhou, W.T.S. Huck, *Chem. Commun.* 5999 (2005).
23. J. Lahann, S. Mitragotri, T.-N. Tran, H. Kaido, J. Sundaram, I. S. Choi, S. Hoffer, G.A. Somorjai, R. Langer, *Science* **299**, 371 (2003).
24. A. Grigoryev, I. Tokarev, K.G. Kornev, I. Luzinov, S. Minko, *J. Am. Chem. Soc.* **134**, 12916 (2012).
25. B. Xue, L. Gao, Y. Hou, Z. Liu, L. Jiang, *Adv. Mater.* **25**, 273 (2013).
26. L. Zhang, Z. Zhang, P. Wang, *NPG Asia Mater.* **4**, e8 (2012).
27. Y. Xiang, J. Shen, Y. Wang, F. Liu, L. Xue, *RSC Adv.* **5**, 23530 (2015).
28. R. Wang, K. Hashimoto, A. Fujishima, M. Chikuni, E. Kojima, A. Kitamura, M. Shimohigoshi, T. Watanabe, *Nature* **388**, 431 (1997).
29. X. Feng, J. Zhai, L. Jiang, *Angew. Chem. Int. Ed.* **44**, 5115 (2005).
30. Y. Sawai, S. Nishimoto, Y. Kameshima, E. Fujii, M. Miyake, *Langmuir* **29**, 6784 (2013).
31. C. Gao, Z. Sun, K. Li, Y. Chen, Y. Cao, S. Zhang, L. Feng, *Energy Environ. Sci.* **6**, 1147 (2013).
32. E. Balaur, J.M. Macak, L. Taveira, P. Schmuki, *Electrochem. Commun.* **7**, 1066 (2005).
33. M. Kettunen, R.J. Silvennoinen, N. Houbenov, A. Nykänen, J. Ruokolainen, J. Sainio, V. Pore, M. Kemell, M. Ankerfors, T. Lindström, M. Ritala, R.H.A. Ras, O. Ikkala, *Adv. Funct. Mater.* **21**, 510 (2011).
34. A. Dupré, P. Dupré, *Théorie Mécanique de la Chaleur* Ch. 9 (Gauthier-Villars, 1869).
35. A.W. Adamson, A.P. Gast, *Physical Chemistry of Surfaces* Ch. 10 (John

- Wiley & Sons, 1997).
36. E. Bormashenko, *Colloid. Polym. Sci.* **291**, 339 (2013).
  37. M. Tedetti, R. Sempéré, *Photochem. Photobiol.* **82**, 389 (2006).
  38. A. Fujishima, T.N. Rao, D.A. Tryk, *J. Photochem. Photobiol. C: Photochem. Rev.* **1**, 1 (2000).
  39. A. Fujishima, X. Zhang, D.A. Tryk, *Surf. Sci. Rep.* **63**, 515 (2008).
  40. J. Mo, Y. Zhang, Q. Xu, J.J. Lamson, R. Zhao, *Atmos. Environ.* **43**, 2229 (2009).
  41. N. Ohtsu, N. Masahashi, Y. Mizukoshi, K. Wagatsuma, *Langmuir* **25**, 11586 (2009).
  42. M. Xing, F. Shen, B. Qiu, J. Zhang, *Sci. Rep.* **4**, 6341 (2014).
  43. H. Chen, T. Tang, A. Amirfazli, *Soft Matter* **10**, 2503 (2014).
  44. W. D. Harkins, F.E. Brown, *J. Am. Chem. Soc.* **41**, 499 (1919).
  45. J. C. Earnshaw, E.G. Johnson, B.J. Carroll, P. J. Doyle, *J. Colloid Interface Sci.* **177**, 150 (1996).
  46. S.F. Jones, G.M. Evans, K.P. Galvin, *Adv. Colloid Interface Sci.* **80**, 27 (1999).
  47. R. Battino, H.L. Clever, *Chem. Rev.* **66**, 395 (1966).
  48. E. Dumont, H. Delmas, *Chem. Eng. Process.* **42**, 419 (2003).
  49. J. Rubio, M.L. Souza, R.W. Smith, *Miner. Eng.* **15**, 139 (2002).
  50. B.-I. Park, H. Jie, B.-G. Song, K.-M. Kang, J.-K. Park, S.-H. Cho, *Res. Chem. Intermed.* **40**, 115 (2014).
  51. J.S. Kuo, L. Ng, G.S. Yen, R.M. Lorenz, P.G. Schiro, J.S. Edgar, Y. Zhao, D.S.W. Lim, P.B. Allen, G.D.M. Jeffries, D.T. Chium, *Lap Chip* **9**, 870 (2009).

## **Appendix II. Microtexture development during equibiaxial tensile deformation in monolithic and dual phase steels**

### **7.1 Microstructure and deformation behavior in DP steel**

Modern high strength steels have been developed for the automotive industry for the purpose of reducing the weight of the car body, which improves fuel efficiency and satisfies the consumer's increasing demand for safer and more comfortable vehicles. Among the high strength steels, generally, dual phase (DP) steels are low-carbon low-alloy materials with 5 ~ 30 vol.% hard martensite in a ductile ferrite matrix. As they combine high strength and good formability at low production costs, they are also widely used for recent automotive applications<sup>1-7</sup>. In general, the martensite fraction in low-carbon DP steel could be controlled by the deformation of ferrite–pearlite steel and a subsequent intercritical annealing condition. During deformation, DP steel shows complex inhomogeneous deformation behavior, which is given by the presence of different microstructural constituents. The complex deformation behavior might act as a drawback to broad application of DP steel. To ensure the reliable application of DP steel, it is important to understand the influence of the complex deformation behavior on the microstructure change. Therefore, there have been many researches to analyze microstructure changes of DP steel with

respect to subgrain texture evolution during deformation<sup>8-17</sup>.

It is well known that the mechanical properties of polycrystalline materials during plastic deformation are strongly affected by their initial microstructures and microstructural changes, such as the rotation of the crystallographic orientations of individual grains, the subgrain evolution, or the quantity and distribution of dislocations including both geometrically necessary dislocations (GNDs) and statistically stored dislocations (SSDs). Finally, the macroscopic mechanical behavior of materials such as DP steel was governed by the combination of microstructural changes and their micromechanical responses, which were influenced by grain or phase interactions during deformation. Lebensohn *et al.* simulated the microstructure change and the subgrain evolution in polycrystalline copper during uniaxial tensile deformation and the results were compared with the experimentally measured data<sup>18</sup>. Dillien *et al.* measured lattice curvature in ferrite of DP steel during cold rolling<sup>19</sup>. It was revealed that a strong lattice curvature develops predominantly around martensite grains and this leads to high orientation gradient in ferrite grain adjacent to martensite grains. As for the GNDs<sup>20-22</sup>, recently, the accumulated GND density in DP steel was estimated based on the misorientation distribution with the help of a high-resolution electron backscatter diffraction (HR-EBSD)<sup>23,24</sup>. However, most of works were related to GND formation in DP steel, which was originated from the volume expansion during austenite-to-martensite transformation without further deformation.

In this study, in order to understand the subgrain texture and microstructural evolution in individual ferrite grains in interstitial-free (IF) and DP steel sheets with various martensitic fractions during plastic deformation HREBSD measurement on a special deformation stage for equibiaxial tension was carried out inside a scanning electron microscope chamber. The micromechanical effect of hard martensite islands on adjacent ferrite grains in DP steels was analyzed by comparing the microstructural changes in the IF and DP steels. The distribution of GND and the height distribution inside ferrite grains near martensite islands, as well as the overall texture evolution for each deformation step, were observed through high resolution transmission electron microscopy (HRTEM) and atomic force microscopy (AFM), respectively. From the measured microstructural and geometrical changes in the IF and DP steels the effect of hard martensite on the microstructure of the steels during plastic deformation was investigated and is discussed.

## 7.2 Experimental procedure

### 7.2.1. Equi-biaxial tensile deformation and microstructure

A quantitative measurement of orientation changes during stepwise biaxial tensile deformation of individual ferrite grains and grain-aggregates in IF and DP steels was attempted by combining EBSD and a specially designed mechanical device as shown in Figure 7.1. The device was installed in the SEM chamber and operated so as to develop the equi-biaxial tensile mode at the center-top part of the sheet-type specimens as the screw rotated up, as shown in Figure 7.1 (b). Figures 7.1 (c) and (d) are digital images of the specimen on the device before and after equi-biaxial tensile deformation, respectively. A lubricant between the hemisphere-shaped cap and specimen was used to decrease the frictional stress between the specimen and the screw. A disk-shaped specimen with a diameter of 16mm was prepared with a wire-cutting method, as shown in Figure 7.1 (a). The specimen was mechanically polished down to a thickness of 300 $\mu\text{m}$  by using a diamond suspension. Then, a final surface polishing by colloidal silica and an Ar<sup>+</sup> plasma cleaning were conducted for high quality digital imaging.

To trace the microstructure of the same area on the specimen during stepwise equi-biaxial tensile deformation, four rectangular micro-indentation marks were placed on the specimen surface before loading, as shown in Figure 7.1 (a). From the shape change of the rectangular indentation marks during deformation,

it was confirmed that the equi-biaxial tensile deformation was applied. Macroscopic strains at each deformation step were obtained by measuring the relative displacement of the indentation marks along both horizontal and vertical directions in the SEM images. The tensile strain was measured to be up to about 13 % along one direction.

All experiments were carried out in a scanning electron microscope (JEOL, JSM-6500F) equipped with a field emission gun. The crystallographic orientation changes of strained grains were analyzed by an EBSD system (INCA crystal, Oxford and HKL channel 5). The accelerating voltage and probe current were set at 20kV and 4nA, respectively. The band detection numbers and resolution of the Hough transformation were also maintained as constants at 5 and 50, respectively, for consistent EBSD measuring conditions. It is known that the appropriate spatial resolution, which is simply the distance between two adjacent pixels, should be chosen according to the grain size<sup>25</sup>. Given ferrite grain sizes of 17 $\mu$ m and 6.5 $\mu$ m in IF and DP steels, respectively, the spatial resolutions used were 1 $\mu$ m and 0.1 $\mu$ m respectively.

To investigate the thickness directional displacement in ferrite grains near martensite islands after equi-biaxial tensile deformation, atomic force microscopy (PSIA, XE-150 model) was used. From the measured surface morphology, the distribution of thickness directional strain was evaluated in the ferrite phase in DP steels. After EBSD measurements of deformed DP steel, the

dislocation structure in ferrite adjacent to martensite islands was observed by high resolution TEM (JEOL, 3000F). For the TEM observation of the special ferrite region, a cross-sectional sample was fabricated via a focused ion beam (FIB, Nova NanoLab 200) equipped with a Schottky field emission gun column, Ga<sup>+</sup> ion beam column, Pt gas injection system, and Omniprobe internal micromanipulator. The damage by the Ga<sup>+</sup> ion beam during FIB sample preparation was reduced by Ar<sup>+</sup> plasma cleaning.

#### 7.2.2. Materials and determination of martensite fraction.

The present investigation was carried out for IF and DP steels, whose chemical compositions are listed in Table 1. While IF steel consists of only a monolithic ferrite phase, DP steels consist of soft ferrite and hard martensite. The proportion of martensite in DP steels was controlled by the deformation of the initial ferrite–pearlite steel and subsequent intercritical annealing treatments at the temperatures of 720°C, 760°C, and 850°C for 30 minutes and these treatments resulted in area fractions of 7%, 18%, and 27%, respectively. The above values were determined through a phase analysis for EBSD patterns (EBSPs) of the specimens. A conventional tool for phase volume fraction measurement is diffraction profile analysis using an X-ray or neutron beam<sup>26,27</sup>. This method is based on the difference in lattice symmetry. However, this method tends to fail when attempting to discriminate between various phases of steels that form by the decomposition of austenite, because those phases,

such as ferrite, bainite, and martensite, have almost identical lattice structures in most cases. Recently, it has been shown that the quantitative measure of the EBSP quality is very useful for mapping microstructures<sup>28-30</sup>. Since the pattern quality is sensitive to lattice defects and surface topology, a map constructed with it shows detailed features of the microstructure, such as the boundaries. Also, because different phases generally have different diffraction intensities, the map can also present phase contrast. The phases that form at low temperatures, such as bainite and martensite, usually have higher dislocation contents, which lead to degraded EBSPs with lower pattern quality. Thus in this study, the initial area fraction and position of martensite in DP steels were determined based on EBSD band contrast (BC) images using the subset selection function in an HKL channel 5 system, where BC quantifies the pattern quality. Figure 7.2 shows the BC image map and profile, which was scaled to be the byte range 0 to 255, for the DP steel with 18% martensite area fraction as an example. For grain identification and subsequent grain averaging of the BC, the misorientation angle for the grain boundary definition was set to 5°. In Figure 7.2 (b), the BC histogram indicates that the martensite phase has original BC values ranging from 20 to 120. Accordingly grains with grain average BC below 98 were assigned to martensite whereas grains with BC over 98 were assigned to be ferrite.

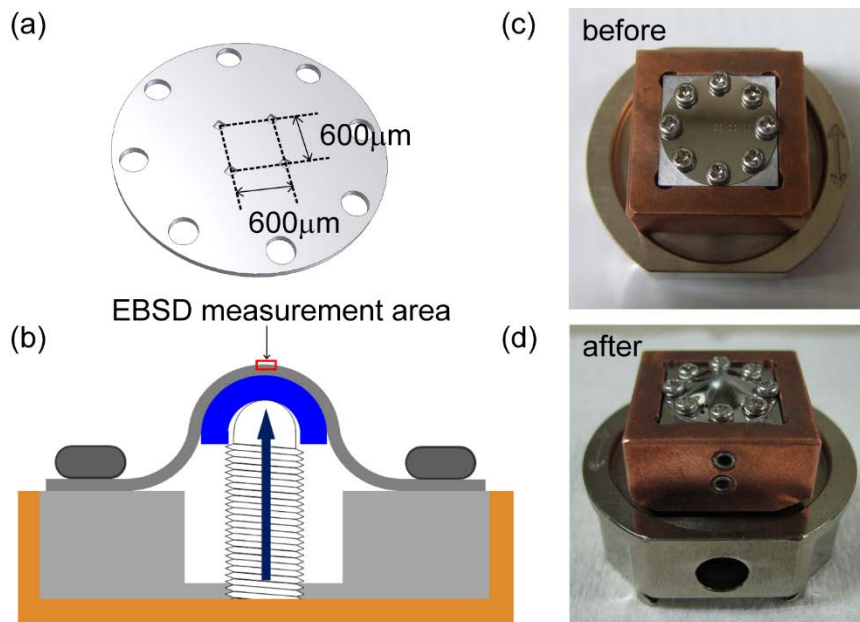


Figure 7.1 Schematic diagram and digital images of equi-biaxial tensile deformation device for EBSD measurement: (a) Sample shape for equi-biaxial tensile deformation. (b) Schematic diagram of equi-biaxial tensile deformation device controlled by rotation of screw. Digital images of equi-biaxial tensile deformation device (c) before and (d) after deformation

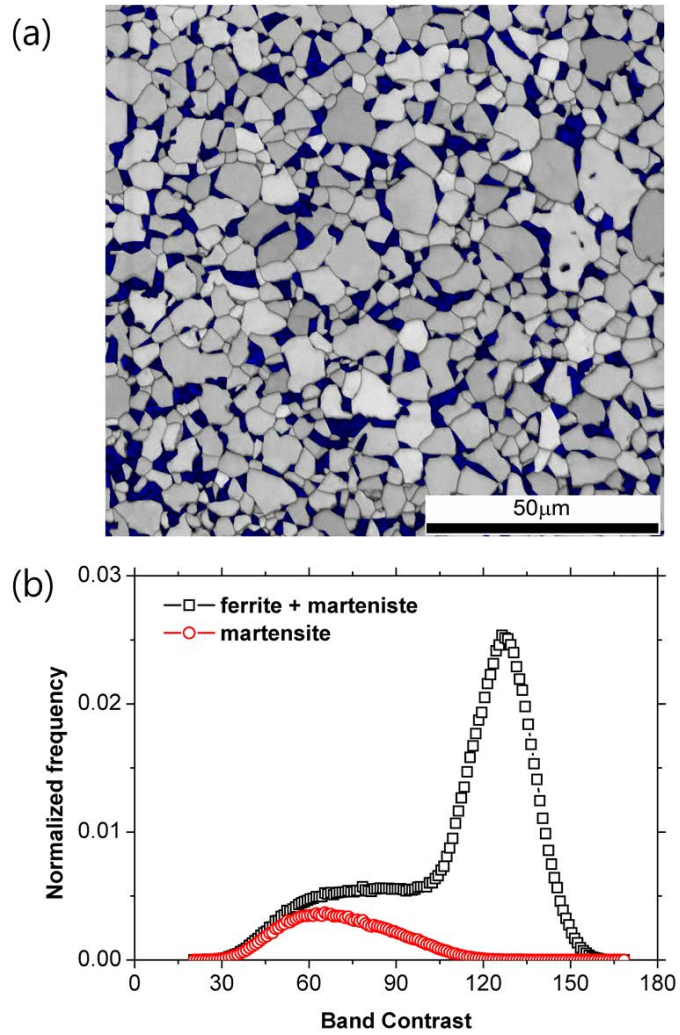


Figure 7.2 (a) Band contrast image and (b) histogram for martensite selection in DP steel. Blue color in (a) indicates martensite phase

## 7.3 Results and Discussion

### 7.3.1 Microtexture development in IF and DP steels

Equi-biaxial tensile deformation for IF and DP steels with martensite area fractions of 0%, 7%, 18%, and 27% was carried out in the SEM chamber using the device shown in Figure 7.1. For the deformation steps corresponding to the horizontal directional strains of 0%, 5%, 9%, and 13%, the orientation images at the center top of the sheet specimens were measured by EBSD. We confirmed that the strain developed at the center top of the specimen was almost equi-biaxial strain based on the finding that the rectangular indentation marks on the specimen surface remained nearly rectangular. The measured orientation image maps from the surface normal direction (ND), overlaid onto the BC image maps, are shown in Figure 7.3. For the zero strain case (before equi-biaxial tensile deformation), the ferrite and martensite in the DP steels could be identified from the BC image maps, as shown in Figures 7.2 and 7.3. It is clear that martensite islands (dark area) are well distributed at triple junctions of ferrite grain boundaries in DP steels.

In order to observe the effect of the martensite islands on texture change in ferrite phase, although the initial crystallographic orientations in IF and DP steels are not similar due to the previous different thermomechanical treatments, IF and DP steels with various martensite fractions were compared. In Figure 7.3, the red, green, and blue colors represent the  $\langle 001 \rangle$ ,  $\langle 101 \rangle$ , and  $\langle 111 \rangle$

crystallographic directions parallel to the normal direction (ND) of the specimen, respectively. It was evident that the area of the green region, which is close to  $\langle 101 \rangle // \text{ND}$ , decreases as the biaxial strain increases. This means that  $\langle 101 \rangle // \text{ND}$  rotates towards  $\langle 111 \rangle // \text{ND}$  or  $\langle 001 \rangle // \text{ND}$  with the biaxial strain. This is as expected because equi-biaxial stretch is similar to compression and the stable end orientations for bcc materials deforming in compression are  $\langle 001 \rangle // \text{ND}$  and  $\langle 111 \rangle // \text{ND}$ . The tendency of orientations between  $\langle 101 \rangle // \text{ND}$  and  $\langle 112 \rangle // \text{ND}$  to split and be unstable was noted by Katoh and Hutchinson, who also noted its importance for subsequent annealing<sup>31,32</sup>. In addition to the overall texture change, the post-deformation images of the IF and DP steels clearly indicate the development of intragranular misorientations in terms of noticeable color gradation inside the ferrite grains. Note that the dark area broadens as the deformation progresses in DP steels. This indicates that the BC values of ferrite regions adjacent to martensite islands were drastically reduced as the biaxial deformation increased. This tendency was stronger in the DP steel with larger martensite fractions and was rarely observed in IF steel. In this study, we investigated why differences in microstructural change occur in IF and DP steels during equi-biaxial deformation.

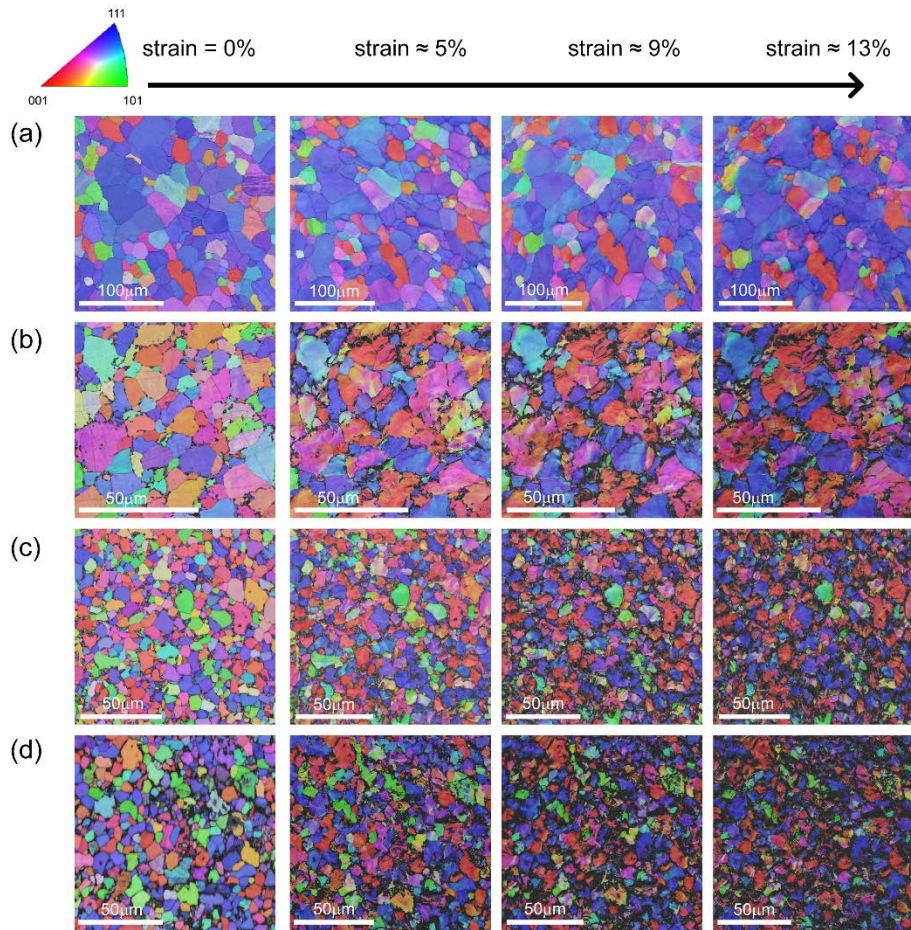


Figure 7.3 EBSD orientation maps of IF and DP steels with martensite area fractions of (a) 0%, (b) 7%, (c) 18% and (d) 27% during equi-biaxial tensile deformation

### 7.3.2 Visco-Plastic Self-Consistent (VPSC) model: texture prediction

In order to investigate the overall texture change during equi-biaxial tensile deformation, a visco-plastic self-consistent (VPSC) model was used. The self-consistent approximation is one of the commonly used methods for estimating the macroscopic behavior of polycrystalline aggregates. However, since this method is based on a mean-field approach<sup>33-35</sup>, the actual micromechanical fields and orientation changes that develop inside the grains of a polycrystalline material may vary from the predictions. In this study, a velocity gradient of equi-biaxial tension in the plane of material with random BCC grains was applied. Version 7c of the Los Alamos VPSC code was employed<sup>36</sup>. The slip systems were assumed to be  $\{110\}\langle 111\rangle$  and  $\{112\}\langle 111\rangle$ . For crystallographic slip, a standard rate-dependent plastic slip law<sup>37</sup> was employed in the VPSC code.

$$\dot{\epsilon}_{ij}(\bar{x}) = \dot{\gamma}_0 \sum_s m_{ij}^s \left( \frac{m_{kl}^s \sigma_{kl}(\bar{x})}{\tau_0^s} \right)^n \quad (7.1)$$

where  $m_{ij}^s$ ,  $\dot{\gamma}_0$ ,  $\dot{\epsilon}_{ij}(\bar{x})$  and  $\sigma_{kl}(\bar{x})$  are the symmetric Schmid tensor associated with slip system (s), a normalization factor, the deviatoric strain rate and stress, respectively. The rate-sensitivity exponent ( $n$ ) and the initial shear stress ( $\tau_0^s$ ) resolved onto the slip plane were assumed to be 20 and 2 MPa, respectively.

The simulated texture at a von Mises equivalent strain of 0.75 is shown in Figure 7.4 as ND inverse pole figures. By partitioning grains into two regions divided by a line connecting  $\langle 113 \rangle$  and  $\langle 304 \rangle$ , two different stable orientations for equi-biaxial tensile deformation were found. Those colored red tended to rotate towards  $\langle 100 \rangle // \text{ND}$ , while the blue grains moved towards  $\langle 111 \rangle // \text{ND}$ . Orientations starting near  $\langle 101 \rangle$  corner rotated towards the  $\langle 100 \rangle - \langle 111 \rangle$  line at the early stages of deformation. This simulation result macroscopically matches with the experimental observation in Figure 7.3 that indicate the area fraction colored green, which represents orientations close to  $\langle 101 \rangle // \text{ND}$ , decreases as the biaxial strain increases.

Figure 7.5 shows the  $\varphi_2 = 45^\circ$  sections of ODF measured in ferrite grains of IF (Figure 7.5 (a)) and DP (Figure 7.5 (b)) steel with a martensite area fraction of 27%. The texture data were obtained by EBSD at the same position of the specimen before (left-hand column) and after (right-hand column) biaxial deformation. In the IF steel, the ferrite grains have an initially strong  $\gamma$ -fiber ( $\langle 111 \rangle // \text{ND}$ ) and a weak  $\langle 100 \rangle // \text{ND}$  component. Since  $\langle 111 \rangle // \text{ND}$  is the stable orientation for the equi-biaxial tensile deformation mode, as shown in VPSC simulation, the intensity of the  $\gamma$ -fiber in IF steel increased after deformation. On the other hand, in the DP steel, although the initial ferrite texture is very similar to that in the IF steel, the rotated cube texture components of  $(001)[\bar{1}\bar{1}0]$  and  $(001)[\bar{1}\bar{1}0]$ , which are another stable orientation for equi-biaxial tensile

deformation, intensified along with the increase in the  $\gamma$ -fiber. This difference between the IF and DP steels may be a consequence of the interphase interaction between hard martensite and soft ferrite.

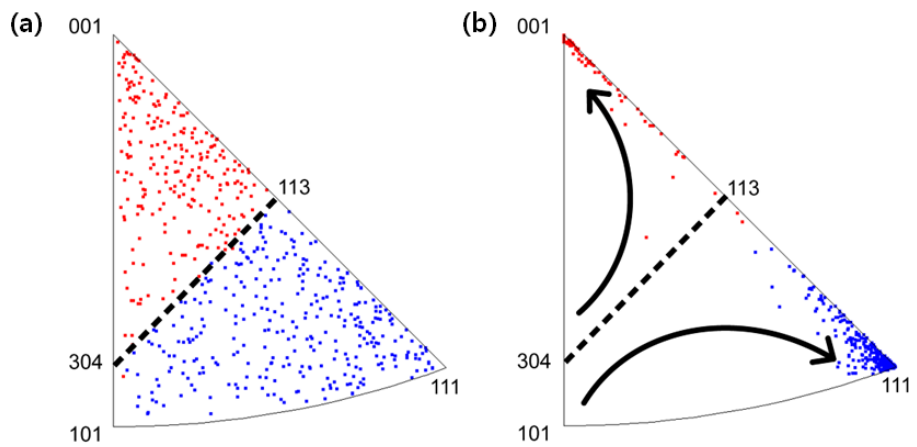


Figure 7.4 Inverse pole figures of steel (a) with random orientation before equi-biaxial strain and (b) after equi-biaxial strain of 40%. Black arrows indicate rotation direction of orientation. Red and blue dots indicate two different regions with  $\langle 001 \rangle // \text{ND}$  and  $\langle 111 \rangle // \text{ND}$  for equi-biaxial tensile deformation, respectively

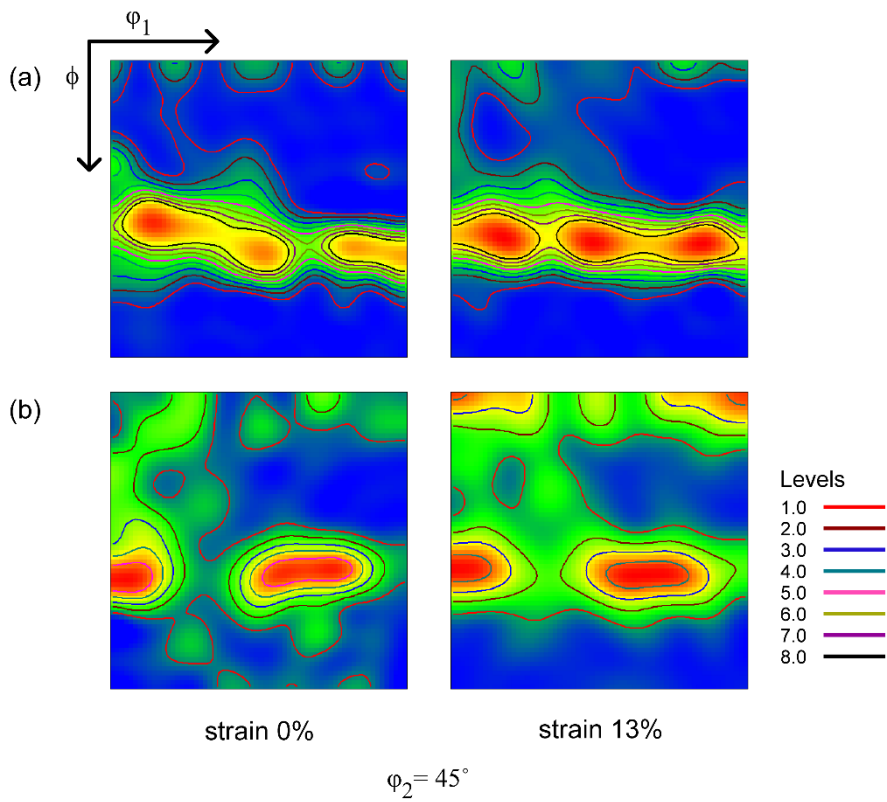


Figure 7.5 ODF sections with  $\varphi_2 = 45^\circ$  obtained at the same area of (a) IF and (b) DP steels with 0% and 27% martensite area fraction before (left-hand column) and after (right-hand column) equi-biaxial tensile deformation

### 7.3.3 Orientation rotation/spread of individual ferrite grains

To investigate the microtexture development inside individual ferrite grains and the intergranular and interphase interactions, several grains with initial orientations marked in black in the inverse pole figures of Figure 7.6 were chosen and examined in detail. In both IF and DP steels, the grains in the regions close to the  $\langle 001 \rangle$  and  $\langle 111 \rangle$  corners rotate towards the stable orientations  $\langle 001 \rangle$  and  $\langle 111 \rangle$ , respectively. This trend agreed with the VPSC prediction. However, in the experimental measurement, increasing orientation spread inside grains was observed as the deformation increased. Notably, the orientation spread in the DP steel is much greater than that in IF steel. Taking the smaller grain size ( $6.5\mu\text{m}$ ) in DP steel than that ( $17\mu\text{m}$ ) in IF steel into consideration, the difference of orientation spread between IF and DP steels is substantial. In the IF steel, orientations starting near the  $\langle 101 \rangle$  corner move towards the midsection of the  $\langle 001 \rangle - \langle 111 \rangle$  line and this feature was also reproduced by the VPSC calculation. On the other hand, it should be noted that the grains of  $\langle 616 \rangle // \text{ND}$  and  $\langle 416 \rangle // \text{ND}$  in DP steel (Figures 7.6 (d) and (e)) exhibit entirely different rotation histories in comparison with the similar grain of  $\langle 516 \rangle // \text{ND}$  in the IF steel. Notably, the grain of  $\langle 416 \rangle // \text{ND}$  in DP steel splits into different grains based on the  $\langle 113 \rangle - \langle 304 \rangle$  border line. It can be seen that one part of the grain moves to  $\langle 001 \rangle$  and the other part to  $\langle 111 \rangle$ . These grain fragmentations in DP steel during deformation might be closely related to the

strengthening of the rotated cube texture component as shown in Figure 7.5.

#### 7.3.4 Strain partitioning and geometrically necessary dislocation (GND)

Based on the above obvious difference of micromechanical behavior and microtexture development between IF and DP steels during equi-biaxial deformation, several effects of hard martensite in DP steel were considered. One of these is strain partitioning between ferrite and martensite<sup>38-40</sup> due to the difference in their hardness. To compare the small-scale mechanical properties of two phases, the nanoindenter-EBSD correlation technique<sup>30,41,42</sup> was used. The mean hardnesses of the ferrite and martensite in the DP steel with 18% martensite area fraction were determined to be 2.9 and 7.3 GPa, respectively. The difference in hardness increases the accumulated strain in the ferrite phase relative to the martensite in DP steel. Therefore, at the same biaxial strain, the actually applied strain in the ferrite region of DP steel is effectively larger than that of IF steel and the enhancement is dependent on the martensite fraction. In addition to the concentration of strain in the ferrite phase, several researchers reported that local shear strain adjacent to the ferrite-martensite interfaces develops in DP steels due to strain partitioning<sup>39,43,44</sup>. Local shear strain is likely to result in localized high dislocation density in the ferrite adjacent to martensite islands, and induce a low BC in this region as shown by EBSD measurements, as shown in Figure 7.3.

Another important effect of the strain partitioning in DP steel is the drastic

increase of surface roughness during deformation. Figure 7 shows the surface morphology and height distribution of DP steel with 18% martensite area fraction after 5% biaxial strain, which was measured by atomic force microscopy (AFM). The martensite islands are high relative to the ferrite grains because of the strain concentration in the soft ferrite grains. It is also apparent that the ferrite regions near the phase interfaces were constrained in the thickness direction because of continuity with neighboring hard martensite islands, which deformed significantly less. The strain constraint in the ferrite regions near ferrite-martensite interfaces induced a steep inclination of the surface in these regions, which also contributes to low BC near the phase interfaces in the EBSD measurements, as shown in Figure 7.3.

The variation in the strain near the ferrite-martensite interface should give rise to strain gradients in ferrite adjacent to martensite islands that induces geometrically necessary dislocations (GNDs)<sup>20-22</sup>. To confirm the GNDs in ferrite regions near martensite, a specimen was re-prepared after 5% biaxial deformation by a light mechanical polishing with colloidal silica to eliminate the surface roughness induced by the deformation. For the EBSD measurement of a smaller region, the spatial resolution was set to 0.05 $\mu\text{m}$ . Figure 8 (a) shows an orientation image after re-preparation of the specimen. Orientation gradients (white arrows) in ferrite grains (marked “F”) adjacent to a martensite island (marked “M”) were evident. To calculate the GND density from the orientation

gradient, the method suggested by Kubin and Mortensen<sup>45</sup> was used. Assuming a series of twist subgrain boundaries in the cylinder, each containing two perpendicular arrays of screw dislocations, the GND density ( $\rho_g$ ) is related to the misorientation angle ( $\theta$ ) as follows,

$$\rho_g = 2\theta / ub \quad (7.2)$$

where  $u$  and  $b$  are the length between two consecutive pixels and the Burgers vector, respectively. Figure 8 (b) shows the calculated distribution of the GND density in the ferrite grains of the region indicated by the dashed box area in Figure 8 (a). The GND density is higher in the ferrite region that is near martensite, where the orientation transition occurs. To observe the dislocation structure directly, the dashed box area depicted in Figure 8 (b) was prepared as a cross sectional sample via FIB and analyzed by HR-TEM. Figure 8 (c) shows a high angle angular dark field (HAADF) image of this region in the [110] ferrite zone axis. It is clear that a high density of tangled dislocations is present in the ferrite region<sup>22</sup> where the orientation transition occurs. The TEM observation is in good agreement with the calculated distribution of the GND density based on the EBSD measurement. From this observation, it was confirmed that the strain constraint in ferrite regions near ferrite-martensite interfaces during deformation induces high density of GNDs. The high dislocation density contributes to the low BC near phase interface observed in

the EBSD measurements, as shown in Figure 3, and the large orientation spread in DP steel.

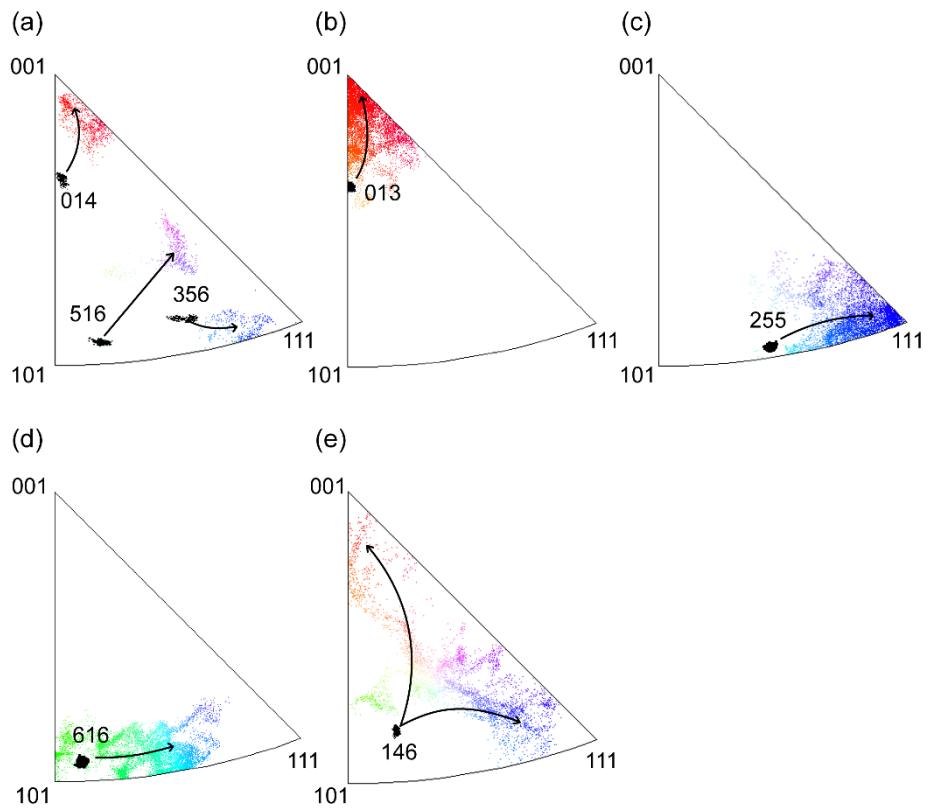


Figure 7.6 Inverse pole figures of measured initial and final orientation of several grains in (a) IF and (b-e) DP steels with 0% and 18% martensite area fraction

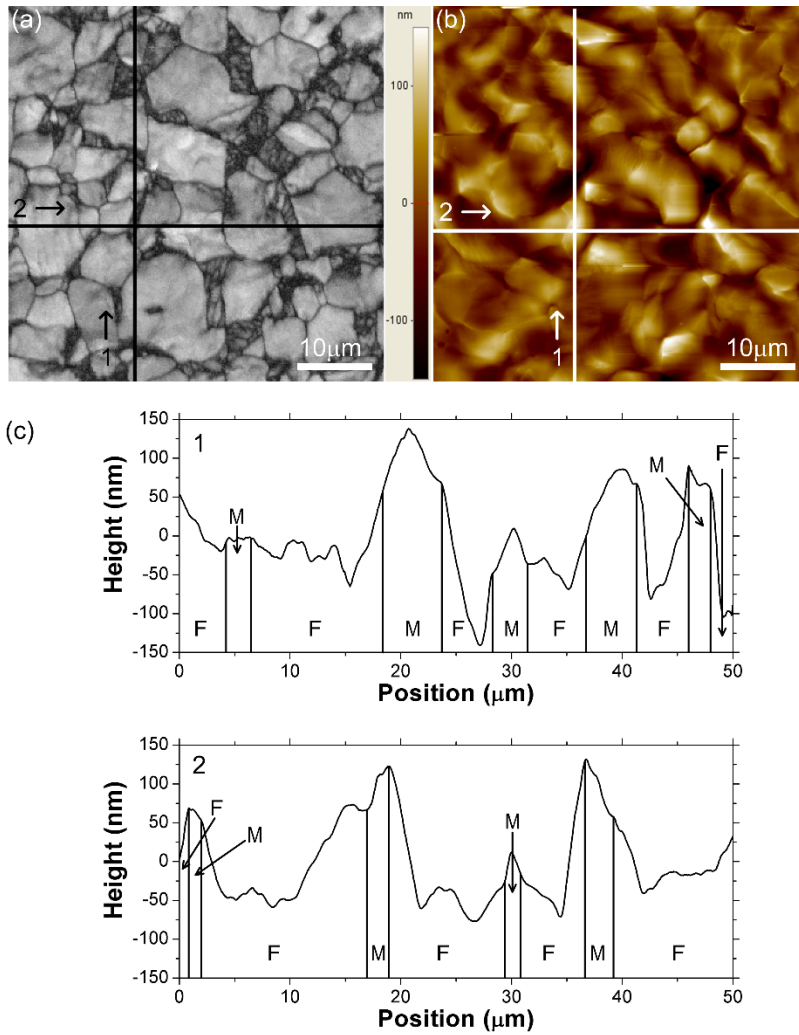


Figure 7.7 (a) EBSD BC image, (b) AFM topography and (c) AFM line profiles matching with line 1 and 2 in (b), respectively, measured in DP steel with 18% martensite area fraction after 5% equi-biaxial tensile deformation. F and M indicate ferrite and martensite, respectively

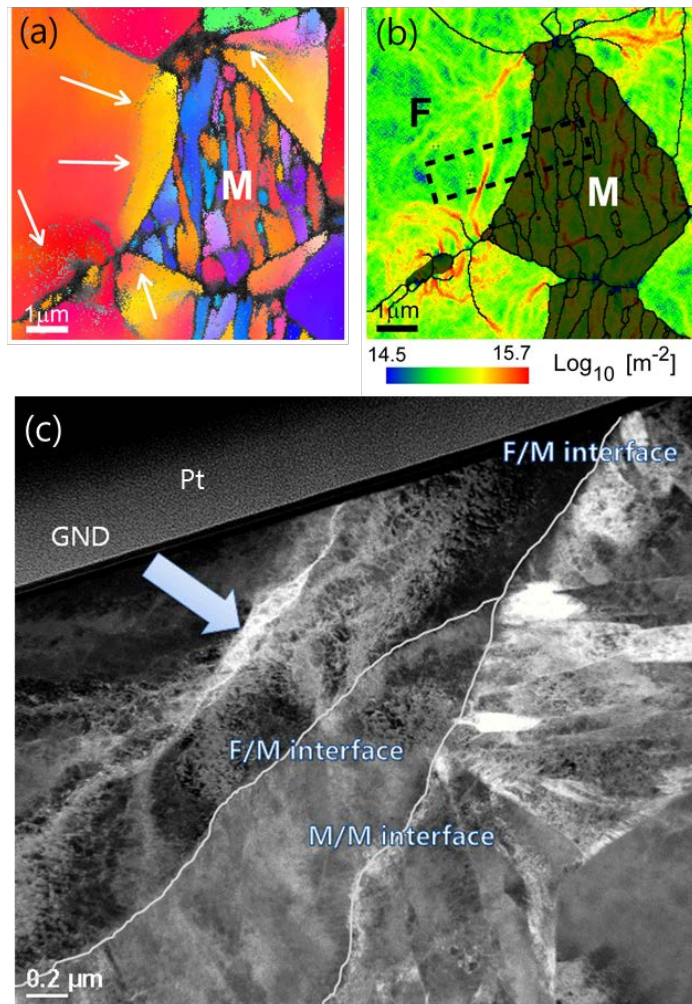


Figure 7.8 (a) EBSD orientation map of DP steel with martensite area fraction 18% after 5% biaxial deformation. Specimen surface was re-polished to eliminate the surface roughness. (b) Calculated distribution of GND density in ferrite grain indicated as dashed box area in (a). (c) HAADF image of the dashed box area depicted in (b)

## 7.4 Conclusion

Microtexture development during equi-biaxial deformation in IF and DP steel sheets with various martensite fractions was investigated by performing HR-EBSD measurement on a special deformation stage positioned inside an SEM chamber. The effect of the hard martensite phase on the microstructural changes during deformation was as follows.

- (1) In both IF and DP steels, orientations close to the  $\langle 001 \rangle$  and  $\langle 111 \rangle$  corners rotated towards the stable orientations  $\langle 001 \rangle$  and  $\langle 111 \rangle$ , respectively. Grains with initial orientation near  $\langle 101 \rangle$  tended to move towards the midsection of the  $\langle 001 \rangle - \langle 111 \rangle$  line at the early stage of deformation. These trends were reproduced by the VPSC calculation. However, grains in DP steels tended to develop higher misorientations inside grains as deformation proceeded in comparison with IF steel. Notably, this trend was strong in grains with initial orientations near  $\langle 101 \rangle$ . These could be described by the strain partitioning and the development of additional local strain above the imposed equi-biaxial strain in ferrite regions near martensite-ferrite interfaces.
- (2) The Band Contrast (BC) values in ferrite regions adjacent to martensite islands drastically decreased as the biaxial deformation increased. This tendency was more evident in DP steel with larger martensite fractions but was rarely observed in IF steel. The loss of pattern quality was induced by

the strain gradient and the steep inclination of the surface in the ferrite regions near martensite-ferrite interfaces. The strain gradient was confirmed through the observation of GNDs in this region through EBSD and TEM.

## 7.5 References

1. P.H. Chang, A.G. Preban, *Acta Metall.* **33**, 897 (1985).
2. P. Tsipouridis, E. Werner, C. Kremaszky, E. Tragl. *Steel Res. Int.* **77**, 654 (2006).
3. K. Mukherjee, S. Hazra, P. Petkov, M. Militzer, *Mater. Manuf. Process.* **22**, 511 (2007).
4. H.N. Han, C.-S. Oh, G. Kim, O. Kwon, *Mater. Sci. Eng. A* **499**, 462 (2009).
5. S.-J. Kim, Y.G. Cho, C.S. Oh, D.E. Kim, M.B. Moon, H.N. Han, *Mater. Design* **30**, 1251 (2009).
6. Y.-S. Song, D.-W. Kim, H.-S. Yang, S.-H. Han, K.-G. Chin, S.-H. Choi, *J. Kor. Inst. Met. & Mater.* **47**, 274 (2009).
7. J. Kim, W. Lee, K.-H. Chung, D. Kim, C. Kim, K. Okamoto, R.H. Wagoner, K. Chung, *Met. Mater. Int.* **17**, 83 (2011).
8. C.M. Vlad, H.J. Bunge, *Proc. of ICOTOM* **6**, 649 (1981).
9. R.K. Ray, *J. Mater. Sci. Lett.* **4**, 67 (1985).
10. R.K. Ray, *Mater. Sci. Eng.* **77**, 169 (1986).
11. D.K. Mondal, R.K. Ray, *Mater. Sci. Eng. A* **158**, 147 (1992).
12. T. Waterschoot, L. Kestens, B.C. De Cooman, *Metall. Mater. Trans. A* **33**, 1091 (2002).
13. S.G. Chowdhury, E.V. Pereloma, D.B. Santos, *Mater. Sci. Eng. A* **480**, 540 (2008).
14. N. Peranio, Y.J. Li, F. Roters, D. Raabe, *Mater. Sci. Eng. A* **527**, 4161 (2010).
15. S.-H. Han, S.-H. Choi, J.-K. Choi, H.-G. Seong, I.-B. Kim, *Mater. Sci. Eng. A* **527**, 1686 (2010).
16. E. Nakamachi, C.L. Xie, M. Harimoto, *Inter. J. Mech. Sci.* **43**, 631 (2001).
17. S.-H. Choi, S.H. Han, K.G. Chin, *Acta Mater.* **57**, 1947 (2009).

18. R.A. Lebensohn, R. Brenner, O. Castelnau, A.D. Rollett, *Acta Mater.* **56**, 3914 (2008).
19. S. Dillien, M. Seefeldt, S. Allain, O. Bouaziz, P.V. Houtte, *Mater. Sci. Eng. A* **527**, 947 (2010).
20. M.F. Ashby, *Philos. Mag.* **21**, 399 (1970).
21. D.A. Hughes, N. Hansen, D.J. Bammann, *Scripta Mater.* **48**, 147 (2003).
22. D.A. Korzekwa, D.K. Matlock, G. Krauss, *Metall. Trans. A* **15**, 1221 (1984).
23. W. Pantleon, *Scripta Mater.* **58**, 994 (2008).
24. M. Calcagnotto, D. Ponge, E. Demir, D. Raabe, *Mater. Sci. Eng. A* **527**, 2738 (2010).
25. F.J. Humphreys, *J. Mater. Sci.* **36**, 3383 (2001).
26. H.M. Rietveld, *J. Appl. Cryst.* **2**, 65 (1969).
27. B.L. Averbach, M. Cohen, *Trans. AIME* **176**, 401 (1948).
28. A.W. Wilson, J.D. Madison, G. Spanos, *Scripta Mater.* **45**, 1335 (2001).
29. J. Wu, P.J. Wray, C.I. Garcia, M. Hua, A.J. Deardo, *ISIJ int.* **45**, 254 (2005).
30. J.-Y. Kang, D.H. Kim, S.-I. Baik, T.-H. Ahn, Y.-W. Kim, H.N. Han, K.H. Oh, H.-C. Lee, S.H. Han, *ISIJ Int.* **51**, 130 (2011).
31. I.L. Dillamore, H. Katoh, *Met. Sci.* **8**, 21 (1974).
32. I.L. Dillamore, H. Katoh, *Met. Sci.* **8**, 73 (1974).
33. Y. Liu, P. Ponte Castañeda, *J. Mech. Phys. Solids* **52**, 467 (2004).
34. R.A. Lebensohn, Y. Liu, P. Ponte Castañeda, *Acta Mater.* **52**, 5347 (2004).
35. R.A. Lebensohn, C.N. Tomé, P. Ponte Castañeda, *Philos. Mag.* **87**, 4287 (2007).
36. R.A. Lebensohn, C.N. Tomé, *VPSC code, Version 7*, Los Alamos (2006).
37. J.W. Hutchinson, *Proc. Royal Soc. London A* **348**, 101 (1976).
38. H.N. Han, C.G. Lee, C.-S. Oh, T.-H. Lee, S.-J. Kim, *Acta Mater.* **52**, 5203 (2004).
39. N. Jia, Z.H. Cong, X. Sun, S. Cheng, Z.H. Nie, Y. Ren, P.K. Liaw, Y.D.

- Wang, *Acta Mater.* **57**, 3965 (2009).
40. J.H. Ryu, D.-I. Kim, H.S. Kim, H.K.D.H. Bhadeshia, D.W. Suh, *Scripta Mater.* **63**, 297 (2010).
  41. T.-H. Ahn, K.-K. Um, J.-K. Choi, D.H. Kim, K.H. Oh, M. Kim, H.N. Han, *Mater. Sci. Eng. A* **523**, 173 (2009).
  42. T.-H. Ahn, C.-S. Oh, D.H. Kim, K.H. Oh, H. Bei, E.P. George, H.N. Han, *Scripta Mater.* **63**, 540 (2010).
  43. J.D. Kang, Y. Ososkov, J.D. Embury, D.S. Wilkinson, *Scripta Mater.* **56**, 999 (2007).
  44. Z.H. Cong, N. Jia, X. Sun, Y. Ren, J. Almer, Y.D. Wang, *Metall. Mater. Trans. A* **40A**, 1383 (2009).
  45. L.P. Kubin, A. Mortensen, *Scripta Mater.* **48**, 119 (2003).

## 요약 (국문초록)

응력 (Stress)은 재료의 합성, 제작, 변형, 그 적용에 이르는 전반적인 과정에 동반되는 물리적, 기계적 현상이다. 소성변형 영역에서는 파괴, 물성저하와 같은 비가역적인 변화를 야기하는 반면에, 탄성변형 영역에서는 전기적, 화학적, 광학적 특성을 가역적으로 변화시키는 것이 가능하다. 탄성영역 내에서 물성변화는, 특히 재료의 크기가 작아짐에 따라 더욱 강화됨에 따라, 1 차원 나노와이어와 같은 저차원 나노물질을 이용한 변형공학(stress 또는 strain engineering) 관련 연구가 활발히 이루어지고 있다.

이러한 저차원 나노물질들은 부피대비 높은 표면면적(surface effect), 양자구속효과(quantum confinement effect), 뛰어난 기계적 물성을 가짐에 따라 벌크 물질과는 상이한 특성을 보여준다. 따라서 나노와이어는 저차원 나노물질 연구 소재 중 주목 받고 있는 소재 중의 하나이다. 또한 외부 응력을 이용한 나노소재의 반응을 이용하여 에너지 하베스팅(energy harvesting), 압전형 나노 발전기(piezoelectric nano-generator), 신축성 전자 장치(stretchable electronics) 개발에 활용되고 있다.

본 연구에서는 1 차원 나노 물질 (나노와이어)의 성장 및 전기적, 기계적 거동에 미치는 응력의 영향에 관한 연구를 진행하였다. 본 연구는 크게 두 가지로 나누어 설명할 수 있다.

첫째, 외부응력을 이용한 나노와이어의 성장 연구는 다음과 같다. 갈륨 ( $Ga^+$ ) 집속 이온빔(Focused Ion Beam)을 InGaN 기판에 조사함에 따라 발생하는 압축응력을 이용하여, 단결정 인듐(indium) 나노와이어를 성장 시켰다. 이온빔 조사 전, 후 시편의 미세구조 및 화학 성분 분석을 통해 인듐 나노와이어는 갈륨 이온빔 조사에 의한 InGaN 기판의 상분해로 인듐이 공급되어 성장하는 것을 확인하였다. 또한 이온빔 조사 또는 이온주입은 시편 표면층에 격자간 원자, 공공 등의 결함을 형성하여

압축응력을 유발하는 것으로 알려져 있으며, InGaN 기판의 면간거리 측정을 통해 인듐 나노와이어는 내부에 축적된 압축응력의 완화를 통해 성장하는 것을 확인할 수 있었다. 상분해된 인듐은 나노크기의 입자형태로 존재하여 진공상태에서 액상의 형태로 다공성 기판 내부를 채우게 되며 최종적으로 정수압(hydrostatic pressure) 상태가 된다. 이러한 압축응력은 인듐 원자의 이동을 가속화시켜, 단결정 나노와이어를 최고 500 nm/s 의 속도로 고속성장 시키는 것이 가능하였다. 집속이온빔을 이용한 나노와이어의 성장은 이온빔의 가속전압, 전류밀도, 조사영역 등을 정밀하게 설정하는 것이 가능하며, 나노와이어의 길이, 두께뿐만 아니라 성장속도를 효율적으로 조절할 수 있다. 두께 40-200 nm, 최고길이 120  $\mu\text{m}$  의 나노와이어가 성장가능하며, 고속의 성장속도는 기존 다른 나노와이어의 성장 방법에 비해 현저히 빠른 성장속도를 보여주었다. 뿐만 아니라 이온빔을 이용한 마스크리스(maskless) 패터닝을 이용하여, 특정 영역에 나노와이어를 선택적으로 성장시키는 방법은 나노와이어를 이용한 소자 제작에 획기적인 기여를 할 것이라 예상된다.

두번째로, 나노와이어에 외부응력을 가함에 따른 기계적, 전기적 특성의 변화를 상변화 메모리에서 활용되는  $\text{Ge}_2\text{Sb}_2\text{Te}_5$  (GST) 물질을 이용하여 압저항 효과 및 상변화 특성을 연구하였다. 단결정 GST 나노와이어는 기상-액상-고상 매커니즘을 이용하여  $\langle 10 \bar{1} 0 \rangle$  방향으로 성장시켰으며, 일축압축 (-0.4%) 시 저항이 감소하고, 인장 (+0.4%) 시 저항이 증가하였으며, 이러한 상대적인 저항변화 ( $\pm 60\%$ )는 외부응력에 따라 가역적으로 반응하였다. GST 나노와이어는 in-situ 인장 실험을 통해 평균 45 GPa 의 탄성계수와 1.5%까지 탄성영역을 가짐을 확인할 수 있었으며, 본 연구에서 적용한 0.4% 이상의 탄성변형을 넘어서 추가적인 변형 및 전기적 특성의 변화가 가능함을 확인할 수 있었다. 측정된 탄성계수 및 저항변화를 통해 P 형 반도체인 GST 나노와이어는  $92.5 \sim 448.5 \times 10^{-11} \text{ Pa}^{-1}$  압의 압저항 계수 ( $\pi_l^p$ )를 가짐을 확인할 수 있었으며, 이 결과는 GST

물질로써 최초의 압저항 효과에 관한 연구 결과이며, 실리콘 나노와이어의 특성과 비교될만한 압저항 효과로 예상된다. 0.4% 미만의 미소변형 구간에서의 GST 나노와이어의 압저항 효과는 밴드갭 또는 캐리어 농도 변화에 기인한 것이 아니라 공공의 이동도 (hole mobility)의 향상에 기인한 것이라 예상된다. 또한 이러한 외부응력은 GST 의 비정질에서 결정질로 상변화 거동에도 영향을 미침에 따라, 임계전압 (threshold voltage)이 압축시 감소, 인장시 증가하는 변화를 보여, 압축시 더 빠른 결정화 거동을 보임을 확인할 수 있었다. 이와 같은 결과는 상변화 메모리 소자 연구에 기여하여 휩 가능한 전기소자, 상변화 메모리, 변형센서로의 적용이 가능할 것이라 예상된다.

본 연구 결과는 1 차원 나노와이어의 성장에서부터 전기적, 기계적 특성 변화에 미치는 응력의 변화를 변형공학의 측면에서 연구하였다. 외부응력을 조절함에 따라 인듐 나노와이어의 성장 조절 및 성장 매커니즘을 이해하였으며, 상변화 물질인 GST 나노와이어의 전기적, 기계적 특성 향상을 변형공학 측면에서 적용하였다. 위 연구 결과는 1 차원 나노물질의 합성 및 활용에 있어서 큰 기여를 한 것으로 판단된다.

**표제어:** 나노기술, 1차원 나노와이어, 집속이온빔, 인듐, 응력을 이용한 나노와이어 성장, 상변화 메모리,  $\text{Ge}_2\text{Sb}_2\text{Te}_5$ , 임계전압, 일축 응력, 압저항 효과

**학 번:** 2006-20819